ABSTRACT

Title of Dissertation:	DESIGN AND PERFORMANCE CHARACTERIZATION OF AN ADDITIVELY-MANUFACTURED HEAT EXCHANGER FOR HIGH TEMPERATURE APPLICATIONS
	Xiang Zhang, Doctor of Philosophy, 2018
Dissertation directed by:	Professor Michael Ohadi, Mechanical Engineering

In its early stages of development, additive manufacturing was used chiefly for prototyping, but over the last decade, its use has evolved to include mass production of certain products for numerous industries in general, and speciality industries such as biomedical and aerospace industries in particular. Additive manufacturing can be used to fabricate unconventional/complex designs that are difficult and time-consuming through conventional fabrication methods, but offer significant performance advantage over state of the art. One such example is high temperature heat exchangers with complex novel geometries that can help improve the heat transfer density and provide better flow distribution, resulting in more compact and efficient designs and thereby also reducing materials costs considering fabrication of these heat exchangers from the suitable super alloys with the conventional manufacturing techniques is very difficult and laborious.

This dissertation presents the results of the first high-temperature gas-to-gas manifold-microchannel heat exchanger successfully fabricated using additive manufacturing. Although the application selected for this dissertation focuses on an aerospace pre-cooling heat exchanger application, the results of this study can still directly and indirectly benefit other industrial sectors as heat exchangers are key components of most power conversion systems. In this work, optimization and numerical modelling were performed to obtain the optimal design, which show 30% weight reduction compared to the design baseline. Thereafter, the heat exchanger was scaled down to 66 × 74 × 27 mm^3 and fabricated as a single piece using direct metal laser sintering (DMLS). A minimum microchannel fin thickness of 165 μm was achieved. Next, the additively manufactured headers were welded to the heat exchanger core and the conventionally manufactured flanges. A high-temperature experimental loop was next built, and the additively manufactured heat exchanger was successfully tested at 600°C with ~ 450 kPa inlet pressure. A maximum heat duty of 2.78 kW and a heat transfer density close to 10 kW/kg were achieved with cold-side inlet temperature of 38°C during the experiments. A good agreement between the experimental and numerical results demonstrates the validity of the numerical models used for heat transfer and pressure drop predictions of the additively manufactured heat exchanger. Compared to conventional plate-fin heat exchangers, up to 25% improvement in heat transfer density was achieved. This work shows that additive manufacturing can be used to fabricate compact and lightweight high temperature heat exchangers, which benefit applications where space and weight are constrained.

DESIGN AND PERFORMANCE CHARACTERIZATION OF AN ADDITIVELY-MANUFACTURED HEAT EXCHANGER FOR HIGH TEMPERATURE APPLICATIONS

By

Xiang Zhang

Dissertation submitted to the Faculty of the Graduate School of the
University of Maryland, College Park, in partial fulfillment
of the requirements for the degree of
Doctor of Philosophy
2018

Advisory Committee:
Professor Michael Ohadi, Chair
Professor Amir Shooshtari
Professor Bao Yang
Professor Christopher Cadou
Professor Marino diMarzo
Professor Peter Chung

Dedication

To my parents, my wife, and my son

who have helped, encouraged, and supported me always

Acknowledgements

First and foremost, I would like to thank my advisor Dr. Michael Ohadi and my co-advisors Dr. Amir Shooshtari and Dr. Serguei Dessiatoun for their guidance, help, encouragement, and support for my research. I will carry what I learned from them with me throughout the rest of my life.

I would like to express my gratitude to Dr. Hal Strumpf from Honeywell Aerospace for providing specifications and technical advices which were very helpful for the completion of this research project. I also wish to thank Mr. Howard Grossenbacher from the machine shop of the Aerospace Engineering Department at the University of Maryland for his continued help on the high-temperature experimental setup's preparation. I wish to thank Ms. Becky Lorenz for her help in welding of the test section as well.

I am grateful to my friends at Smart and Small Thermal Systems Laboratory (S2TS), especially Farah Singer, Martinus Arie, Fabio Battaglia, Stefan Bangerth, David Hymas, Raphael Mandel, David Deisenroth, Daniel Bae, and Ratnesht Tiwari for providing a constructive and peaceful environment and also their helpful tips and suggestions regarding my research.

Table of Contents

List of Tables

List of Figures

Nomenclature

A_{base}	area of the microchannel surface base [m^2]
A_{chn}	microchannel cross section area [m^2]
Cd	discharge coefficient [-]
CF	configuration correction factor of both unmixed cross-flow [-]
COP	coefficient of performance [-]
Cp	specific heat [J/kg-K]
D_{chn}	microchannel cross section hydraulic diameter [m]
Di	nozzle inlet cross section diameter [m]
Do	nozzle throat diameter [m]
H	heat exchanger core overall height [m]
H_{base}	microchannel surface base height [m]
h_{base}	base conductance ($h_{base} = Q/A_{base}(T_{in} - T_{base})$) [$W/m^2K$]
L	heat exchanger core overall length [m]
$LMTD$	log mean temperature difference [K]
m	mass [kg]
$\dot{m}$	mass flow rate [kg/s]
N_{layer}	total number of manifold-microchannels layers [-]
P	system pressure [Pa]
ΔP	pressure drop [Pa]
Q	heat duty [W]
Re	Reynolds number [-]
T	temperature [°C]
ΔT	temperature difference [°C]
t_{fin}	fin thickness [m]
U	overall heat transfer coefficient [W/m^2K]
U_X	uncertainty of variable X [-]
$\dot{V}$	volumetric flow rate [m^3/s]
W	heat exchanger core overall width [m]
W_{chn}	microchannel width [m]
$Wall_{mnd}$	manifold wall thickness [m]

Greek Symbols

μ	dynamic viscosity [kg/(m·s)]
ρ	density [kg/m^3]

Subscripts

base	microchannel surface base

cal	calibration
chn	microchannel
cold	cold side flow
exp	experiment
hot	hot side flow
in	inlet
mnd	manifold
num	numerical
out	outlet
std	standard

Abbreviations

AM	additive manufacturing
DMLS	direct metal laser sintering
DOE	design of experiment
EBM	electron beam melting
ECS	environmental control system
HTGR	high temperature gas-cooled reactor
HTHX	high temperature heat exchanger
HX	heat exchanger
IHX	intermediate heat exchanger
LOM	laminated object manufacturing
LTHX	low temperature heat exchanger
M2HX	manifold-microchannel heat exchanger
PCHX	printed circuit heat exchanger
PFHX	plate-fin heat exchanger
sCO2	Super critical CO_2
SLM	selective laser melting

Chapter 1: Introduction

1.1. Motivation and Background

Energy saving through heat recovery has been an important objective in many industries. Researchers have identified the importance of high temperature heat exchangers with operating temperatures of 500-1000°C to recover heat from a hot exhaust stream and transfer it for heating cold inputs to the system [1]. It is well established that higher cycle efficiencies can be obtained when the turbine inlet temperature for a typical power generation cycle is increased. However, increases in turbine inlet temperature are limited by the high temperature heat exchangers which support the power generation cycle. One of such high temperature heat exchangers is used in aircraft environmental control system (ECS), in which heat exchangers are used to cool compressor bleed air using ram air as the heat sink, and the cold exhaust air on the hot side is used to condition the aircraft cabin as shown in Figure 1-1 [2]. High temperature heat exchangers can also be used to increase gas turbine efficiency where high temperature recuperators used for this purpose have a typical operating temperature of about 580°C [3, 4]. Another application of high temperature heat exchangers is in gasoline fueled vehicles to reduce fuel consumption by recovering waste heat from exhaust ranging from 200 to 850°C and converting it to mechanical or electrical energy [5, 6]. High temperature heat exchanger is also used in gas cooled nuclear reactors where an intermediate gas-gas heat exchanger recovers nuclear heat (> 800°C) and transfers it to secondary systems to generate electricity or hydrogen [7-9].

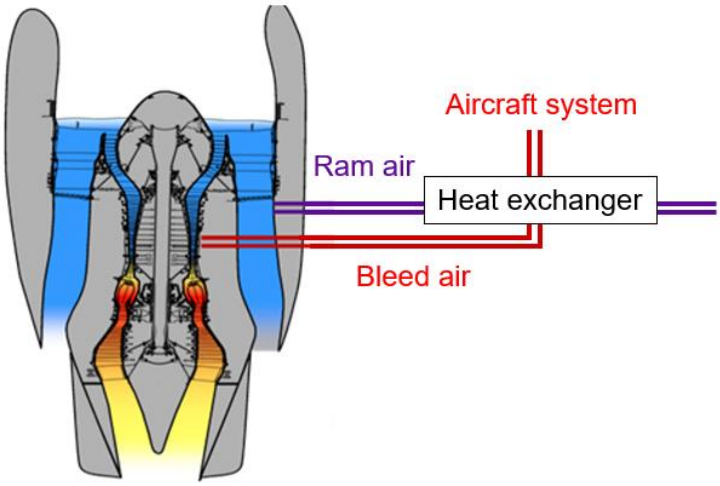

Figure 1-1: Heat exchanger in aircraft environmental control system

Currently, the most widely commercialized type of compact heat exchanger used in high temperature gas-to-gas applications is the plate-fin heat exchanger (PFHX) [10-12]. To improve the performance over the conventional designs, novel heat transfer surfaces have been suggested in recent years. One such design is the manifold-microchannel technique first proposed by Harpole and Eninger [13] in 1991. Since then, numerous studies have been reported in the literature discussing the superior performance of this technology in various applications compared to conventional technologies [14-26]. Unlike the plate-fin design, the manifold-microchannel concept design utilizes a manifold placed on top of microchannels as shown in Figure 1-2. Then, through the manifold, the air is distributed into the microchannels and travels a short length in each microchannel before it is guided out. Due to the short flow length, the air flow in the microchannel typically remains in the developing regions, which results in substantially higher heat transfer coefficients. Studies by Arie et al. [15, 25] show that an air-cooled air-to-water heat exchanger utilizing manifold-microchannel has higher heat transfer density and

heat transfer coefficient than other state-of-the-art dry cooling heat exchangers used for power plants. Jha et al. [17, 18] investigated the performance of a tubular manifold-microchannel evaporator for waste heat recovery systems and reported high heat transfer coefficients. Researchers also demonstrated enhanced performance of plate heat exchangers with manifold-microchannel used for refrigeration/air conditioning [19, 24, 26].

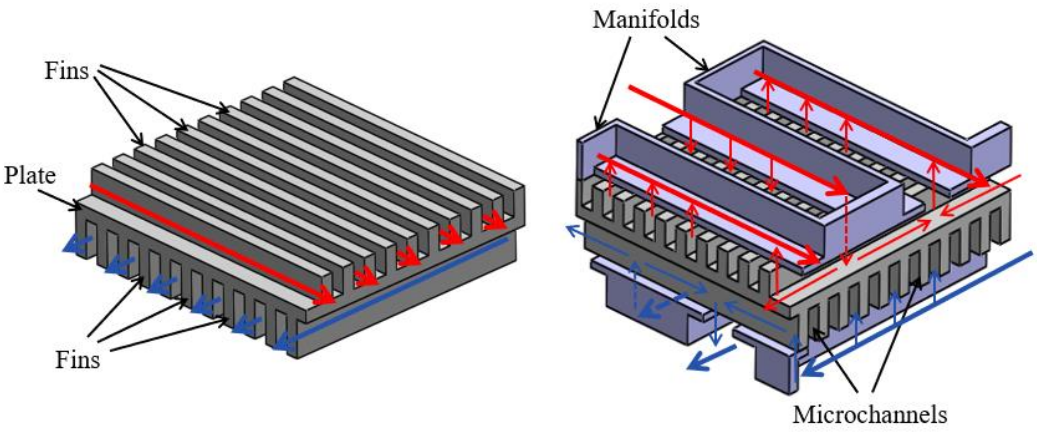

Figure 1-2: Plate-fin concept (left) vs. manifold-microchannel concept (right)

Despite the superior performance of manifold-microchannel heat exchangers for various applications reported in the literature, their main drawback is the difficulty associated with their manufacturing. When the manifolds and the microchannel surface are conventionally manufactured separately, the heat exchanger with multiple layers of manifolds and microchannel surfaces (as shown in Figure 1-3) must be assembled through brazing, welding or diffusion bonding. In these processes, the bonding material may penetrate and obstruct the microchannels, adversely affecting the performance of the heat exchanger. Moreover, for large-scale heat exchangers consisting of hundreds of manifold-microchannel layers, the assembly process is challenging and time consuming.

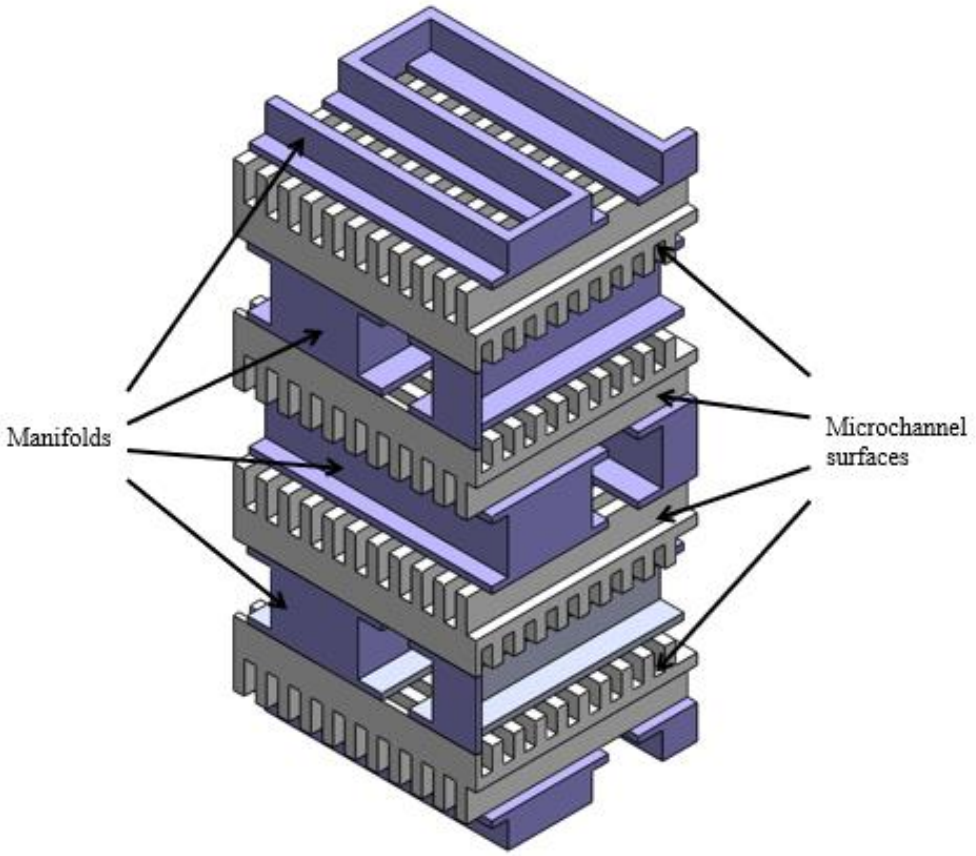

Figure 1-3: Multiple layers of manifolds and microchannel surfaces

Additive manufacturing (AM) has evolved from prototyping to mass production in the last decade and is now used in many industries such as biomedical, automotive, and aerospace [27, 28]. AM can produce lightweight structures with high mechanical robustness and has capability to fabricate unconventional designs that are not possible using conventional fabrication methods. Heat exchangers are one such applications for which AM has recently gained traction. Additively manufactured heat exchangers can be fabricated with complex internal geometries and external shapes with lighter weight and higher compactness which are key factors for heat exchangers used in high end applications such as aerospace industry. The shorter lead time to produce the heat exchangers is another advantage

of AM. High temperature heat exchangers typically involve expensive materials. Additive manufacturing of these heat exchangers by incorporating unconventional designs can help improve the heat transfer density, and provide better flow distribution, resulting in compact and efficient heat exchangers at reduced cost.

Additive manufacturing technology has shown great potential not only for the design and construction of complex geometries but also for simplifying the assembly process and reducing fabrication steps. Recently the direct metal laser sintering (DMLS) process has been used successfully to fabricate metallic fins as thin as 220 μm for an air-to-water manifold-microchannel heat exchanger produced as a single unit (manifold-microchannel was only used on the air side while water side had simple rectangular channels) [29-33]. In another recent study, Grestler and Erno's [34] metallic heat exchanger, which is used as a turbine engine fuel-cooled oil cooler, was also fabricated through selective laser melting (SLM) without any assembly process.

Although there have been a few studies on additively manufactured heat exchangers, no work is reported in the literature which addresses development of AM heat exchangers for high-temperature gas-to-gas applications such as those found for heat exchangers in aircraft environmental control systems, which must be able to operate up to temperatures of 650°C with bleed hot air [16, 34-37]. The current work demonstrates the successful design and fabrication through DMLS of a gas-to-gas manifold-microchannel heat exchanger using Inconel 718. In this work, the manifold-microchannel was used on both hot and cold sides. The heat exchanger was experimentally tested with N_2 on the hot-side at 600°C and air on

the cold-side at 38°C. The experimental results were compared against the calculated performance of conventional plate-fin heat exchangers to assess the performance enhancement.

1.2. Dissertation Objective

The main objective of this dissertation is to design, built and test a gas-to-gas heat exchanger that can provide significant performance enhancement compared to conventional heat exchangers for aerospace application. This is to be accomplished by implementing advanced fabrication techniques, advanced heat transfer surfaces, and design optimization. Accomplishing this objective will be an important step towards development of economical gas-to-gas heat exchangers for aircrafts environmental control system. In addition, although this study focuses on gas-to-gas pre-cooling for aircraft, the knowledge gained in this study can be applied to many other applications where air or gas is used as the heat transfer medium, such as HVAC, automotive (car radiator), and electronic cooling applications.

1.3. Approach

To accomplish the project objective, metallic heat exchangers were exhaustively studied. Metallic heat exchangers are the most common type of heat exchangers, especially for aerospace applications, due to their high structural strength. To demonstrate the technology, a full-scale air-to-air heat exchanger design was created based on the operation conditions through an optimization process. Then, a scaled-down unit was designed, fabricated, and experimentally tested. This was motivated by the notion that a full-scale aerospace pre-cooling heat exchanger is

too risky and expensive to build. The scaled-down unit also does not require a sizeable test setup compared to the full-scale unit. The heat exchanger can be then scaled up for the given application based on the experimentally validated model. The scaled-up design was compared with the conventional design to calculate how much improvement the advance design could yield. A flow chart showing the major steps performed to accomplish the dissertation objective is shown in Figure 1-4.

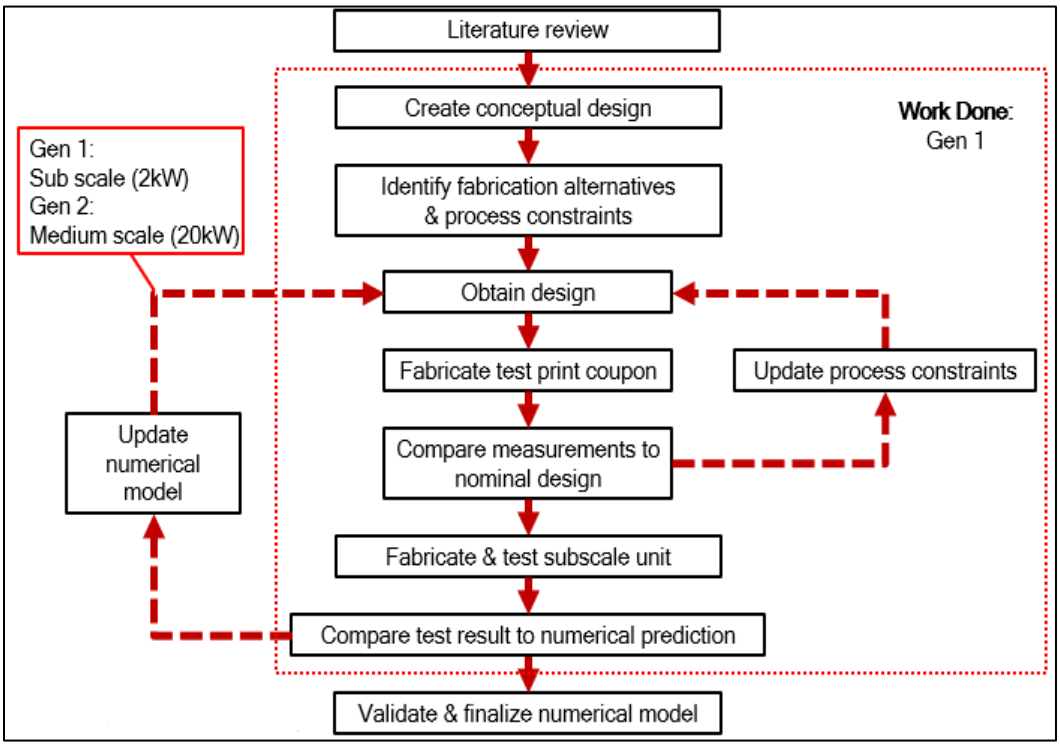

Figure 1-4: Flow chart of the project approach

A summary of each step is provided in the following.

1. *Literature* review of high temperature heat exchangers

   A detailed literature review of high temperature heat exchangers was performed. The study included identifying common types of high

temperature heat exchangers (HTHXs) and their corresponding applications in the literature.

2. *Define the design requirements & create conceptual design*

   The design requirements for the heat exchanger, such as heat exchanger capacity, pressure drops on both hot and cold sides, inlet temperatures, system pressures, and mass flow rates were defined based on specifications of a typical heat exchanger on aircraft. A conceptual design was then created based on the manifold-microchannel technology and the design requirements.

3. *Identify fabrication alternatives & process constraints*

   A study was performed on the advanced manufacturing techniques that can be used to fabricate the metallic high temperature heat exchanger. The study included fabrication techniques and fabrication limitations such as minimum feature size and maximum fabrication size.

4. *Create the heat exchanger design*

   Based on the chosen fabrication approach, the fabrication limitations and constraints identified in the previous step were implemented for the design selection and sizing. A full-scale heat exchanger design was then created through the optimization process.

5. *Fabricate test print coupon & update fabrication process constraints*

   To save time and confirm the actual fabrication constraints, several sectional test coupons were fabricated by the additive manufacturing

technique. A detailed evaluation was performed to check the quality of the fabricated coupons. If the measured parameter (for example, fin thickness) turned out to be significantly different from the design value, the design process constraints would be updated, and a new design would be obtained. Then this step would be repeated until all the manufacturing constraints are satisfied.

6. *Fabricate & test scale-down unit*

   Once the test print coupon's quality was confirmed from the previous step, a subscale unit was created by scaling down the full-scale unit to meet the AM fabrication size limitation for the identified AM printer. The subscale unit was then fabricated through additive manufacturing and tested under high temperature conditions, which were chosen based on the scaling-down process, initial design requirements, and the capability of the test setup.

7. *Compare test results to numerical prediction & update numerical model*

   By comparing the test results of the subscale unit to the numerical predictions, if the difference was too large, the numerical model would be examined and improved, and some or all previous steps would be repeated. If the heat exchanger design requirements and fabrication constraints/limitations were updated, then another full-scale as well as subscale design would be created. The new subscale unit would be tested to check the revised numerical model.

1.4. Major Contributions

The major contributions of this study are as follows:

1. The successful use of additive manufacturing is demonstrated for the first time to print a metal gas-to-gas cross-flow manifold-microchannel heat exchanger for high-temperature applications.
2. A computational model was developed, and the model was verified by comparison of the results with those of the experiments, thus verifying the model that can be used as a design tool.
3. The performance of an additively manufactured manifold-microchannel heat exchanger is characterized for the first time at temperatures up to 600ºC and pressures up to 4.5 bar through a new high-temperature experimental setup. This setup can be used to test different high temperature heat exchangers under desired conditions.

Details of the work are documented in respective chapters of this dissertation.

1.5. Dissertation Layout

The layout of this dissertation is as follows. First a literature study of conventional and state-of-the-art high temperature heat exchangers is presented in chapter 2. The design requirements are defined in chapter 3. In addition, the manifold-microchannel concept is explained. Subsequently, the fabrication alternatives are presented in chapter 4. The fabrication process and constraints are also discussed in detail. Next, the numerical method used to predict the performance is explained

in chapter 5. The optimal full-scale air-to-air heat exchanger design was also selected based on the optimization results with different fabrication approaches. Then, the full-scale design's scaling-down process is presented. The test print coupon study is discussed in chapter 6, and the subscale unit's design and fabrication are discussed as well. The experimental work on the scaled-down heat exchanger is discussed in later chapters. The experimental results are then compared with numerical predictions. Considering the decent agreement between the experimental and numerical data, an advanced design was created and discussed in chapter 9. Lastly the conclusion and future work are presented in the last chapter.

Chapter 2: Literature Review

2.1. Introduction

High temperature heat exchangers (HTHXs) are described in the literature as operating above an arbitrary value of 500°C, and early development of HTHXs was motivated by the first oil shock in 1973, which created a demand for energy saving and more effective use of energy [38]. Since then, various types of HTHXs have been developed, and many have been used as recuperators for gas turbine engines, aerospace, hydrogen production, waste heat recovery, supercritical CO_2 power cycles, and high temperature fuel cell systems [39-43]. Heat exchangers operating at such high temperatures are subject to unique material challenges such as creep, reduced strength at higher temperatures, oxidation of material, corrosion, and thermal shock.

Most materials used at lower temperatures, such as steel, copper, and aluminum, lose their thermo-mechanical properties at elevated temperatures. For this reason, they cannot be used for HTHX applications. Rather, materials which can retain their properties at high temperatures, such as high-grade steels and Ni-based alloys, are used for HTHXs. The strength of some material candidates for HTHXs application are shown in Figure 2-1. As shown there, most of these materials lose strength at temperatures exceeding 550°C and particularly above 600°C. Depending upon the operating temperature and pressure, high temperature materials can vary from steels to Ni-based alloys and ceramics. The prices for the material can vary from ~$2-3/kg for steel to ~$70/kg for Ni-based alloys [44].

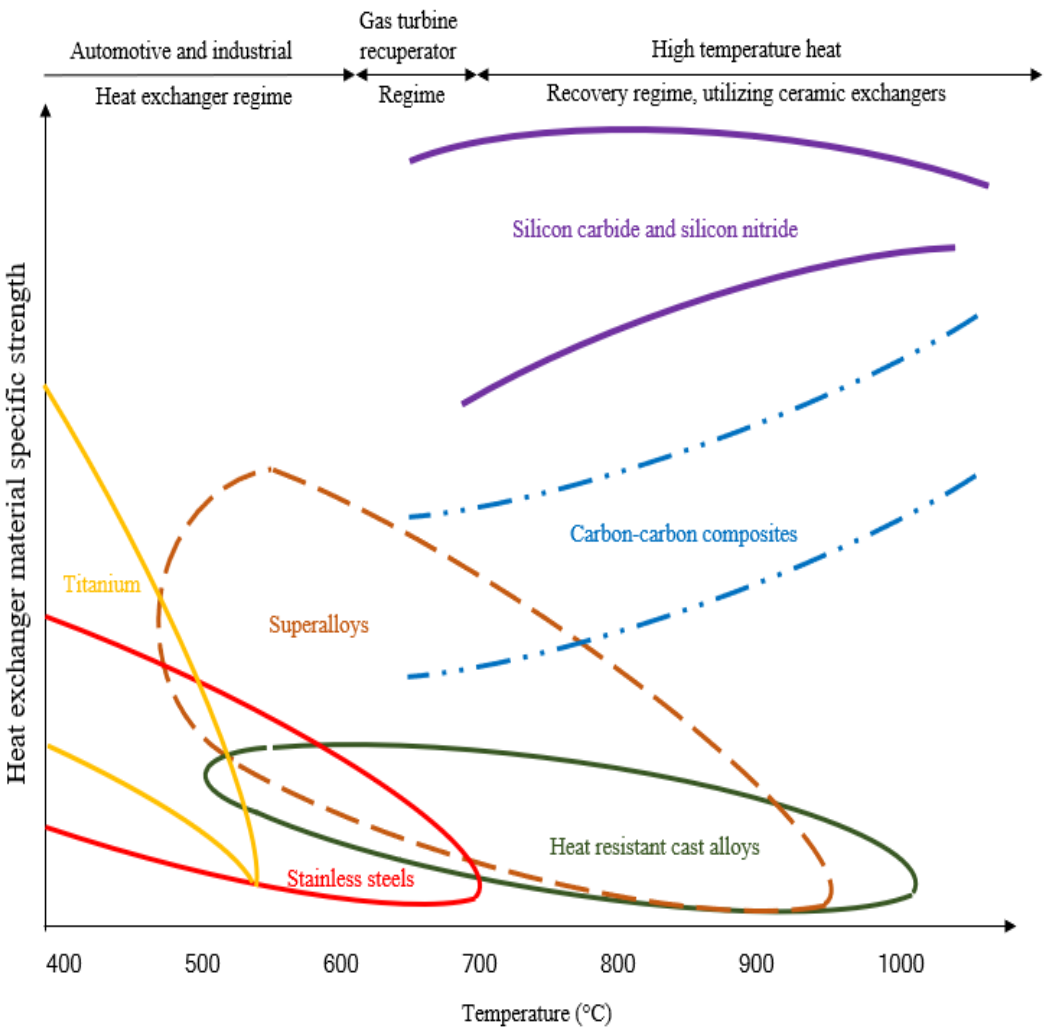

Figure 2-1: Temperature ranges for heat exchanger materials (adapted from reference [45])

As a result, expensive alloys that retain their strength at elevated temperatures are typically the material of choice. However, these alloys typically have low thermal conductivity, and difficult manufacturability [46, 47], and thus they present their own challenges in heat exchanger design and fabrication. Even these alloys lose strength at elevated temperatures. This low strength at higher operating pressures means that the walls must be thicker, requiring more material. Thick wall geometry

makes the HTHXs made of expensive alloys cost prohibitive in most power cycle applications. One way to offset these costs is to develop compact heat exchangers that have higher surface area to volume ratio and thus reduce the amount of material needed. As a result, in past couple of decades, there has been increased interest in development of compact and cost effective HTHXs [48, 49]. Advanced manufacturing techniques, mainly additive manufacturing of metals, have recently shown potentials in fabricating compact HTHXs with innovative heat transfer surface designs [50]. This chapter provides insights into recent developments in design and application areas of HTHXs.

2.2. Types of High Temperature Heat Exchangers

The cost of HTHX increases exponentially as the operating temperature increases, particularly above 600°C, mainly due to the material cost as well as manufacturing cost of the superalloy and ceramic heat exchangers [12]. Higher pressure applications such as those encountered in the power cycles complicates the issue even further. The majority of conventional heat exchanger designs used in low temperature applications prove to be uneconomical at high operating temperatures. The high cost of exchangers in power plant applications such as supercritical CO_2 Brayton cycles is a major stumbling block to making the cycle economical [10].

As a result, newer designs of heat exchangers that utilize the materials more efficiently, namely higher surface area to volume ratio designs, are being developed [10, 50]. These designs typically use microchannels as well as fin geometries to accomplish the higher area. An added advantage of smaller channel sizes is that the

heat transfer in such miniature geometries is much higher [51, 52]. This section reviews various heat exchanger types and designs utilized in high temperature applications.

2.2.1. Plate-fin heat exchanger (PFHX)

Plate-fin heat exchangers (PFHXs) are one of the most commonly utilized HTHXs for diverse industrial sectors. They are used mainly for gas-to-gas heat transfer applications. The main components of a PFHX, including side bars, fins, and parting sheets, are shown in Figure 2-2. The fins are usually fabricated using a stamping process and are brazed together with the base plates. A brazed PFHX can withstand a maximum pressure of 90 bar, while diffusion bonded PFHXs can be used under pressures up to 200 bar [10].

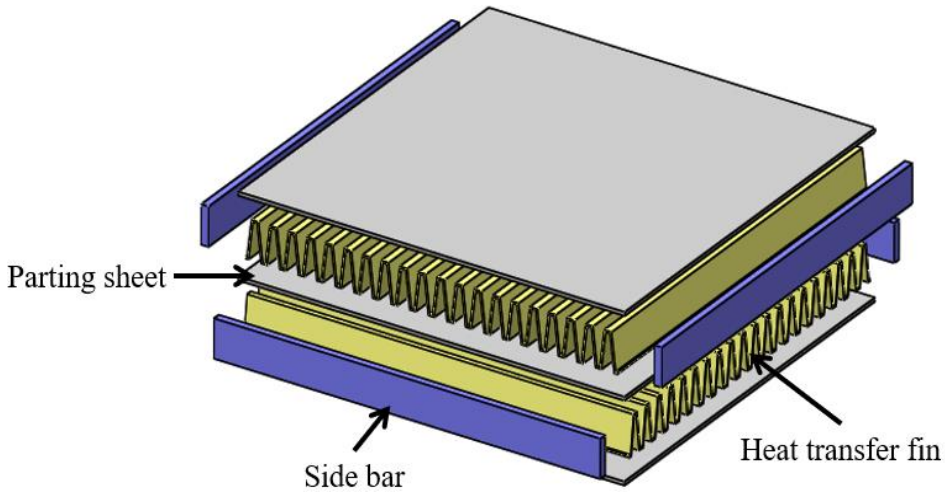

Figure 2-2: Illustration of main components of PFHX

The fins in PFHXs can be easily rearranged, which allows the PFHXs to operate in any of the cross-flow, counter-flow, or cross-counter-flow configurations. The

main applications for PFHXs at high temperatures are gas turbine and power plants for hot gas heat recovery. Generally, PFHXs have a good heat transfer area to volume ratio and hence can be compact and economical for high-temperature applications [10].

2.2.2. Plate-and-frame heat exchanger

Plate-and-frame heat exchangers are often used to transfer heat between two liquids or two gases. The fluid-separating plates of these heat exchangers are typically manufactured by compression processing of a thin metal sheet, and they come in several patterns such as wavy, chevron, washboard, herringbone, cross-corrugated, cross-undulated, or cross-wavy [49, 53-55]. Two such heat transfer plates are then stacked to produce a single cell, and this process is repeated to manufacture the required number of cells. The structural strength of the core is achieved through the connection of the end plates once all the cells are stacked, as shown in Figure 2-3 [56]. For high pressure applications, the plates can be welded or brazed together to ensure operation up to 200 bar pressure and 815°C temperature [57]. Two layouts are typically used for plate-and-frame heat exchangers in recuperators in microturbine systems: 1) rectangular designs, which are installed behind the rotating machinery, and 2) annular designs, which are wrapped around the turbine [49, 58].

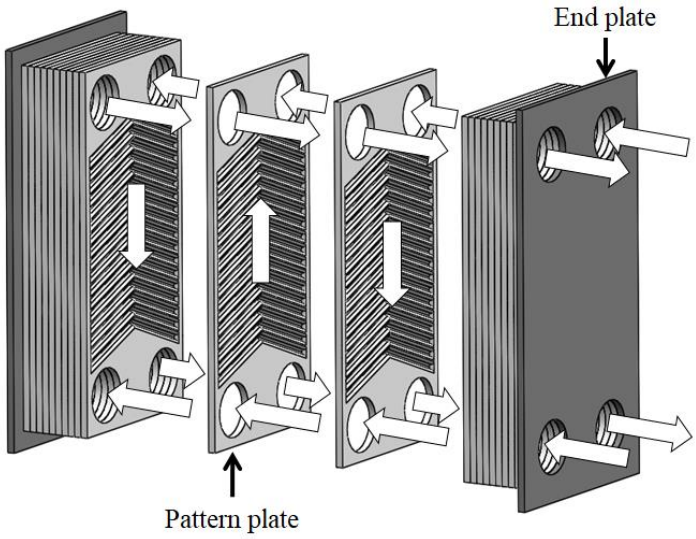

Figure 2-3: Plate-and-frame heat exchanger structure concept

2.2.3. Shell-and-tube heat exchanger

Shell-and-tube heat exchangers (Figure 2-4) are the most common type used in industry. The tube diameters vary from 0.625” to 1.5” (~16 mm to 38 mm) in conventional heat exchangers. These heat exchangers have very low surface area to volume ratio and hence are generally not economical for high-temperature and high-pressure applications. Chordia et al. [10], however, developed a shell-and-tube heat exchanger with a large number of tubes of diameter close to 1 mm to achieve small wall thickness and very high surface area to volume ratio. Since the channels are on the order of millimeters or less, the heat exchanger benefits from the high heat transfer. Since this type of heat exchanger can handle more severe conditions and higher pressures and temperatures, it can be used in gas turbine systems if there is no space limitation. It can also be used as a high temperature gas-cooled reactor for nuclear heat utilization.

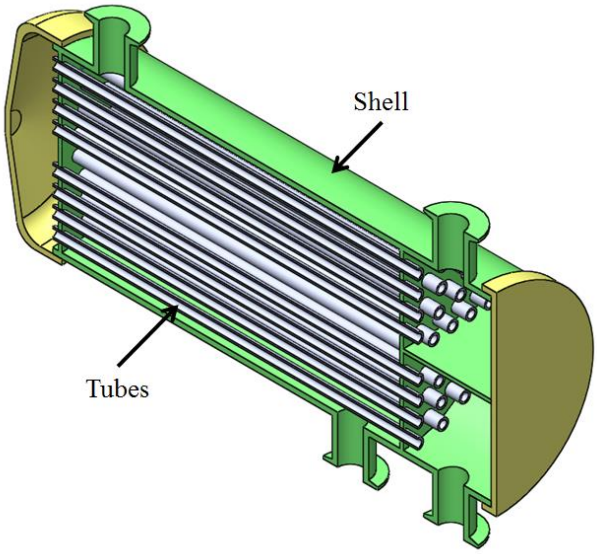

Figure 2-4: Shell-and-tube heat exchanger structure concept

2.3. Examples of HTHX Demonstrations

High temperature heat exchangers have several applications ranging from aerospace, waste heat recovery, nuclear heat utilization, exhaust gas recuperators, and as primary heaters and recuperators in advanced high efficiency power cycles such as supercritical CO_2 Brayton cycle. The present section reviews some of the applications of the HTHXs currently being used or developed.

2.3.1. Recuperator for gas turbine power generation

For over half a century, gas turbines have been widely used in power plants and aircraft propulsion, in which heat exchangers have always played an important role. The heat exchanger serves as a recuperator, which preheats compressed air before it enters the combustor by recovering heat from exhaust gas. Thus, the gas turbine

cycle efficiency can be increased and fuel consumption can be reduced [59]. For this application, the typical compressor exit gas temperature can be as high as 725°C, which requires an HTHX as the recuperator [4]. Three major types of recuperators in gas turbine systems are used: PFHXs, plate-and-frame heat exchangers, and shell-and-tube heat exchangers [60].

For an optimized gas turbine cycle, whose inlet gas/air temperature is 825°C/ 521°C and pressure ratio is 24.3, Aquaro [7] proposed a PFHX fabricated from superalloy with increased fin thickness of 0.15 mm on the air side to withstand the pressure at these maximum operating temperatures. A PFHX designed by Toyo [61] was used as a recuperator with effectiveness of about 90% in intercooled and recuperated micro gas turbines at about 650°C under inlet pressure about 400 kPa. Similar to the external shape of the PFHX design from Toyo, Ingersoll-Rand [62] also developed a plate-fin recuperator, which adopts offset fins in the heat transfer area, operates at 700°C with effectiveness of about 90%, and has a cycle pressure ratio up to 14. AlliedSignal (Honeywell's predecessor) [63, 64] produced a compact plate-fin ceramic recuperator for a cruise-missile propulsion application, and an industrial gas-turbine plate-fin recuperator (effectiveness of 84-89%) with offset plate-fin surfaces which operates at 510 – 575°C and has a pressure ratio of 10.

A plate-and-frame type recuperator with effectiveness of about 90% and operating temperature of 650°C has been developed by Rekuperator Svenska AB (RSAB) [65] for application in a micro gas turbine power plant for combined electricity and heat generation. Another welded plate-and-frame counter-flow recuperator was developed by Honeywell [66]. A plate-and-frame recuperator with effectiveness of

90% was designed by Wilson et al. [67] using silicon carbide, which improved the overall thermal efficiency from 27% to over 40%, since the material can withstand inlet hot gas temperature of 955°C.

Oak Ridge National Laboratory [58] developed an annular plate-and-frame recuperator which can withstand inlet gas temperatures as high as 850°C, inlet pressure of 690 kPa, and offers benefits from minimal ducting of the system. Another counter-flow annular plate-and-frame recuperator with effectiveness of 90% and operating temperature of 725°C was designed by ACTE [68]. Rolls-Royce [69] also developed a spiral recuperator which operated with pressure ratio up to 14 and effectiveness up to 92%.

In addition to plate-and-frame heat exchangers and PFHXs, shell-and-tube heat exchangers are commonly used in gas turbine systems if size is not the limiting factor. Proe Power Systems [70] developed the Proe 90TM shell-and-tube recuperator, which operates with maximum temperature of 891°C and maximum inlet pressure of 621 kPa, and has a predicted heat duty of 30 kW, effectiveness of 95%, and relatively low pressure drop (1-6 kPa). Schönenborn et al. [71] also developed a cross-counter flow recuperator, which operates with maximum temperature of 671°C and maximum inlet pressure of 3091 kPa. This recuperator was fabricated with two manifold tubes and a bundle of profile tubes using Iconel 625. However, the estimated total weight of this shell-and-tube type recuperator was about 1,000 kg per engine, which clearly adds too much weight to the engine system on aircraft [4].

2.3.2. Intermediate heat exchanger for nuclear heat utilization

Another application of HTHXs is nuclear heat utilization. For nuclear power plants, the heat exchangers must be both economically competitive and meet stringent safety requirements. Excellent safety characteristics can be achieved with high temperature gas-cooled reactors (HTGRs), since HTGRs have high heat capacity with their graphite core and high chemical stability with helium as the coolant [7]. However, to transfer the nuclear heat to the end user's facility, such as a hydrogen production or steam reforming system, a high temperature intermediate heat exchanger (IHX), which may use He as the working fluid on both sides and must operate above 900°C, is needed [39]. In the 1980s, a shell-and-tube He/He IHX was designed and constructed in Germany with a heat duty of 10 MW, which successfully ran some tests for several months up to 950°C [64, 72]. Another 10 MW He/He IHX based on the shell-and-tube design was designed in Japan to operate at temperatures above 900°C [9]. The IHX is a vertical helically coiled counter-flow heat exchanger. Primary He enters from the bottom at 950°C with inlet pressure of 4 MPa, while secondary He enters from top at 200°C with inlet pressure of 4.1 MPa. To minimize constraints of axial and radial thermal expansions on the tubes, a floating hot header with a combination of a central hot gas duct was adopted which passes through the central space inside the helix bundle.

2.3.3. High temperature prime heat exchanger in externally fired systems

An externally fired combustion process takes place at atmospheric pressure outside the working fluid operating cycle. Generally, an externally fired system may have hot combustion temperatures of 1500°C and higher [73]. Therefore, an HTHX is required to transfer heat from combustion to the gas turbine working fluid, which may have pressure up to 17 bar for a gas turbine or 250 bar or higher for a supercritical CO_2 power generation cycle. As the heat exchanger has to withstand the stresses imposed by the working conditions and the constituents in the combustion gases, a shell-and-tube heat exchanger may generally be the preferred candidate for externally fired systems [74].

One such HTHX is presented by K. A. Al-Attab [75]. In this biomass fuel powered system, a two-pass cross-flow heat exchanger with baffle shells and tubes was chosen to transfer the combustion heat to the compressed air. Due to the selected material, stainless steel, the maximum turbine inlet temperature was limited to 694°C. If a nickel-based superalloy had been used for the heat exchanger's fabrication, a maximum turbine inlet temperature of 800 – 825°C may have been reached [74].

2.3.4. Pre-cooler for aircraft environmental control system applications

The environmental control system is used in aircrafts to maintain a comfortable closed environment by keeping temperature within acceptable limits. Hot bleed air from the engine compressor, which has temperature of 500 to 750°C is precooled using HTHX, so that it can circulate within the various systems of the aircraft for

other usage [76-78]. The pre-coolers are typically compact PFHXs that have relatively high heat transfer surface area per volume ratios. Since weight is a critical design point for components on aircraft, a plate-fin carbon-carbon heat exchanger operating at 650°C was designed by Stevenson et al. [2]. This HTHX achieved about 40% mass reduction over a common metallic HTHX. However, multi-component coatings were needed for this carbon-carbon heat exchanger to avoid the oxidation issue at this operating temperature.

2.3.5. High temperature industrial waste heat recovery

Industrial waste heat refers to the energy generated as a byproduct in industrial processes that otherwise is not put to useful practical use. Examples of high temperature waste heat sources with temperatures of more than 500°C include metal refining/heating furnaces, hydrogen plants, and glass melting furnaces. For example, exhaust gases leaving the reverberatory furnace, which are frequently used in aluminum melting operations, usually have temperatures from 600 to 1300°C, and 40-60% of furnace energy input can be carried way with these exhaust gases. HTHXs can be utilized to recover most or a good portion of this waste heat and improve the total cycle efficiency.

2.4. HTHX Fabrication using Advanced Manufacturing Techniques

Processing, machining, welding and brazing of superalloys is difficult due to their higher toughness, low thermal conductivity, tendency to crack during welding, or the unavailability of suitable brazing materials [46, 47, 79]. Specialized equipment and highly trained operators are often needed for processing such materials.

However, new developments in advanced manufacturing techniques such as 3-D printing can address the challenges faced by conventional manufacturing. This section discusses HTHXs fabricated using various advanced manufacturing techniques such as additive manufacturing and photo-chemical etching processes.

2.4.1. Additive manufacturing

Additive manufacturing (AM), also known as 3-D printing, emerged nearly three decades ago and was initially used mainly for quick prototyping and production of specialized parts. However, due to its high degree of freedom, especially for fabrication of complex parts, there has been significant development of industrial-scale 3-D printers since then. 3-D printers now can print various metals, ceramics, and other tough-to-machine materials. As a result, AM has evolved from prototyping purposes to production of complex parts used in industries such as aerospace, biomedical, oil and gas.

There are three major metal-based AM techniques: selective laser melting (SLM), direct metal laser sintering (DMLS), and electron beam melting (EBM). SLM and DMLS printers usually consist of two platforms. The first platform is a powder dispenser platform that houses the metal powder. The second platform is the build platform on which the 3-D structure is built. After a layer of the 3-D structure is built, the powder dispenser platform rises while the build platform lowers, so a new layer of powder can be distributed on top of the existing layer. A re-coater arm is used to uniformly distribute the metal powder, as shown in Figure 2-5. In the case of DMLS, the metal powder is sintered using a laser just below its melting

temperature. For the case of SLM, the powder is completely melted. Lenses focus the laser beam while a scanning mirror controls the beam or spot location based on a slicing of the 3-D structure CAD file. The process is repeated until the entire 3-D structure is built. The EBM process is similar to that of SLM. The major difference is that an electron beam is used instead of a laser to melt the powder. Due to the use of the high-power electron beam, parts fabricated using EBM will have better mechanical strength than parts fabricated using the SLM or DMLS process.

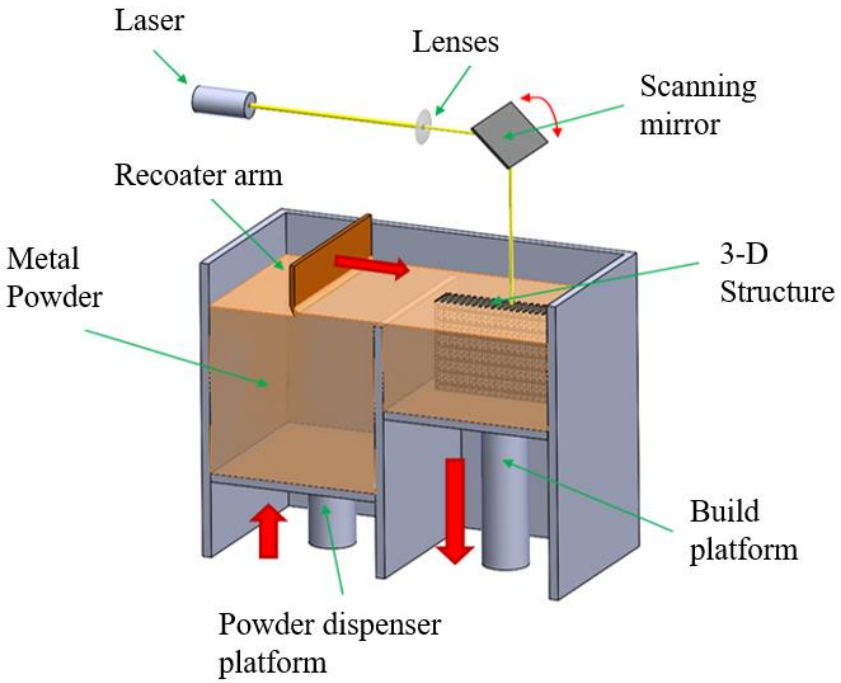

Figure 2-5: DMLS / SLM concept [80]

Laminated object manufacturing (LOM) is another AM technique capable of fabricating metal heat exchangers. In the LOM process, a 3-D structure is built layer by layer by cutting a sheet of material using a laser. A heated roller bonds the build part in the current layer onto the previous layer. The process is repeated until the entire 3-D structure is built. Compared to DMLS and SLM, the LOM process is

simpler and cheaper. In addition, LOM can be used to fabricate ceramic heat exchangers. However, the finish quality and accuracy of LOM are not as good as DMLS or SLM.

Additive manufacturing can help fabricate the complex and compact geometries of HTHXs which are otherwise almost impossible to fabricate. Several superalloys such as Inconel 718 and Inconel 625 are compatible with AM. It also allows fabrication of the heat exchanger as a single component, which eliminates the need to weld or braze different parts. There have been a couple of successful attempts to fabricate HTHXs using AM, as summarized below.

1. Multi-furcating heat exchanger

A 3-D printed HTHX was developed by Gerstler and Erno [34] from General Electric Global Research. They successfully fabricated multi-furcating heat exchangers using SLM for fuel-cooled oil cooler applications. The heat exchanger surfaces were fabricated using four different materials: aluminum, titanium alloy (Ti64), cobalt chrome, and Inconel 718. The test results showed that the heat exchangers met the pressure drop and heat transfer design requirement with 66% lower weight and 50% lower volume than the conventional heat exchangers.

2. Advanced fin-and-tube heat exchanger

In another study at University of Maryland, in collaboration with Oak Ridge National Laboratory (ORNL) [36], a novel fin-and-tube heat exchanger was

successfully fabricated out of titanium using DMLS. The heat exchanger has a complex fin geometry which cannot be economically fabricated using conventional manufacturing methods.

3. Novel air-to-water heat exchanger

Arie et al. [16] reported a novel air-to-water heat exchanger design fabricated through the DMLS process using different materials such as aluminium alloy (AlSi10Mg), stainless steel (SS17-4), and titanium alloy (Ti64). A fin thickness of 220 μm on the air side was also claimed as the minimum feature inside the heat exchanger fabricated using DMLS. Arie et al. [35] also developed another air-to-water polymer heat exchanger made from thin polyethylene sheets using layer-by-layer line welding and showed superior air-side performance over a plane plate fin surface.

2.4.2. Photo-chemical etching

Photo-chemical etching is a fabrication process that utilizes a photoresist and etchants to machine away a certain area of a metal plate. The process was initially developed for fabrication of printed circuit boards. However, due to its ability to etch various metals, including titanium, nickel superalloy, and copper superalloy, and its high accuracy, the process has been used to fabricate printed circuit heat exchangers.

During the etching process, first, a photoresist layer is deposited on the metal surface. Then, the photoresist is exposed to UV light via a photo-tool. Afterward,

the exposed metal is dissolved via an etching process to form semi-circular channels with typical channel width of 0.5-2 mm [81]. Lastly, the photoresist is removed using a solution like alkaline. If the photo-tool specifies the area that needs to be dissolved by the UV light, the process is called positive-working photoresist. If the photo-tool specifies the area that is left, the process is called negative-working photoresist.

Photo-chemical etching has been extensively used to fabricate printed circuit heat exchangers (PCHEs). The design consists of stacked plates with fine grooves etched into each plate. The stacked plates are usually bonded using a diffusion bonding technique. The common flow configurations of PCHE include counter-flow, cross-flow, and cross-counter-flow. Some PCHEs are claimed to withstand a maximum design pressure of 900 bars and temperatures up to 980°C [82]. Heatric [83] has successfully marketed a printed circuit heat exchanger fabricated using photo-chemical etching and diffusion bonding.

PCHEs achieve high thermal performance and are compact due to the smaller channel geometries. However, they incur larger pressure drops due to the long straight microchannels. The chemical etching process itself is expensive for the high temperature materials, as they are tough to etch. This makes these heat exchangers relatively expensive, especially for higher temperature applications. The low mass-based heat transfer density (kW/kg) and high cost of such heat exchangers has been a challenge for their adaptation in high temperature (>600°C) applications.

2.5. Comparison of Selected HTHXs

Table 2-1 compares state-of-the art HTHXs. As seen in the table, for the listed heat exchangers, the shell-and-tube heat exchangers offer the highest maximum temperature and pressure. Shell-and-tube heat exchangers also benefit from being well researched and widely used in a diverse range of applications with good reliability. However, they are usually bulky and heavy due to their low heat transfer density. Plate-and-frame heat exchangers and plate-fin heat exchangers offer higher heat transfer density than shell-and-tube heat exchangers, although they need to operate at lower temperature and pressure. In addition, recent development of printed circuit heat exchangers has resulted in compact heat exchangers with very high heat transfer density. However, the high pressure drop of the printed circuit heat exchanger is the major limitation for many applications where pumping power is constrained.

Table 2-1 State-of-the-art heat exchanger comparison

	A_{heat}/V (m^2/m^3)	T_{max} (℃)	$Pressure_{max}$ (bar)	Ref
Shell-and-tube heat exchanger	50 – 100	1100	1000	[57]
Plate-and-frame heat exchanger	120 – 660	815	200	[57]
Plate-fin heat exchanger	800 – 1500	800	200	[10, 11]
Printed circuit heat exchanger	200 – 2500	980	900	[10, 82]

2.6. Summary

Cost effective high temperature heat exchangers are key to the success of emerging high-temperature, high-efficiency modular power cycles for diverse applications of energy conversion, power generation and energy/waste heat recovery applications. Most common heat exchangers currently available in the market are the plate-fin, plate-and-frame, and shell-and-tube types. The ideal high temperature heat exchanger would offer an optimum balance among heat transfer effectiveness, pressure drop, size and weight (indirectly controlling the cost) of the heat exchanger, while meeting longevity and reliability requirements. For elevated temperatures, most heat-resistant superalloys that can withstand the required temperature suffer from low thermal conductivity and high cost. Therefore, innovative design and manufacturing techniques are crucial to successful development of such heat exchangers. While additive manufacturing of superalloys for high temperature applications faces numerous challenges, it is believed that additional research support in this field can overcome many of the challenges. Significant progress has already been made in the past few years and demonstrates the potential of AM for fabrication of high temperature heat exchangers. In the next chapter, a high temperature gas-to-gas heat exchanger's conceptual design, which incorporates the manifold-microchannel technology and has the potential to be fabricated through AM, will be discussed.

Chapter 3: Conceptual Design

3.1. Introduction

This chapter discusses the design requirements for the high temperature gas-to-gas heat exchanger. The concepts behind the design of the metallic heat exchanger surfaces (manifold-microchannel technology) are also explained. For the heat exchanger design, a gas-to-gas cross-flow heat exchanger with manifold-microchannel on both hot and cold sides was proposed.

3.2. Design Requirements

The design requirements were provided by an aerospace company for an aerospace turbofan pre-cooler. The current conventional design is based on a compact plate-fin heat exchanger that incorporates the microchannel technology. The detailed design specifications including overall volume, build material, mass flow rates, inlet temperatures, system pressures, and pressure drops on both hot- and cold-sides are shown in Table 3-1 and Table 3-2.

Table 3-1 Physical specifications

Overall Volume	≤ 125 in^3 (0.002 m^3)
Cold-flow Length	≤ 5 in (0.127 m)
No-flow Length	≤ 5 in (0.127 m)
Weight	≤ 10 lb (4.54 kg)
Material	Inconel 718

Table 3-2 Operation specifications for full-scale heat exchanger

Parameter		**Unit**	**Nominal Condition**
Hot Side	Flow Rate	lb/min (kg/s)	10 (0.076)
	Temperature	°F (°C)	1200 (649)
	Pressure	psia (kPa)	64.7 (448)
	Pressure Drop	psid (kPa)	2.6 (18)
Cold Side	Flow Rate	lb/min (kg/s)	10 (0.076)
	Temperature	°F (°C)	100 (38)
	Pressure	psia (kPa)	14.7 (101)
	Pressure Drop	psid (kPa)	0.3 (2)

3.3. Manifold-microchannel Technology

The manifold-microchannel technology was first proposed by Harpole and Eninger [13] in 1991. The main advantage of this technology is that a high heat thermal performance can be achieved without significant increase in pressure drop as reported in [84].

The manifold-microchannel concept involves a flow guiding system called manifold positioned over microchannels as shown in Figure 3-1. The purpose of the manifold is to distribute and deliver the flow into multiple short microchannels. As shown in the figure, the flow first enters through the manifold channels, then is distributed into the microchannels where travels a short length before it is guided out. Due to the short flow length in the microchannels, the flow is typically in the

thermally developing regions, resulting in substantially higher heat transfer coefficients. In addition, a short flow length in microchannels can also reduce pressure drop, which in turn, reduces the pumping power requirement. The study from Cetegen [84] shows that for the same heat transfer rate, pressure drop in a channel can be reduced by a factor of N^2, where N is the number of channel segments.

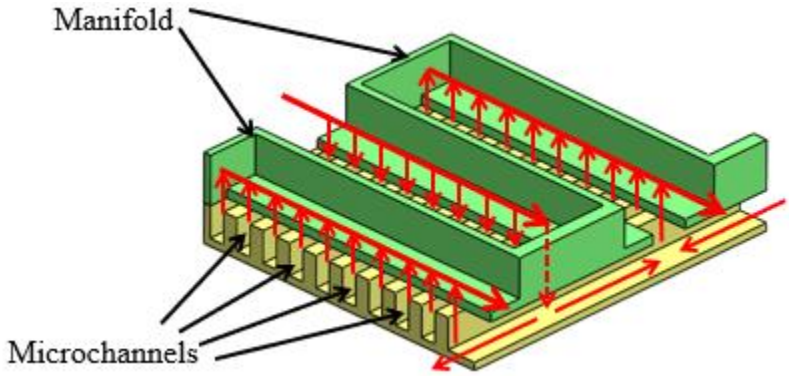

Figure 3-1: Manifold-microchannel concept

By studying the behavior of the flow along the microchannel in a U-shape path when it enters and exits, Copeland et al. [85] created a 3-D CFD simulation for the microchannel section which is part of a manifold-microchannel heat sink as shown in Figure 3-2. The model used water as the working fluid and silicon as solid material for fins and base. It was also assumed uniform laminar flow distribution in all channels. With different combinations of manifold channel pitches, microchannel depth, microchannel widths, and channel flow velocity (inlet velocity ranging from 0.1 m/s to 1.0 m/s), pressure drops in the range of 47 – 12,260 Pa and thermal resistance of 0.25 – 1.85 ºC/W were observed. Another 3-D CFD

simulation work by Ng and Poh [86, 87] also considered only the microchannel section, and assumed uniform flow in all microchannels. By using water as the working fluid, they observed pressure drops in the range of 45 – 10,209 Pa and thermal resistance of 0.53 – 6.66 ºC/W with inlet velocity of 0.1 – 1.0 m/s.

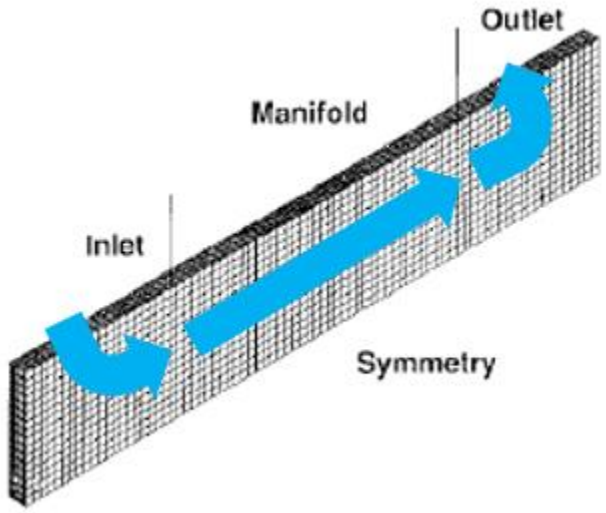

Figure 3-2: Microchannel computational domain by Copeland et al. [85]

In another study, Kim et al. [88] conducted experimental tests on manifold-microchannel for forced air cooling with a design consisting of manifold and multiple microchannels. The heat sink was made of silicon, and air was used as the working fluid. The experiment results revealed that compared to microchannel heat sink, 35% reduction on thermal resistance was possible with using manifold-microchannel.

A 3-D CFD simulation study of a manifold-microchannel heat sink was reported by Ryu et al. [89]. The model included a single manifold-microchannel segment with a portion of the inlet and outlet manifold channels as shown in Figure 3-3.

Copper was chosen as the material of the solid part, and water was used as the working fluid. The results showed that compared to traditional microchannel heat sinks, manifold-microchannel technique can reduce thermal resistance by half, and improve temperature uniformity along the channel.

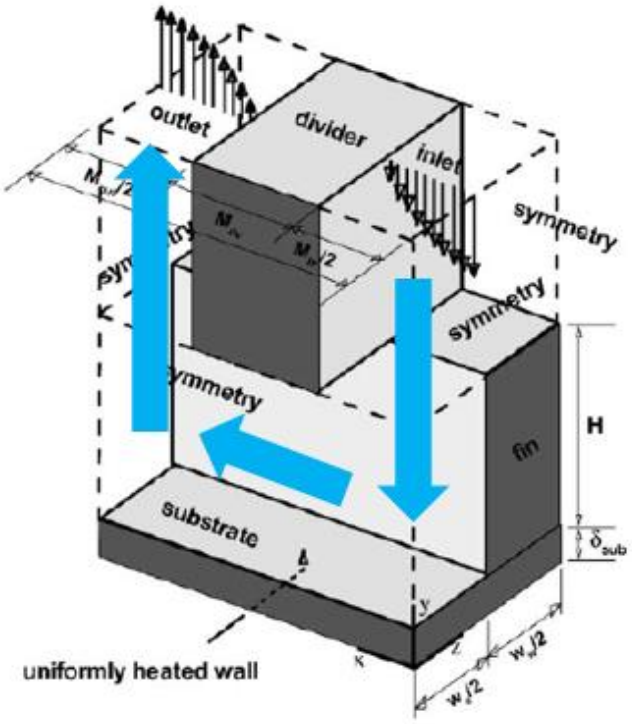

Figure 3-3: Single manifold-microchannel segment computational domain by Ryu et al. [89]

A small manifold-microchannel heat sink was designed by Wang et al. [90], and a 3-D CFD modeling was performed. The heat exchanger design had only 30 microchannels, and copper was used as the solid material. By using water as the working fluid, the simulation results showed that manifold-microchannel design could deliver better temperature distribution compared to microchannel heat sink and an increase in heat transfer by 75% was obtained.

A combined numerical and experimental study on a manifold-microchannel heat sink was performed by Escher et al. [91]. Water was used as the working fluid and silicon was selected as the fin and base material. To simplify the numerical model, porous media was used to replace the microchannel section. Anisotropic permeability was applied to account for the resistance of the microchannels. The simulation results matched with the experimental results to some degree. The results also showed that a thermal resistance of 0.09 cm^2K/W with a corresponding pressure drop of 0.22 bar was possible for a 2 x 2 cm^2 system.

Cetegen [84] created a multi-objective optimization for a manifold-microchannel heat sink design. The numerical model only simulated a single manifold-microchannel segment, and copper was used as the solid material and water as the working fluid. The simulation results showed that for the same pumping power, the manifold-microchannel heat sink may provide 72% higher heat transfer coefficient than a traditional microchannel heat sink, or 306% higher heat transfer coefficient than a jet impingement heat sink. Cetegen also conducted several single-phase and multi-phase heat transfer experiments using a manifold-microchannel heat sink which showed significant performance improvement compared to other conventional heat sink technologies.

Boteler et al. [92] carried out a numerical investigation on manifold-microchannel heat sink which included both the manifold and microchannel section. Different models with 2 to 20 microchannels were studied. A model with 10 microchannels is shown in Figure 3-4. The numerical results showed that the manifold-

microchannel heat sink yielded a 97% reduction on pressure drop and could provide better temperature distribution compared to a conventional microchannel heat sink.

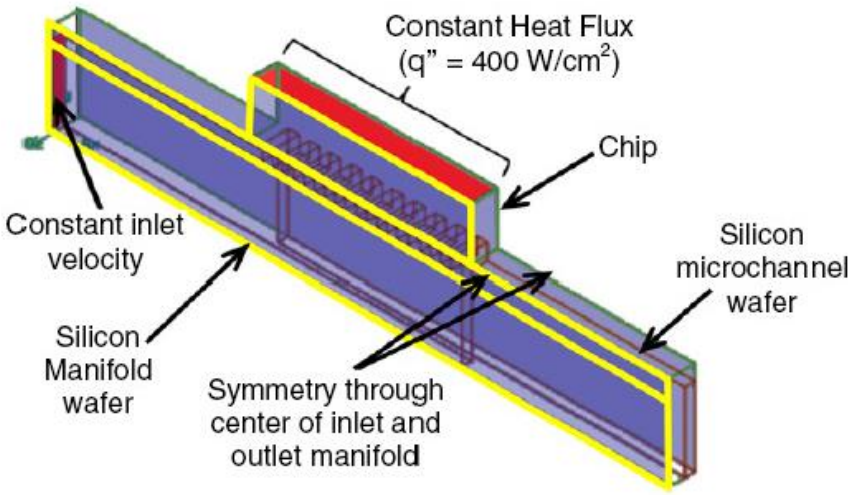

Figure 3-4: Manifold-microchannel computational domain by Boteler et al. [93]

Mandel et al. studied the implementation of manifold-microchannel for high heat flux electronic cooling applications [94]. Several manifold-microchannel heat sinks were fabricated and tested using R245fa as the refrigerant. The experimental results showed that high heat transfer coefficient of 40 kW/m^{2}K-140 kW/m^{2}K at pressure drops of 10 kPa-50 kPa could be achieved by forcing thin film evaporation on the microchannel in two-phase regime.

Another study regarding manifold-microchannel's implementation for low heat flux applications was performed by Andhare et al. [26]. A water-to-water manifold-microchannel plate heat exchanger was successfully fabricated and tested. The experimental results showed that with a pressure drop per length value of 5.85

bar/m, an overall heat transfer coefficient close to 20 kW/m^{2}K was achieved for a flow rate of 20 g/s.

Arie [80] successfully developed a hybrid numerical method to predict the performance of air-to-water manifold-microchannel heat exchanger, and fabricated a heat exchanger where manifold-microchannel concept was implemented on the air-side (the design concept is shown in Figure 3-5). The numerical and experimental results showed that manifold-microchannel plate heat exchanger could yield significant performance improvement compared to conventional plate heat exchangers.

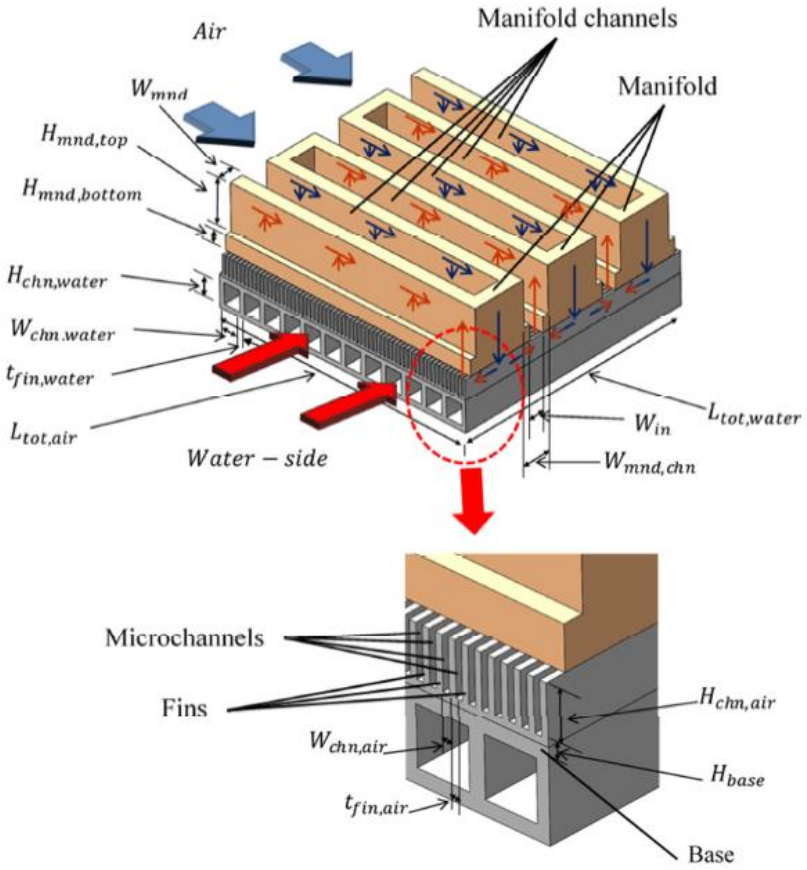

Figure 3-5: Air-to-water manifold-microchannel design concept by Arie [80]

Although many studies have been reported regarding the performance improvement using manifold-microchannel technology, they were mostly focused on heat sink design used for chip cooling application. Even one study tried to implement manifold-microchannels in the air-side of an air-to-water heat exchanger, the heat exchanger was only used for drying cooling application under low-temperature (~ 40ºC on air-side & ~ 67.5ºC on water-side) operation conditions.

3.4. Gas-to-gas Cross-flow Heat Exchanger Conceptual Design

Since manifold-microchannel technology has not been implemented in a gas-to-gas application such as air-to-air heat exchangers used on aircraft where weight reduction is as important as performance enhancement, the proposed high temperature gas-to-gas heat exchanger's conceptual design consists of manifold-microchannels on both hot and cold sides in a cross-flow configuration as shown in Figure 3-6 (a). As discussed in the previous section, manifold-microchannel technology involves adding system of manifolds on top of the microchannels to reduce the flow length along each microchannel. Pumping power can be then reduced since reduced flow length would result in reduced pressure drop across the heat exchanger. At the same time, increased heat transfer performance can be expected as the flow is still in the developing region due to the short flow length. Since manifold-microchannel can improve the heat transfer performance and reduce the pumping power, by applying manifold-microchannels on both gas sides for the conceptual design, a weight reduction compared to conventional heat exchanger with the same performance can be expected. The complete heat

exchanger may be composed of several layers stacked vertically as shown in Figure 3-6 (b).

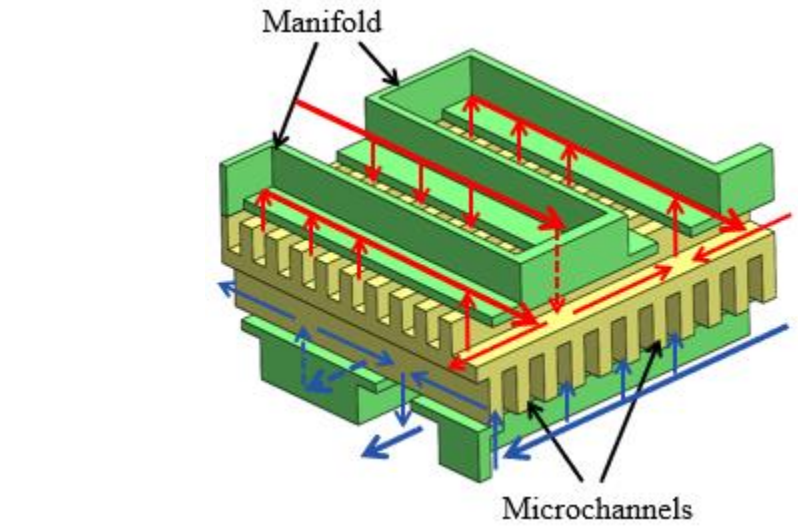

(a)

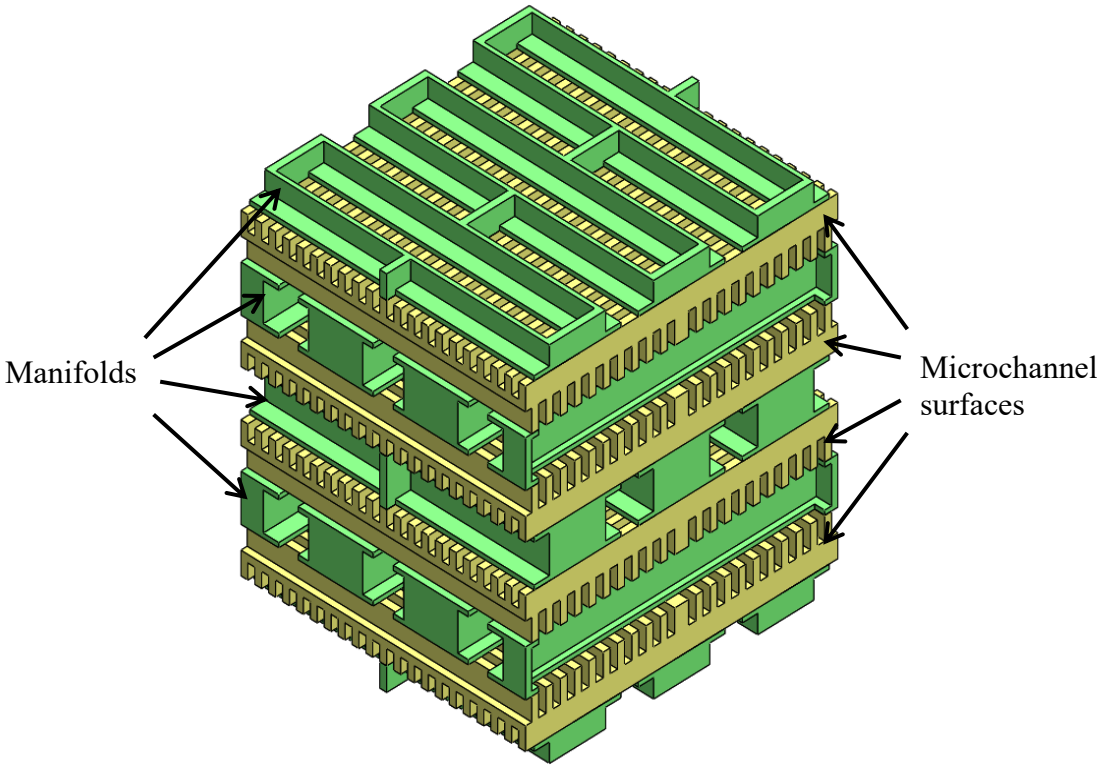

(b)

Figure 3-6: Advanced gas-to-gas heat exchanger conceptual design (a); multi-layer manifold-microchannel heat exchanger concept (b)

3.5. Summary

In this chapter the design requirements for the high temperature heat exchanger were presented based on the operating and physical specifications provided by an aerospace company for an aerospace turbofan pre-cooler prototype which is conventionally based on compact plate-fin heat exchangers that incorporate microchannel technology. In addition, the rationality behind adoption of the manifold-microchannel technology were explained. With reduced flow length, higher heat transfer coefficients and lower pressure drops can be achieved with the same flow rate compared to conventional heat transfer geometries such as plate-fin or microchannel technique. Considering the proposed gas-to-gas high temperature heat exchanger's conceptual design consisted of manifold-microchannels on both the hot and cold side in a cross-flow configuration, the fabrication alternatives for such complex gas-to-gas high temperature heat exchangers will be discussed in the next chapter.

Chapter 4: Fabrication Alternatives

4.1. Introduction

This chapter discusses the fabrication alternatives for the gas-to-gas cross-flow manifold-microchannel heat exchanger such as direct metal laser sintering, photo-chemical etching, laser micro-machining, and diffusion bonding. The fabrication principles and the limitations of the techniques are discussed in detail. The presented information in this chapter aims to provide the rationality for adopting additive manufacturing as the fabrication method of the choice.

4.2. Direct Metal Laser Sintering

Direct metal laser sintering (DMLS) is a metal powder based additive manufacturing process. A computer-controlled laser is used to sinter the metal powder based on a pre-programmed geometry (usually a STL file of the CAD model) to build a 3-D structure layer by layer. DMLS was first developed by EOS GmbH of Munich, Germany [95], and now is one of the most common additive manufacturing methods for metallic structures in United States. A DMLS machine generally consists of two platforms: a powder dispenser platform to house the metal powder, and a build platform on which the 3-D structure is being fabricated. When printing of a layer of the 3-D structure is completed, the powder dispenser platform will rise, and the build platform will lower down at the same time. By doing so, a new layer of metal powder can be evenly distributed on top of the previous layer through a re-coater arm. Based on the pre-programmed geometry, a scanning mirror

controls the laser to sinter the powder and build a cross section of 3-D structure on the new layer. The process is repeated until the entire 3-D structure is fabricated.

Since it emerged as a new manufacturing technique, DMLS process has been improved significantly over the past decade. The minimum feature size that can be currently fabricated through DMLS is about 200 – 300 μm with a normal-resolution machine or 150 μm with a high-resolution machine. A list of the fabrication limitations and tolerances is given in Table 4-1 based on three top DMLS-service-provider companies in United States (Proto Labs, Stratasys, and 3D Systems). Considering DMLS's good compatibility with common heat exchanger materials (such as Aluminum, Stainless Steel, and Inconel) and its capability to fabricate complex geometry which may be difficult or impossible through conventional manufacturing technique, the fabrication method shows promise to be implemented for both manifold and microchannel surface's fabrication.

Based on the communications with all three DMLS-service-provider companies (Proto Labs, Stratasys, and 3D Systems), it was concluded that to avoid any warpage on the manifold wall (shown in Figure 4-1) and also thermal short circuit between incoming and outgoing flows, the minimum manifold wall thickness needs to be 500 μm. A minimum manifold base thickness of 1 mm is also needed if post-process will be applied to meet certain flatness requirement for assembly. Moreover, the minimum microchannel fin thickness needs to be 150 μm due to the minimum feature size constraint.

Table 4-1 DMLS limitations and tolerances

	Proto Labs [96]	**Stratasys** [97]	**3D Systems** [98]
Layer thickness	Normal resolution: 30 µm High resolution: 20 µm	Normal resolution: 40 µm	N/A
Minimum feature size	Normal resolution: 380 µm High resolution: 150 µm	Normal resolution: 300 µm	Normal resolution: 200 µm
Tolerance	± 76 µm	First inch: ± 127 µm Thereafter: ± 50 µm	± 50 µm
Maximum build size	Normal resolution: 246 × 246 × 274 mm^3 High resolution: 89 × 89 × 74 mm^3	N/A	Normal resolution: 275 × 275 × 420 mm^3

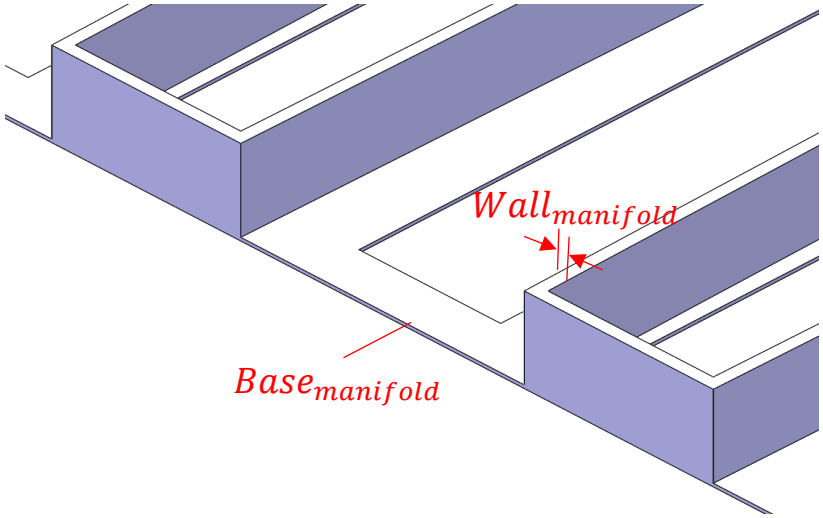

Figure 4-1: Manifold design layout

4.3. Photo-chemical Etching

Photo-chemical etching is a fabrication process which utilizes a photoresist mask and a liquid etchant to remove certain regions of a metal part. The process was initially developed for fabrication of printed circuit boards. However, due to its ability to etch various metals, the process is also commonly used to create microchannels in metal surfaces for printed circuit heat exchangers. As shown in Figure 4-2, during photo-chemical etching process, first the shape of the part is printed onto a photographic film. Then, photo-tool which is a sheet of photographic film showing negative images of the parts is prepared. Next, the metal sheet is laminated with a UV-sensitive photoresist. The coated metal is placed under the photo-tool. The plate is then exposed to UV light. After the plate is "developed", the unexposed resist is washed away. During etching, etchant reacts with the unprotected metal, and essentially corrodes it away. After neutralizing and rinsing, the remaining resist is removed, and the finished metal sheet is cleaned and dried. Photo-chemical etching is a process by which a concentrated acid is used to remove material to shape desired structure. However, since etching on metal materials is homogeneous, it is hard to fabricate microchannels with rectangular cross sections.

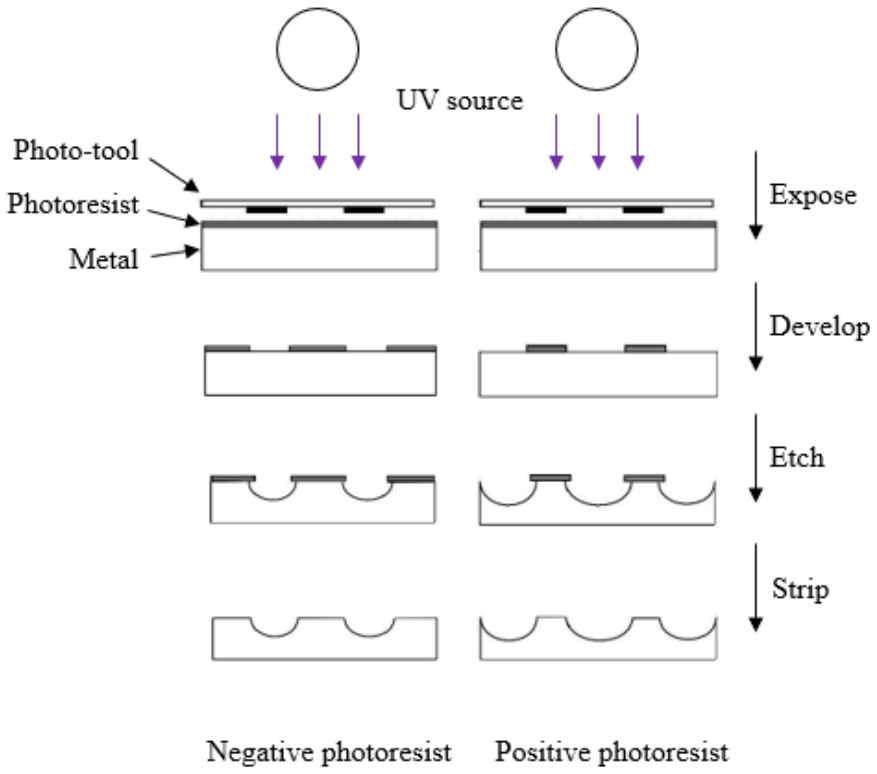

Figure 4-2: Photo-chemical etching process (adapted from reference [99])

Based on the communications with the photo-chemical etching company (ChemTec - A Division of ChemArt), to fabricate a double-side cross-flow microchannel surface through the etching process, the aspect ratio of the microchannel width to the microchannel height would be 1.1. The minimum microchannel fin thickness and the minimum microchannel width would be 80 µm. The total microchannel surface height, as shown in Figure 4-3, is greater than 0.013 mm and less than 2.032 mm. However, considerable effort will be needed if the etched double-side microchannel surface has to meet certain flatness requirement for assembly through post processing.

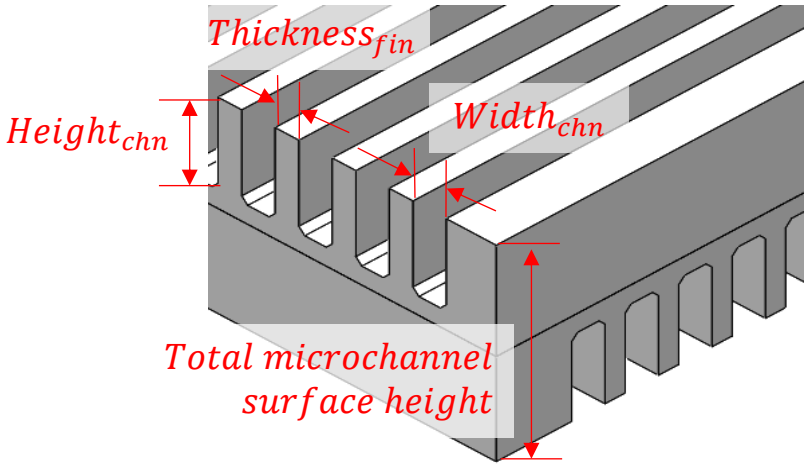

Figure 4-3: Microchannel surface design layout

4.4. Laser Micro-machining

Laser micro-machining is another approach to fabricate the double-side cross-flow microchannel surface. By applying a high-power laser beam, energy of the laser is converted to heat which vaporizes or melts the metal material to form the microchannel structure as shown in Figure 4-4 [100]. An assist gas or fluid is often utilized to improve the cut quality, expel molten metal, and minimize the heat affect zone. However, laser micro-machining is a very time-consuming process as it may take over 2 days to fabricate one 389 × 132 × 1.3 mm^3 size microchannel surface. Also, the maximum channel height would be 500 μm according to the communications with the laser micro-machining company (Potomac Laser).

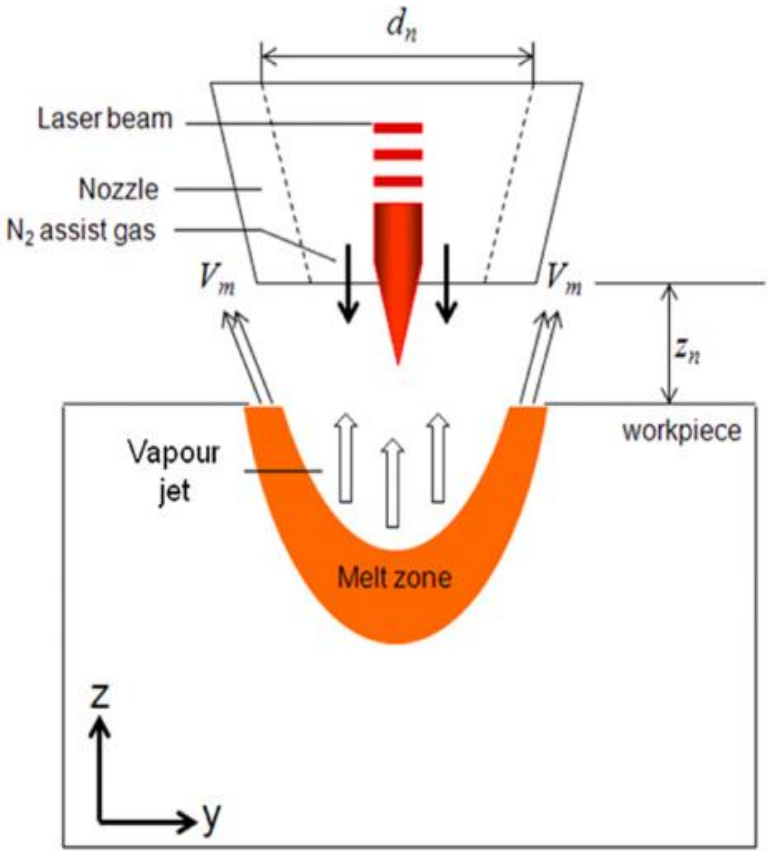

Figure 4-4: Laser micro-machining process concept [101]

4.5. Diffusion Bonding

As shown in Figure 4-5, diffusion bonding is a solid-state joining process by which two nominally flat surfaces are joined at an elevated temperature using an applied interfacial pressure for a period ranging from a few minutes to a few hours [102]. If manifold and microchannel surface are fabricated separately, diffusion bonding would be the best approach to assemble the parts. However, a thin bonding aid layer such as Ni-layer may be required for certain materials which may add additional thermal interfacial resistance to the assembled core. Due to the small size of the microchannels, improper bonding between the manifold and microchannels can

also cause clogging in the microchannels which can reduce the heat transfer performance and increase the pressure drop significantly. If diffusion bonding is used, in order to meet the parallel and flatness requirements for the bonding surfaces, considerable effort is needed to prepare the microchannel surfaces and manifolds.

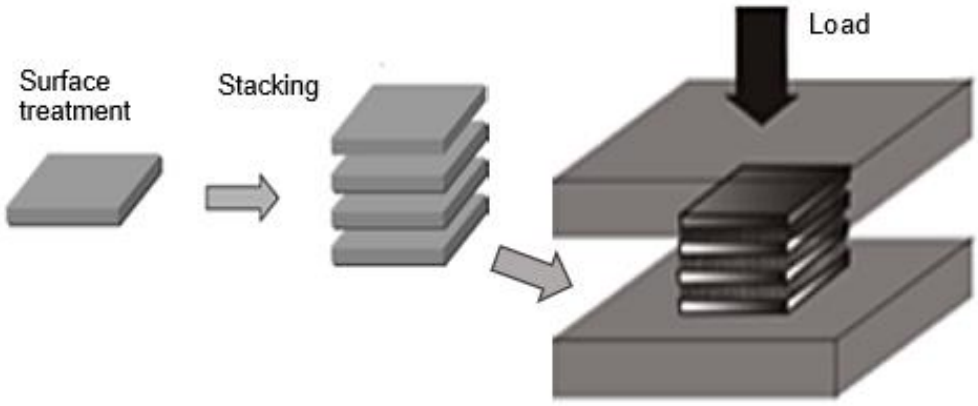

Figure 4-5: Diffusion bonding process concept [103]

Based on the communication with the diffusion bonding company (Vacuum Process Engineering), in order to ensure the bonding quality, the bonding surface's parallel needs to be 0.03 mm or better, and the surface's flatness needs to be 0.127 mm or better. Furthermore, microchannel surface needs to add 1 mm thick side bars on all 4 sides, and manifold also needs to add 1 mm thick side bars as shown in Figure 4-6 to provide enough bonding surface area.

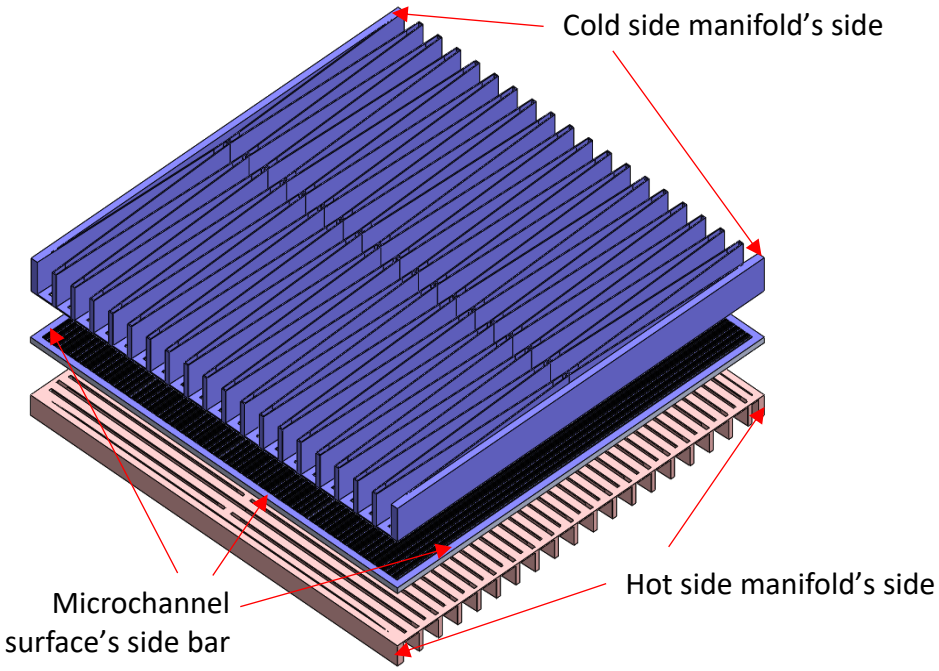

Figure 4-6: Exploded view of assembly design for one stack of cross-flow manifold-microchannel through diffusion bonding

4.6. Fabrication Alternatives Risk Assessment

As shown in Table 4-2, in order to choose the best fabrication approach for the gas-to-gas cross-flow manifold-microchannel heat exchanger, the limitations of the fabrication alternatives are summarised, and the risks of each fabrication alternative are assessed. Based on the risk assessment, it was concluded that if the heat exchanger is 3-D printed as a single unit, the assembly process can be avoided and the fabricating lead time can also be significantly shortened.

Table 4-2 Fabrication alternatives risk assessment

	Process	**Limitations**	**Risk Level**
Microchannel Surface	DMLS	• Metal powder may be remained in the microchannels due to small channel width and sintering heat from the fins • Minimum fin thickness is more than 150 μm • Minimum separating sheet thickness is about 500 μm	Moderate
	Photochemical etching	• Microchannel has a tolerance of 80 μm or more • Microchannel surface's flatness after etching is generally 10 mm, but flatness of 0.127 mm is possible with post process • Cannot get rectangular cross section for microchannel	Moderate
	Laser micromachining	• Cost is very expensive • Very slow process which may take over two days to fabricate a single $389 \times 132 \times 1.3$ mm^3 microchannel surface	Moderate
Manifold	DMLS	• Probably going to be some warp on the manifold base (if base thickness is 300 μm) due to the heat on the thin wall structure • Manifold base can be made thicker and be machined to meet the flatness requirement	Moderate
Assembly	Diffusion bonding	• Parallel and flatness required for both manifold base and microchannel surface are 0.03 mm and 0.127 mm respectively • May cause clogging in the microchannels	High
	DMLS	• If both manifold and microchannel surface are fabricated through DMLS, then it can be 3D printed as a single unit without assembly process	Low

4.7. Summary

This chapter discusses several fabrication options for the gas-to-gas cross-flow manifold-microchannel heat exchanger including direct metal laser sintering, photo-chemical etching, laser micro-machining, and diffusion bonding. The procedure for each technique is described and the associated limitations technique are discussed. A risk analysis was performed which indicated the additive manufacturing would be a better choice for the current design. In the next chapter, the optimization process which was performed to obtain the optimal heat exchanger design is discussed, and the identified manufacturing constraints are included to predict the performance of the heat exchangers produced through different fabrication methods.

Chapter 5: Optimization & Design Selection

5.1. Introduction

This chapter discusses about a single objective optimization process performed for the gas-to-gas cross-flow manifold-microchannel heat exchanger to find the optimal design which meets the design requirements as listed in chapter 3. The first goal of this optimization was to compare the predicted performance of the manifold-microchannel heat exchangers produced through different fabrication approaches. The second goal was for design selection. An optimal design, which meets all the design requirements and shows the best performance with the chosen fabrication approach, was identified and scaled down to a lab-scale unit so that it could be fabricated and tested.

5.2. Single Objective Optimization

A single objective optimization was performed to calculate the highest heat transfer performance of the manifold-microchannel heat exchanger for the given physical and operating conditions listed in chapter 3. The goal of the optimization is to maximize the heat duty (which is the same as to maximize the effectiveness) of the cross-flow heat exchanger. Based on the fabrication alternatives discussed in the previous chapter, the optimization was performed for three manufacturing process constraints: 3-D metal printing (DMLS), photo-chemical etching, and laser micro-machining.

The geometrical and performance constraints for all three manufacturing methods are shown in Table 5-1 for both hot and cold sides. The geometrical constraints were based on the manufacturing limitations as recommended by the manufacturers. These manufacturing limitations were also discussed in the previous chapter.

Table 5-1 Optimization constraints

	3-D Metal Printing	**Photo-chemical Etching**	**Laser Micro-machining**
Geometrical Constraints (hot and cold sides)			
Re_{mnd}	100-16,000		
H_{chn}/L_{front}	0.00236-0.0394	W_{chn}/1.1	≤0.00394
W_{chn}/t_{fin}	0.5-5		
W_{chn}/L_{front}	0.00157-0.00787		
$W_{mnd-chn}/L_{front}$	0.0315-0.0787		
$H_{mnd,top}/L_{front}$	0.00787-0.0787		
n	30-1000		
$W_{in}/W_{mnd-chn}$	0.1-0.9		
t_{fin}/L_{front}	≥0.00118	≥0.000630	≥0.000394
$H_{mnd,bottom}/L_{front}$	0.00236		
W_{mnd}/L_{front}	0.00394		
H_{base}/L_{front}	0.00236		
$(H_{chn,hot} + H_{chn,cold} + H_{base})/L_{front}$	N/A	0.000102-0.016	N/A
Performance Constraints			
$T_{in,hot}$	38° C		
$T_{in,cold}$	649°C		
Δp_{hot}	≤17.9 kPa		
Δp_{cold}	≤2.07 kPa		
$Re_{front,hot}$	18,000		
$Re_{front,cold}$	18,000		
V_{tot}	≤0.00205 m^3		

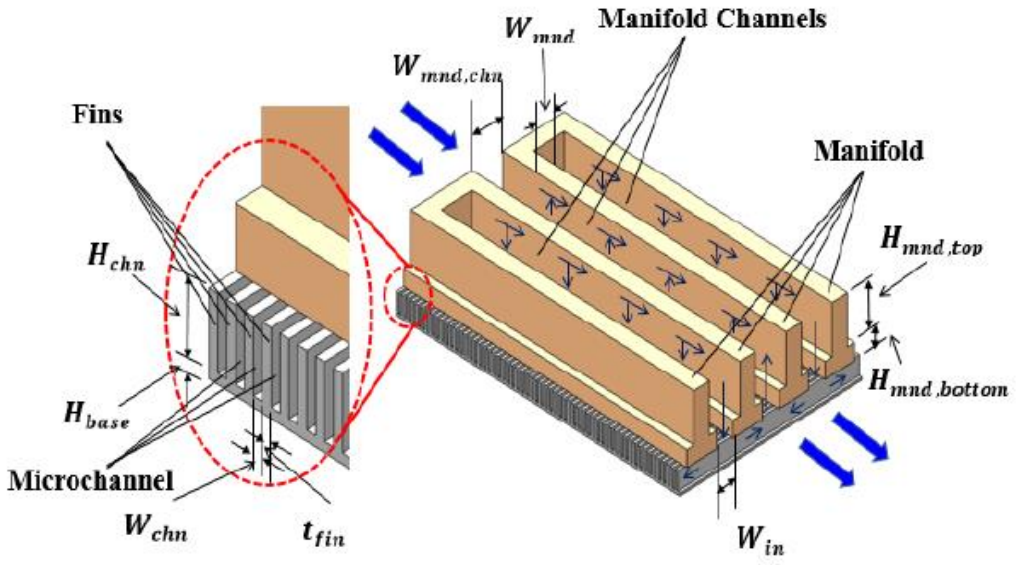

Figure 5-1: Manifold-microchannel design layout

As shown in Figure 5-1, the geometrical parameters are defined as manifold wall thickness (W_{mnd}), manifold channel width ($W_{mnd,chn}$), manifold channel height ($H_{mnd,top}$), manifold base thickness ($H_{mnd,bottom}$), manifold-to-microchannel inlet width (W_{in}, note: this is the width of the opening where either the flow enters from the manifold channel to the microchannels or the flow exits from the microchannels to the manifold channel), microchannel fin thickness (t_{fin}), microchannel width (W_{chn}), microchannel height (H_{chn}), microchannel base thickness (H_{base}, note: this is only for one side, which means the separating sheet thickness is $2H_{base}$), and microchannel numbers on one side (n). The geometrical constraints were normalized by the frontal area length scale (L_{front}) of 0.127 m. The frontal area length scale was calculated as $L_{front} = \sqrt[3]{V_{tot}}$ based on the maximum possible volume of the heat exchanger. The maximum heat exchanger volume (V_{tot}) is

0.00205 m^3 which was listed as the heat exchanger physical requirement in chapter 3. In addition to the geometrical constraints, the performance constraints based on the operating conditions were also included in Table 5-1, where Re_{front} is Reynold number calculated based on the frontal area and the mass flow rate as:

$$Re_{front} = L_{front}\dot{m}_{front}/(A_{frontal}\mu) \quad (1)$$

where $A_{frontal} = {L_{front}}^2$, and μ is the dynamic viscosity based on the average of hot and cold inlet temperatures.

Approximation-assisted optimization was employed to calculate the maximum heat capacity and the dimensions that meet all the constraints. The main advantage of such method is that it can reduce computational time significantly by using metamodel to predict the performance of the heat exchanger using the known information of the system. The optimization process was divided into 4 stages. The first stage is Design of Experiment (DOE) where initial sampling was performed using space filling method developed by Aute et al. [104]. The performance of the sampling points was then evaluated individually. The second stage is creating a metamodel using sampling points as input. Dace, a Kriging-based metamodel toolbox developed by Lophaven et al. [105], was used for this purpose. The third stage is the optimization process which utilized genetic algorithm method. The basic principle of genetic algorithm is to use concept like natural selection to eliminate inferior solutions and retain high performance solutions. The last stage is to validate the metamodel by calculating the performance of the heat exchanger using the modified hybrid method developed by Arie [80] and compare it to the one

predicted using metamodel. If the error between the prediction and actual values is small, the process concludes. Otherwise, the metamodel is recreated by using the validation points as additional sampling points. The process is repeated until sufficiently low metamodel error is obtained, and the process flow chart is shown in Figure 5-2.

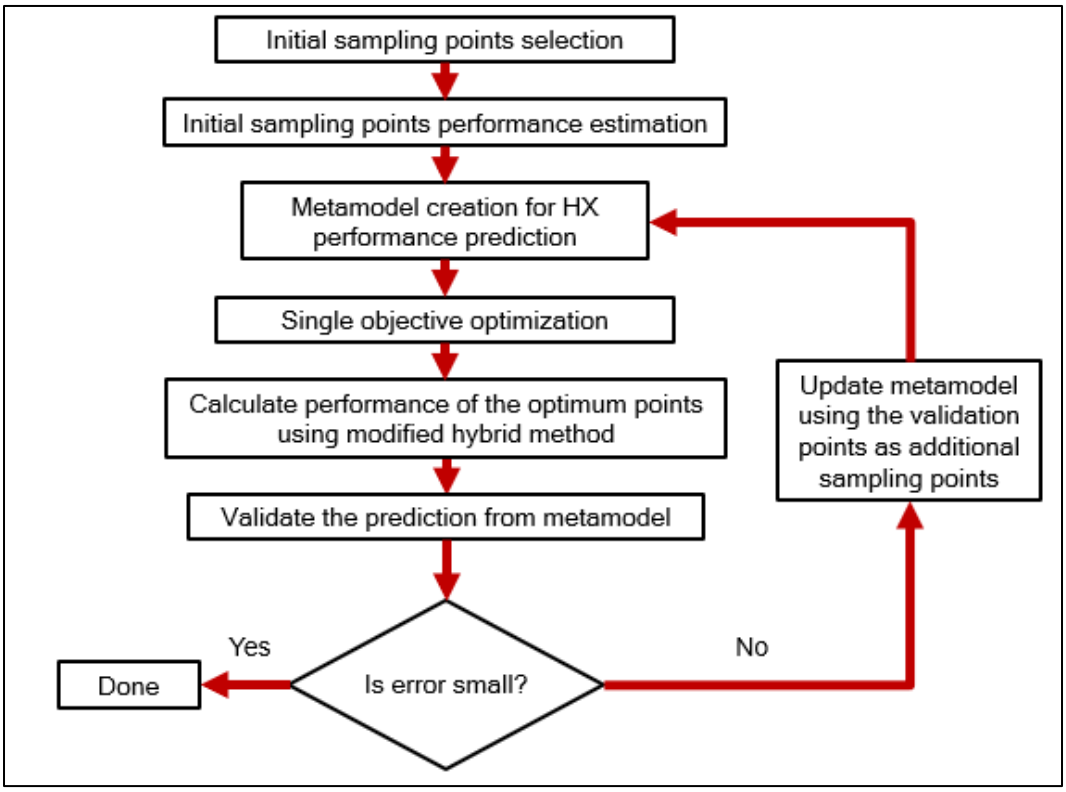

Figure 5-2: Single objective optimization flow chart

5.3. Modified Hybrid Method

The pressure drop and heat transfer performance of the manifold-microchannel heat exchanger were evaluated using modified hybrid method developed by Arie et al. [80]. This method involves using a single manifold-microchannel CFD simulation (the model is shown in Figure 5-3) to calculate the heat transfer coefficient and

pressure drop in the microchannel. The manifold pressure drop, on the other hand, was calculated by solving a 1-D differential equation of mass and momentum balance in the manifold channel. The detailed description of the method can be found in Ref. [106].

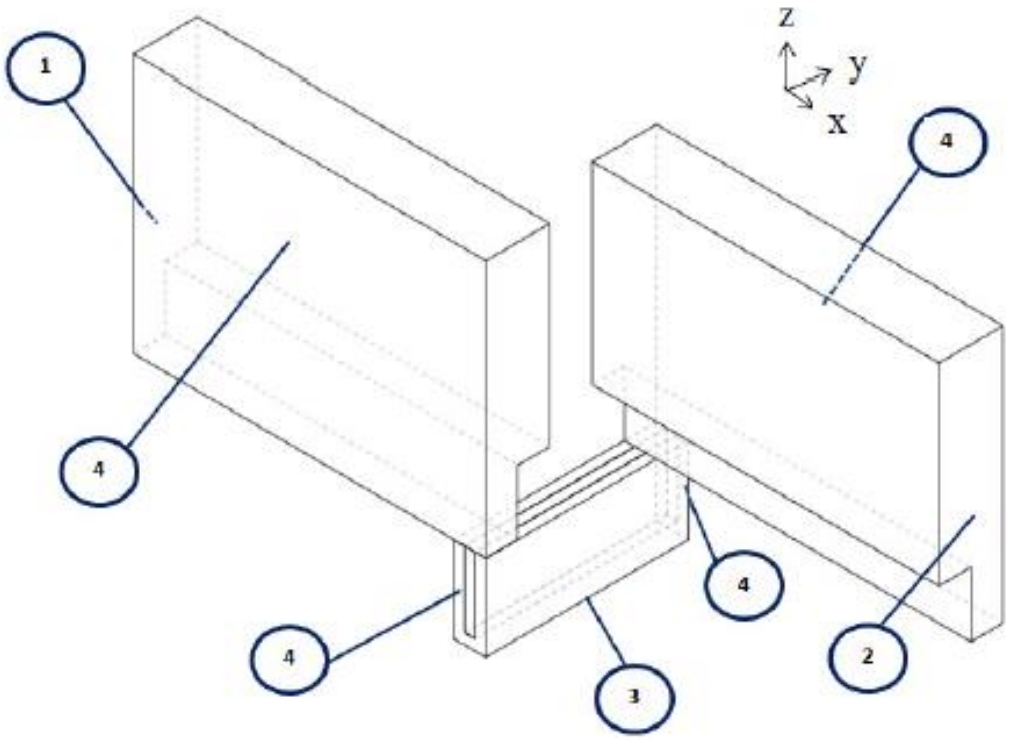

Figure 5-3: Computational domain and boundary conditions of a single manifold-microchannel by Arie [106]: (1) manifold channel inlet surface with mass flow inlet and constant temperature, (2) manifold channel outlet surface with constant pressure outlet, (3) microchannel base surface with constant surface temperature, (4) symmetry planes

The combined heat capacity (Q_{tot}) of the cross-flow heat exchanger was evaluated by first calculating the heat capacity in each stack($Q_{1\ stack}$). To do the calculation, first a single stack heat exchanger needs to be divided into N_{hot} sections on the hot flow direction and N_{cold} sections on the cold flow direction, each consisting of a single manifold-microchannel pass. An example is shown in Figure 5-4 for a single stack cross-flow manifold-microchannel heat exchanger with 2 passes on both the hot and cold sides (N_{hot} = 2 and N_{cold} = 2), which is subdivided into 4 components with a single manifold-microchannel pass of each.

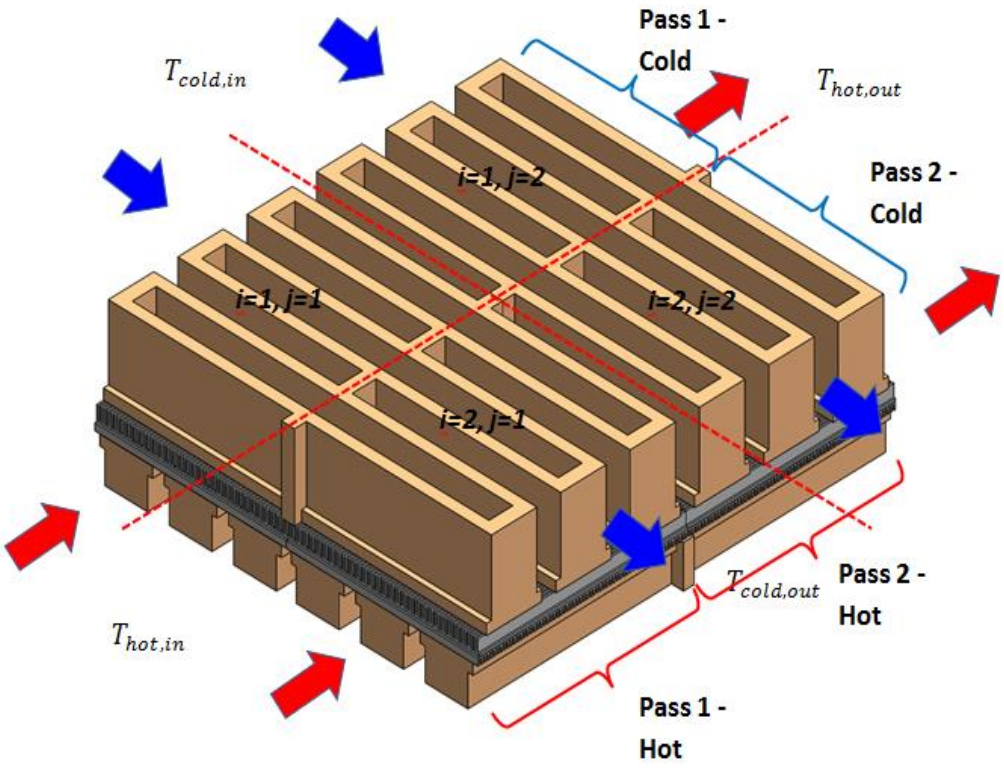

(a)

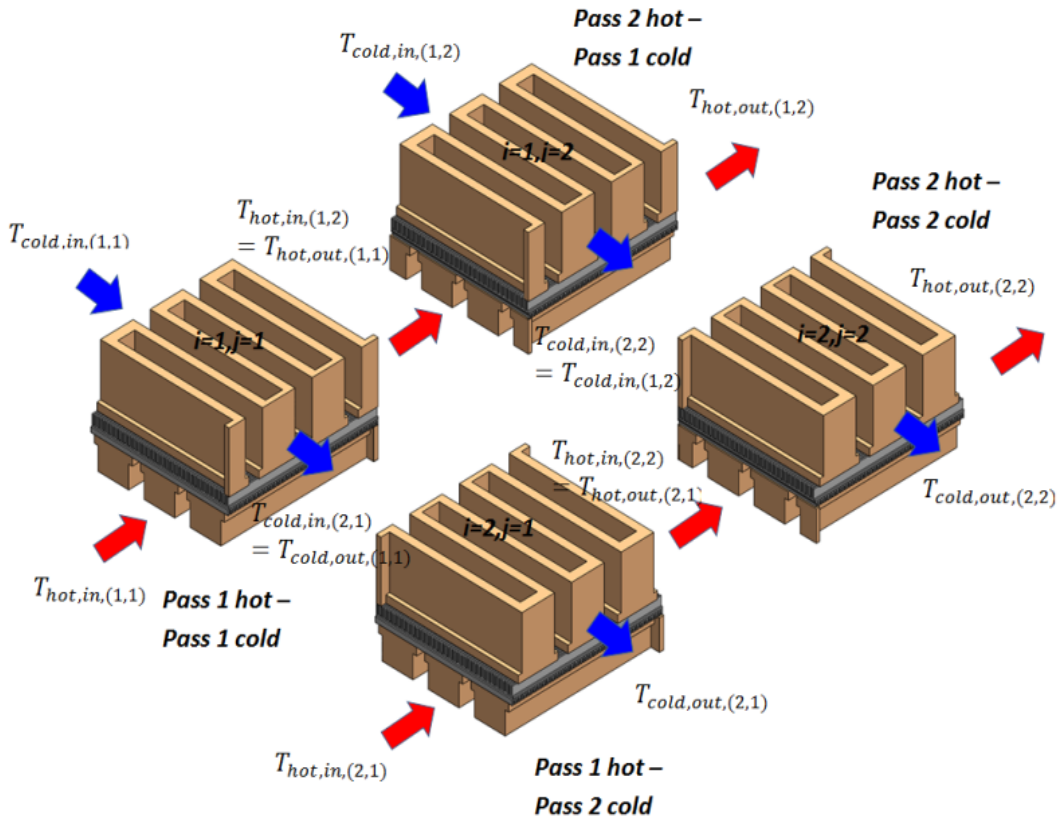

(b)

Figure 5-4: CAD model with 2 passes on both hot and cold sides by Arie [50]: combined model (a), subdivided model (b)

The heat duty for each component can then be calculated by performing an energy balance on that section. The detailed steps for Q_{tot} calculation are as follows:

1. Set the temperature boundary condition:

$T_{hot,in,(i,1)} = T_{hot,in}$ for i = 1 to N_{cold}

$T_{cold,in,(1,j)} = T_{cold,in}$ for j = 1 to N_{hot}

2. Set i=1 and j=1

3. Perform an energy balance on the section i, j by solving Eqs. (2) – (5) to solve for 4 unknown variables: heat capacity $Q_{i,j}$, cold-side exit temperature $T_{cold,out,(i,j)}$, hot-side exit temperature $T_{hot,out,(j,i)}$, and base temperature $T_{b,(i,j)}$, where h_{hot} and h_{cold} are the base conductance obtained from the CFD simulations. A_{base} is the total base area of the heat exchanger evaluated as: $A_{base} = L_{tot,hot} / \times L_{tot,cold}$.

$$Q_{i,j} = \frac{\dot{m}_{hot}}{N_{cold}} C_{p,hot}\left(T_{hot,in,(i,j)} - T_{hot,out,(i,j)}\right) \quad (2)$$

$$Q_{i,j} = \frac{\dot{m}_{cold}}{N_{hot}} C_{p,cold}\left(T_{cold,in,(i,j)} - T_{cold,out,(i,j)}\right) \quad (3)$$

$$Q_{i,j} = h_{hot} \frac{A_{base}}{N_{hot} N_{cold}} \left(T_{hot,in,(i,j)} - T_{b,(i,j)}\right) \quad (4)$$

$$Q_{i,j} = h_{cold} \frac{A_{base}}{N_{hot} N_{cold}} \left(T_{b,(i,j)} - T_{cold,in,(i,j)}\right) \quad (5)$$

4. Set $T_{hot,in,(i,j+1)} = T_{hot,out,(i,j)}$

and $T_{cold,in,(i+1,j)} = T_{cold,out,(i,j)}$

5. Update i value: $i = i + 1$

6. Repeat step 3-5 until $i = N\_cold$

7. Update *j* value: $j = j + 1$ and re-set i=1

8. Repeat step 3-7 until $j = N\_hot$

9. Calculate the total capacity of each stack as:

$$Q_{1\ stack} = \sum_{j=1}^{N_{hot}} \sum_{i=1}^{N_{cold}} Q_{i,j}$$

10. Calculate the total capacity of the heat exchanger as: $Q_{tot} = N_{stack} Q_{1\ stack}$ where N_{stack} is total stack number of the heat exchanger.

Two main assumptions were considered for the modified hybrid method. One is that the flow distribution among the microchannels is uniform, which means the mass flow rate in each microchannel is the same. The second assumption is for each computational domain (i, j) the base temperature remains constant. This is a fair assumption because for the case of single manifold-microchannel pass, the same inlet temperature in all microchannels is expected as the flow comes from the top of the microchannels through the manifold channel, and heat transfer only occurs in the microchannel section (no heat transfer occurs in the manifold channel). Because both the hot and cold flows have the same inlet temperatures, and uniform flow is fed across microchannels, each layer of the heat exchanger can be divided into hundreds of repeated unit cells which have the same hot-inlet and cold-inlet temperatures as shown in Figure 5-5. For each unit cell, due to the short flow length, a constant base temperature can be assumed.

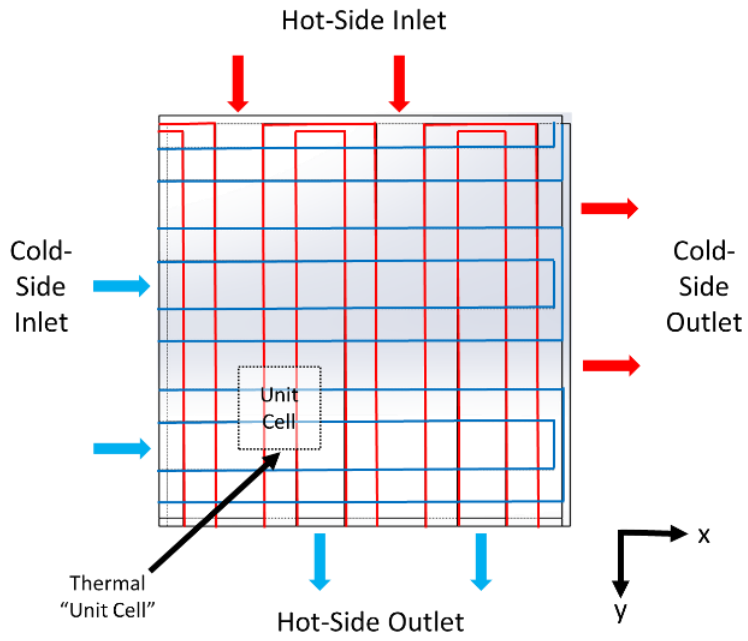

Figure 5-5: Unit-cell pattern from cross-flow manifold-microchannel heat exchanger [107]

5.4. Optimization Results & Design Selection

The optimization results of effectiveness (ε) and heat exchanger solid volume ratio (V_{solid}/V_{tot}) based on different manufacturing constraints are shown in Table 5-2. By comparing the results, the heat exchanger with microchannel surface and manifold both fabricated by 3-D metal printing (DMLS) provides the highest effectiveness and lowest heat exchanger solid volume ratio. 18% effectiveness improvement and 34% solid volume ratio reduction are possible compared to the heat exchanger manufactured by photo-chemical etching, and 8% effectiveness improvement and 17% solid volume ratio reduction are possible compared to a heat exchanger manufactured by laser micro-machining. Since the build material for all three heat exchangers is assumed to be the same as Inconel 718, and the overall

volume of all three design is the same as 0.002 m^3, a lower solid volume ratio also implies a lower mass of the heat exchanger design.

Table 5-2 Optimization results

Microchannel Surface Manufacturing Process	**Manifold Manufacturing Process**	**Optimized Results**
3-D Metal Printing (DMLS)	3-D Metal Printing (DMLS)	$\varepsilon = 0.569$ $V_{solid}/V_{tot} = 0.164$
Photo-chemical Etching	3-D Metal Printing (DMLS)	$\varepsilon = 0.481$ $V_{solid}/V_{tot} = 0.249$
Laser Micro-machining	3-D Metal Printing (DMLS)	$\varepsilon = 0.528$ $V_{solid}/V_{tot} = 0.197$

Besides higher effectiveness and lower heat exchanger solid volume ratio, there are also other benefits for heat exchanger manufactured by 3-D metal printing. First, 3-D printing the entire heat exchanger core as a single piece eliminates the necessity of subsequent steps. Secondly, 3-D metal printing technique is quite efficient thereby saves fabrication time and reduces material wastage as compared to other techniques. Thirdly, additive manufacturing is highly effective in fabricating extremely complicated and compact geometries, which can aid in developing minimum feature size that will potentially yield higher performance using a variety of materials as compared to any of the conventional fabricating techniques.

However, if 3-D metal printing (DMLS) is chosen as the fabrication approach based on the optimization results, the overhang issue must be considered. During the 3-D printing process, if the next layer is larger than the previous layer, an overhang issue will occur and cause build crash on the part as shown in Figure 5-6. DMLS has a

small allowance for unsupported overhangs (0.5mm), and structure with self-supporting angle (≥ 45°) can avoid overhangs as well.

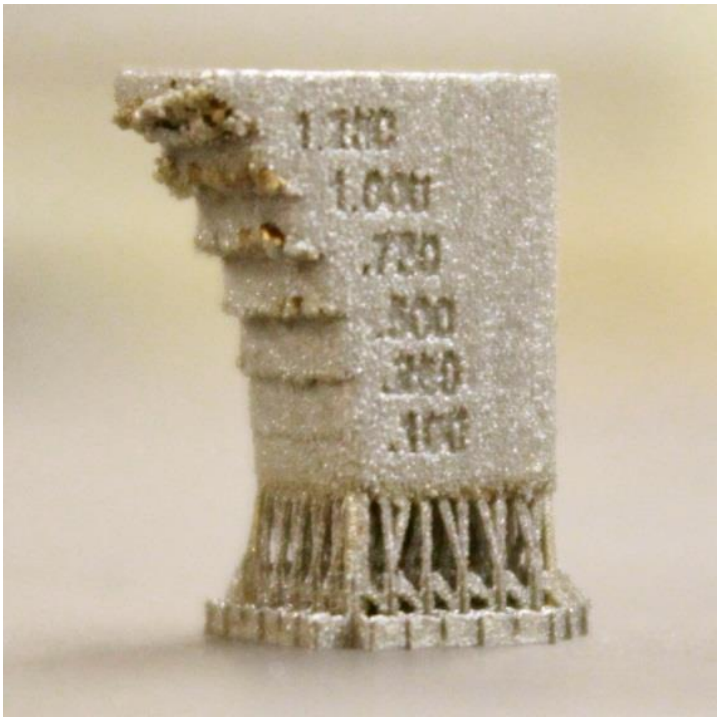

Figure 5-6: Build crash caused by overhangs [108]

For the cross-flow manifold-microchannel heat exchanger, depending on the printing orientation, the overhang issue will either occur at the manifold base and microchannel fins as shown in Figure 5-7 (a), or at the manifold walls and microchannel fins as shown in Figure 5-7 (b). Based on the communication with the manufacturer, it would be very challenging to print the part if the design was like the first case. And for the second case, if inclined fins and inclined manifold walls (which will be discussed in detail in the next chapter) can be implemented into the design, the printing of the part could still be realized.

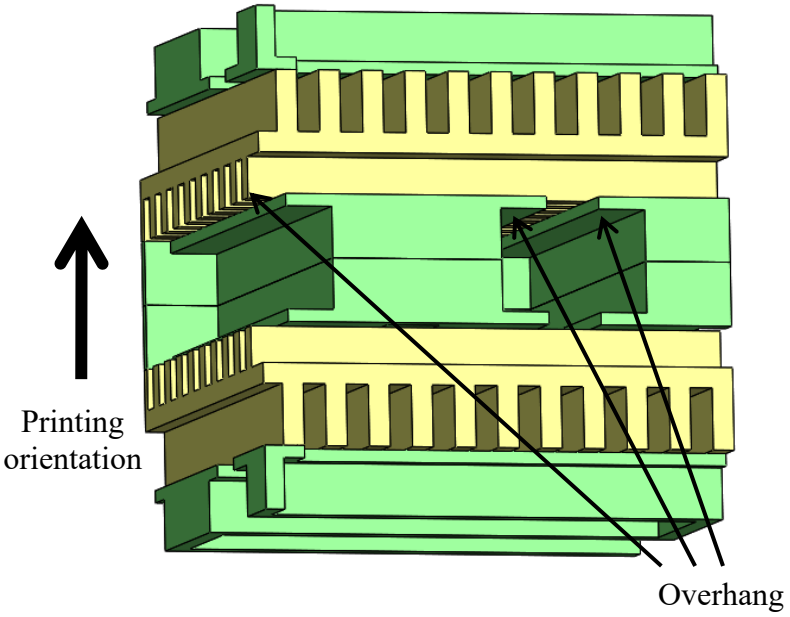

(a)

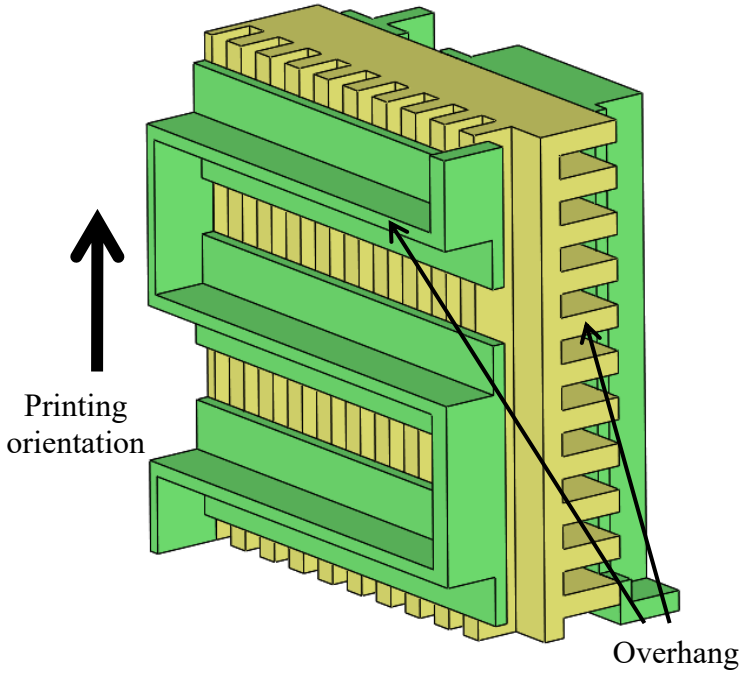

(b)

Figure 5-7: Overhang issue with cross-flow manifold-microchannel design: overhangs at the manifold base and microchannel fins (a); overhangs at the manifold walls and microchannel fins (b)

Since heat does not significantly transfer along the manifold channels, and the pressure drop across these channels will not be affected much if the manifold wall is modified from vertical wall to inclined wall, another optimization which added the effect of the inclined microchannel fins was performed. The updated optimized result from the 3-D metal printing process was again compared with the other two manufacturing approaches as shown in Table 5-3. The results showed that by implementing the inclined microchannel fins, the heat duty of the heat exchanger using DMLS process was reduced less than the one using laser micro-machining. However, the optimal design based on 3-D metal printing still has the lowest weight compared to the other two. For the design using photo-chemical etching, the reason that it has more layers might because the aspect ratio of microchannel width to height was fixed. For the design using laser micro-machining, since the microchannel height could not be more than 0.5 mm, more fins were needed to enlarge the heat transfer area. Therefore, it also has the largest base area (389 x 132 mm^2). As the weight of the manifold-microchannel heat exchanger design is mainly from the microchannel surfaces, more layers or larger base area will result in significant increase of the heat exchanger's total weight. Considering the higher heat transfer density (Q/m) which means less weight as an important aspect for the aerospace applications, and the elimination of assembly process, the heat exchanger design based on the 3-D metal printing (DMLS) approach was finally chosen.

Table 5-3 Summary of fabrication process and updated optimized results

Microchannel	Manifold	Assembly	Main Constraint	Optimized Results
3-D Metal Printing (DMLS)	3-D Metal Printing (DMLS)	**None**	Fin thickness ≥ 0.15 mm	Q = 23.8 kW m = 3.11 kg **Q/m = 7.65 kW/kg** 368 x 115 x 48 mm^3 (V_{tot} = 0.00205 m^3)
Photo-chemical Etching	3-D Metal Printing (DMLS)	**Diffusion Bonding**	Channel width = 1.1 x channel height	Q = 23.4 kW m = 4.29 kg **Q/m = 5.46 kW/kg** 341 x 113 x 52 mm^3 (V_{tot} = 0.00200 m^3)
Laser Micro-machining	3-D Metal Printing (DMLS)	**Diffusion Bonding**	Channel height ≤ 0.5 mm	Q = 25.6 kW m = 3.62 kg **Q/m = 7.08 kW/kg** 389 x 132 x 40 mm^3 (V_{tot} = 0.00205 m^3)

5.5. Scaled-down Model

In order to fabricate and test the optimized heat exchanger design, the heat exchanger had to be scaled down considering both the manufacturer's fabrication limitation and the testing capability in the lab. The dimensions of the subscale unit were determined by downscaling the full-scale 23.8 kW gas-to-gas cross-flow manifold-microchannel heat exchanger design which was obtained through the optimization process in the previous section. This downscaling process aims to reduce the overall volume of the full-scale heat exchanger to match the selected manufacturer's fabrication capability while keeping both hot and cold side microchannels' geometrical parameters (microchannel fin thickness, microchannel width, and microchannel height) unchanged.

To ensure the subscale unit's overall volume was less than the manufacturer's maximum building volume, a new optimization was performed. The effort involved additional geometrical constraints to ensure that hot side flow length (L) was less than 66 mm, cold side flow length (W) was less than 76 mm, and no-flow length (H) was less than 76 mm (see Figure 5-8). To keep similar performance characteristics, mass flow rate per microchannel on both hot/cold sides and COP on both hot/cold sides were kept the same as the full-scale design. The comparison between full-scale design and subscale unit is shown in Table 5-4. As can be seen, the subscale unit is about 1/10 of the full-scale unit in terms of heat transfer capacity.

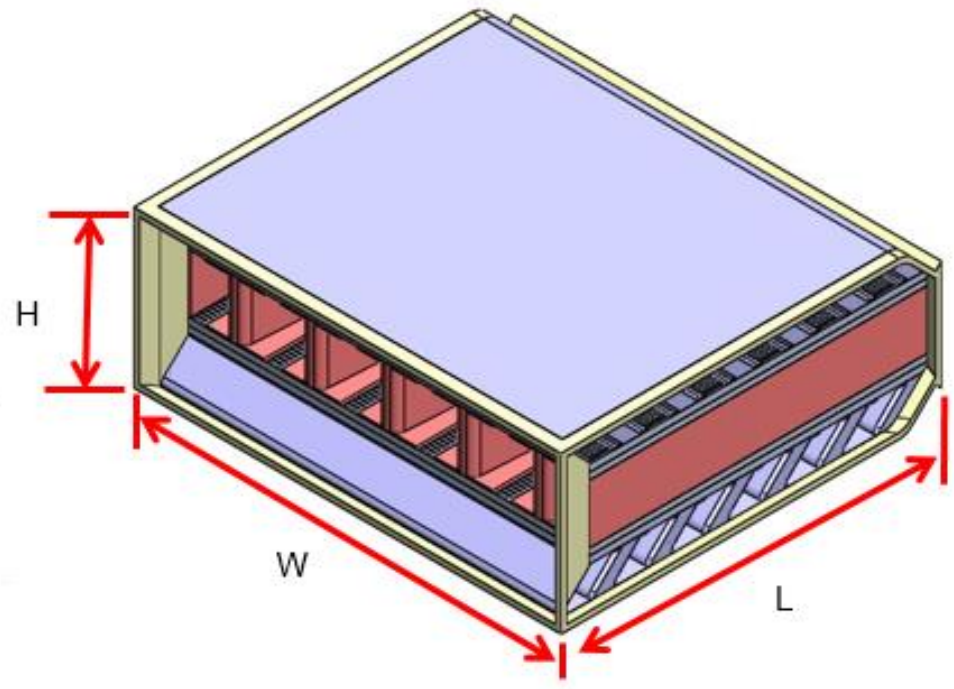

Figure 5-8: Subscale unit design (the yellow part was designed as connection interface for headers)

Table 5-4 Comparison between full-scale design and subscale unit

	Full-scale Design	**Subscale Unit**
Capacity (Q)	23.8 kW	2.0 kW
Hot flow length (L)	368 mm	59 mm
Cold flow length (W)	115 mm	70 mm
No-flow length (H)	48 mm	26 mm
Number of Layers	4	2

5.6. Summary

In summary, single-objective optimization for the gas-to-gas cross-flow manifold-microchannel heat exchanger with different fabrication approaches was described in this chapter. The optimization constraints and process were discussed in detail. The optimized results showed that even by implementing inclined microchannel fins to avoid the overhang issue, the heat exchanger design using 3-D metal printing (DMLS) process could still provide the highest heat transfer density (Q/m) and eliminate the assembly process to significantly reduce the fabrication lead time. Lastly, the optimized full-scale gas-to-gas cross-flow manifold-microchannel heat exchanger was scaled down for fabrication and experimental testing.

Chapter 6: Test Print Coupon & Subscale Unit Fabrication

6.1. Introduction

This chapter first discusses the test print coupons which were fabricated to evaluate the build quality using the selected DMLS process. The coupons' geometry was based on the scaled-down design proposed in chapter 5 with some design modifications according to the recommendations from the manufacturer (Proto Labs). After fabrication, the test print units were analyzed to evaluate the fabrication quality such as the printable minimum microchannel fin thickness and the minimum microchannel base thickness (which can also be called as separating sheet) that can prevent leakage from hot to cold side (as the design requirement has a higher system pressure on the hot side). Based on the test print units' evaluation, the subscale unit's geometry was updated to ensure the best fabrication quality, and the unit was successfully 3-D printed which matched very well to the final CAD design.

6.2. Test Print Coupon Design

Based on the communication with the manufacturer, DMLS only has a small allowance of 0.5 mm for unsupported structure [108]. Considering that the microchannel height on both sides of the design would be greater than 1 mm, either the hot side or cold side microchannel fins were suggested by the manufacturer to be printed at an inclined angle of 45 degrees to avoid overhangs during the fabrication process as shown in Figure 6-1. Based on the optimization study

discussed in the previous chapter, it was found that the heat exchanger's heat duty would be higher if inclined microchannel fins were implemented on the hot side.

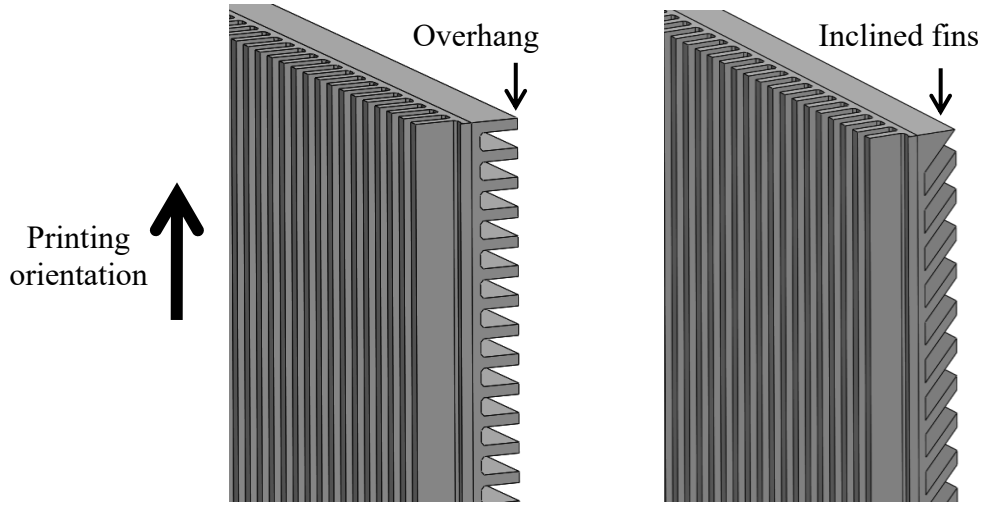

Figure 6-1: Cross-flow microchannel design layout: both side vertical fins (left); inclined fins on one side (right)

Since it was decided that hot side microchannel fins need to be inclined, to avoid overhang issue on the cold side, the manifold wall on cold side also had to be modified from vertical wall to inclined wall as shown in Figure 6-2 (a). With inclined microchannel fins on hot side and inclined manifold walls on cold side, a $20 \times 16 \times 9$ mm^3 test print coupon design based on the scaled-down design's geometry dimensions was created as shown in Figure 6-2 (b).

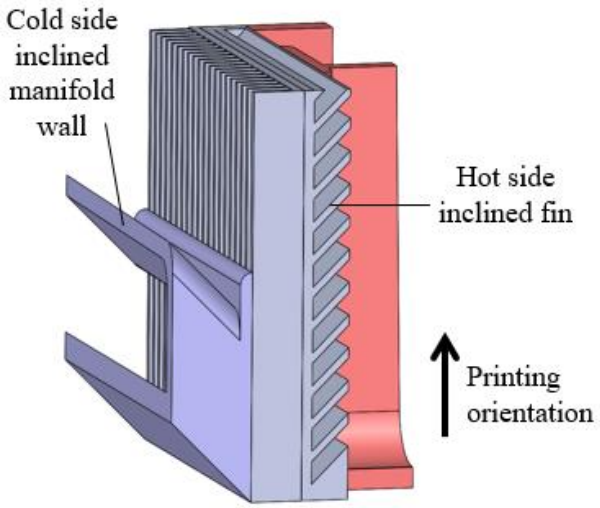

(a)

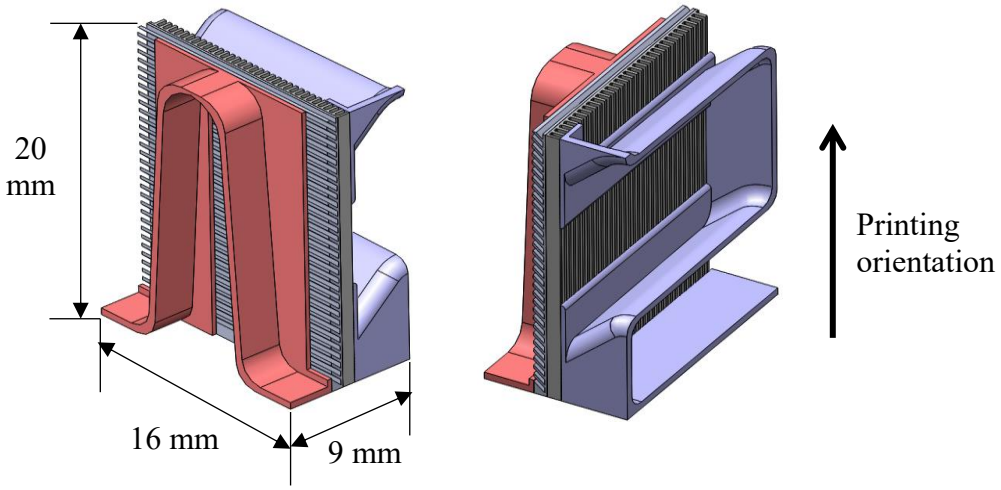

(b)

Figure 6-2: Zoom-in section view of cross-flow manifold-microchannel design with inclined microchannel fins on hot side and inclined manifold walls on cold-side (a); CAD design of the test print coupon (b)

Based on the initial scaled-down design obtained from the optimization discussed in the previous chapter, two test print coupon designs were prepared to check the manufacturer's minimum printable feature size such as the minimum microchannel fin thickness and manifold wall thickness. As shown in Table 6-1, coupon 1 has 0.200 mm vertical fins and 0.172 mm inclined fins as recommended by the manufacturer, and coupon 2 has the same dimensions as the initial scaled-down design except thinner inclined fins and manifold walls on the hot side. The same printing orientation were applied for both coupons as shown in Figure 6-2 (b).

Table 6-1 Test print coupon designs' minimum feature size dimensions

	Coupon 1		**Coupon 2**	
	Hot side	**Cold side**	**Hot side**	**Cold side**
Microchannel fin thickness (t_{fin})	0.172 mm	0.200 mm	0.106 mm	0.150 mm
Microchannel channel width (W_{chn})	0.280 mm	0.280 mm	0.346 mm	0.330 mm
Manifold wall thickness ($Wall_{mnd}$)	0.500 mm	0.500 mm	0.300 mm	0.500

6.3. Test Print Coupon Fabrication & Evaluation

Both test print coupons were successfully fabricated using DMLS by the manufacturer (Proto Labs) with Inconel 718 as shown in Figure 6-3. According to the weight measurement, both coupons showed very good agreement with the design value (< 2.3%) based on the material density provided by the manufacturer and the solid volume obtained from the CAD design.

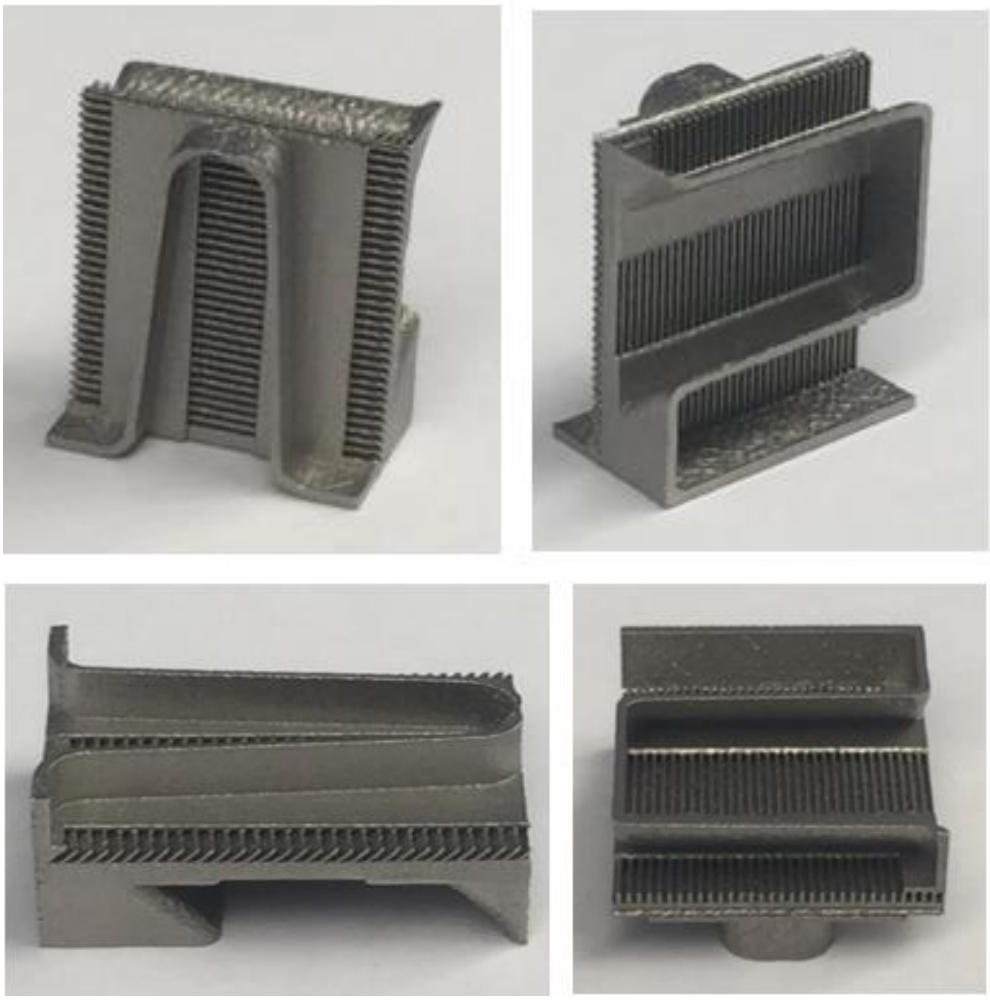

Figure 6-3: 3-D printed 20 x 16 x 9 mm^3 Inconel 718 test print coupon with inclined fins and inclined manifold walls

By measuring the small feature dimensions with a digital microscope, the measurements showed a good match as shown in Table 6-2. However, it was found that the fabricated minimum inclined fin thickness was 180 µm (± 12 µm) even if the CAD design value was less than it. And if the designed inclined fin thickness was less than 100 µm, this feature would not be printed according to the

manufacturer. For the vertical fins, it was concluded that the minimum printable thickness was 165 μm (± 7 μm).

Table 6-2 Test print coupons measurement

	Coupon 1			Coupon 2		
	Design (mm)	**Avg. Measure (mm)**	**diff %**	**Design (mm)**	**Avg. Measure (mm)**	**diff %**
Hot side length (L)	20.75	20.93	0.9%	20.50	20.66	0.8%
Cold side length (W)	15.80	15.76	-0.3%	15.80	15.79	-0.1%
No-flow length (H)	8.93	8.84	-1.0%	8.93	8.67	-2.9%
$\mathbf{H_{man\_cold}}$	3.82	3.79	-0.8%	3.82	3.8	-0.5%
$\mathbf{H_{man\_hot}}$	2.80	2.78	-0.8%	2.80	2.74	-2.1%
$\mathbf{Wall_{man\_cold}}$	0.50	0.51	2.0%	0.50	0.51	2.0%
$\mathbf{Wall_{man\_hot}}$	0.50	0.53	6.0%	0.30	0.32	6.7%
$\mathbf{t_{fin\_cold}}$	0.20	0.22	7.7%	0.15	0.17	10.6%
$\mathbf{t_{fin\_hot}}$	0.17	0.18	4.8%	0.11	0.19	75.8%

No defects (such as broken microchannels or warped manifold walls) were identified based on the evaluation of the fabricated coupons. As shown in Figure 6-4, both vertical fins and inclined fins showed good uniformity, and the manufacturer claimed that the surface roughness is 5 to 10 μm Ra. Except the different feature sizes of the coupons' design, both fabricated coupons also demonstrated a good repeatability with DMLS process.

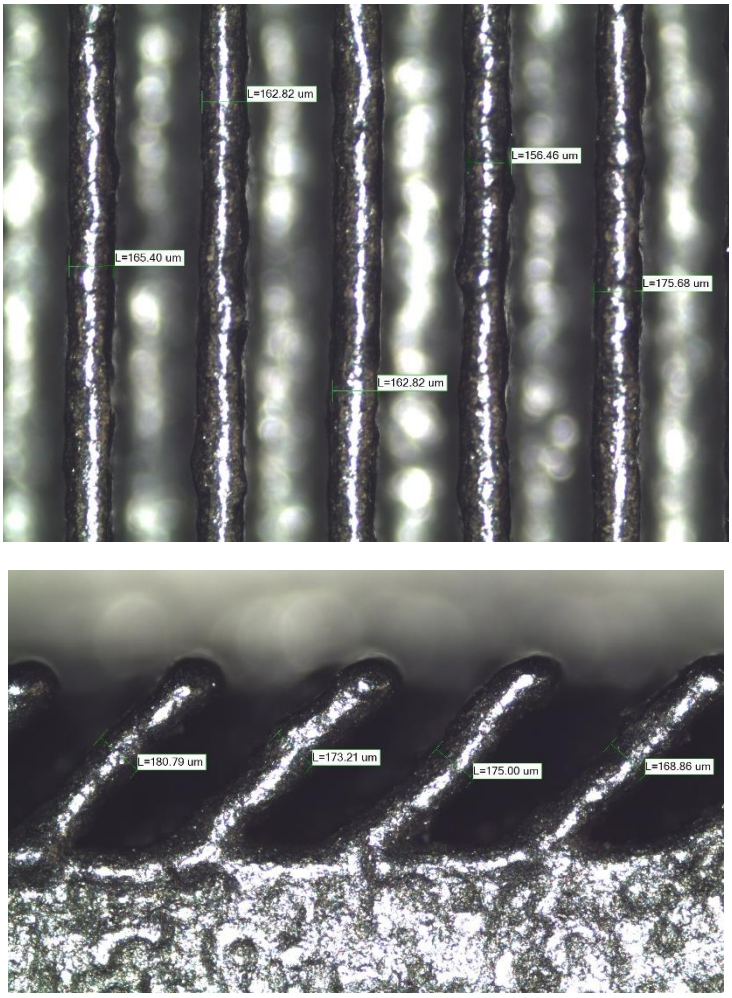

Figure 6-4: Measurements of the printed Inconel 718 coupon 2: straight fins (top); inclined fins (bottom)

6.4. Pressure Containment Coupon

Except the minimum feature size, the microchannel base thickness (which also can be call as separating sheet) was another important factor for the manifold-microchannel heat exchanger design. Considering the weight of the microchannel base is usually about 40-50% of the total manifold-microchannel heat exchanger's mass, a thinner microchannel base can significantly reduce the total weight of the

heat exchanger. However, it was noticed that the part fabricated by DMLS is not as solid as the one fabricated through conventional techniques. According to the DMLS manufacturer, the density of part is generally 99-99.5% of the raw material since it is a sintering process with micron size metal powder (which means there are some voids within the part). As a result, there might be a leaking issue if the microchannel base was too thin. In order to find the minimum microchannel base thickness which could prevent leakage under the requested system pressure (64.7 psia), two pressure containment test coupon designs were created with the same dimensions as test print coupon 2 as shown in Figure 6-5.

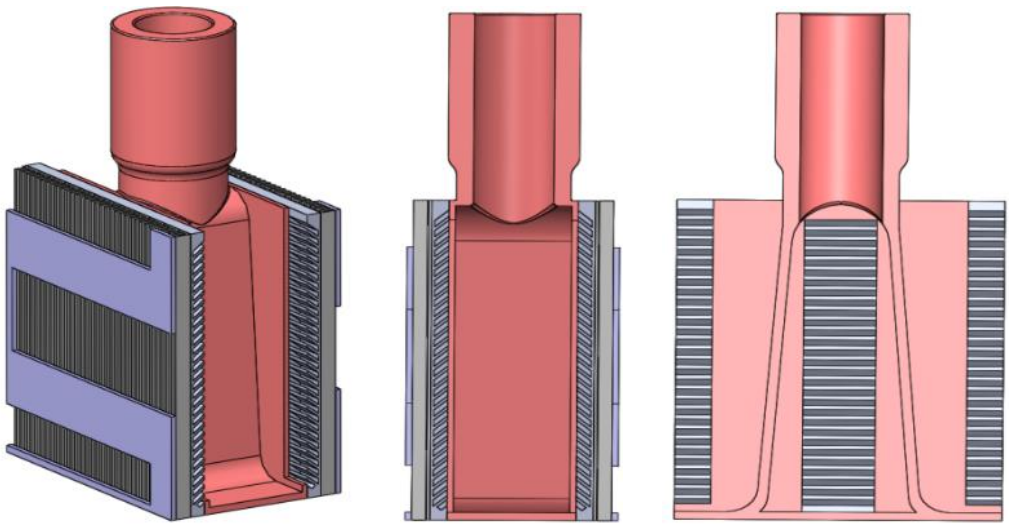

Figure 6-5: Pressure containment test coupon's CAD design (left); cross section view – right side (middle); cross section view – front side (right)

The difference between the pressure containment test coupon designs was that one has a microchannel base thickness of 0.5 mm, and the other's is 0.3 mm. The pressure containment test coupons were successfully fabricated using DMLS as shown in Figure 6-6. Considering the small tube opening with an inner diameter of

4 mm and the inclined microchannels with a channel width of 0.346 mm, there might still be some power left in the enclosure area on the hot side which is shown in red in Figure 6-5, which could accidentally seal the voids and reduce the leakage. To ensure there was no powder remaining in the inclined microchannels, the 3-D printed coupons were post-processed using an ultrasonic cleaner. After the cleaning, both coupons showed very good agreements to the design values (within 2%) based on the weight measurements.

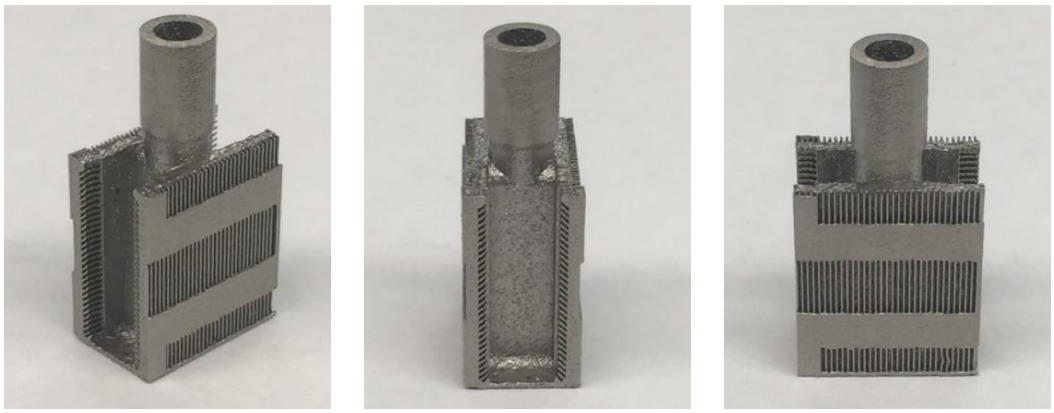

Figure 6-6: 3-D printed Inconel 718 pressure containment test coupon

To perform the pressure containment test, the coupon was directly connected to a Nitrogen gas tank, and the applied pressure was controlled by the pressure regulator. By putting the coupon under water, if there was any leakage, it would be visually identified, and the leaking point could be located based on where the bubbles showed up. As shown in Figure 6-7, one leaking point was identified on the coupon with base thickness of 0.3 mm, and no leakage was found on the one with 0.5 mm thick microchannel base. To check the maximum pressure that can be held by the 3-D printed coupon with base thickness of 0.5mm, another high-pressure test was performed. By connecting the coupon to a water-based pressure

pump, it was found that the coupon could withstand up to 3000 psig without any leakage.

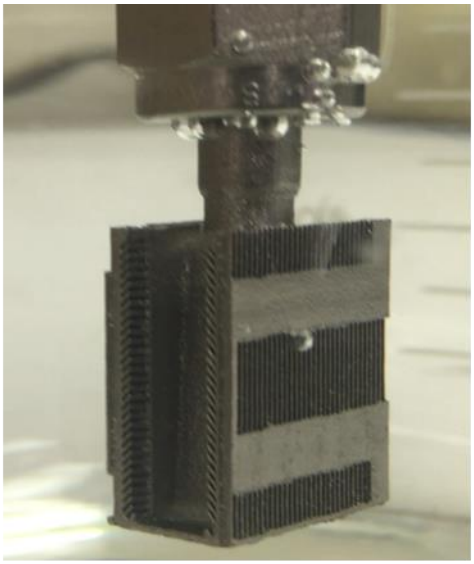

Figure 6-7: Pressure containment test coupon with base of 0.3 mm at 20 psig

6.5. Subscale Unit Design

Since the fabrication and evaluation of the test print coupons indicated the feasibility of the selected fabrication approach, a subscale unit design was created based on the DMLS process. The design has the same inclined microchannel fins on the hot side, and inclined manifold walls on the cold side. The printing orientation of the subscale unit is shown in Figure 6-8. A $10 \times 10 \times 5$ mm^3 small sectional sample design was also created for measuring internal structure dimensions considering it would be very difficult to directly measure the microchannel's dimensions inside the subscale unit.

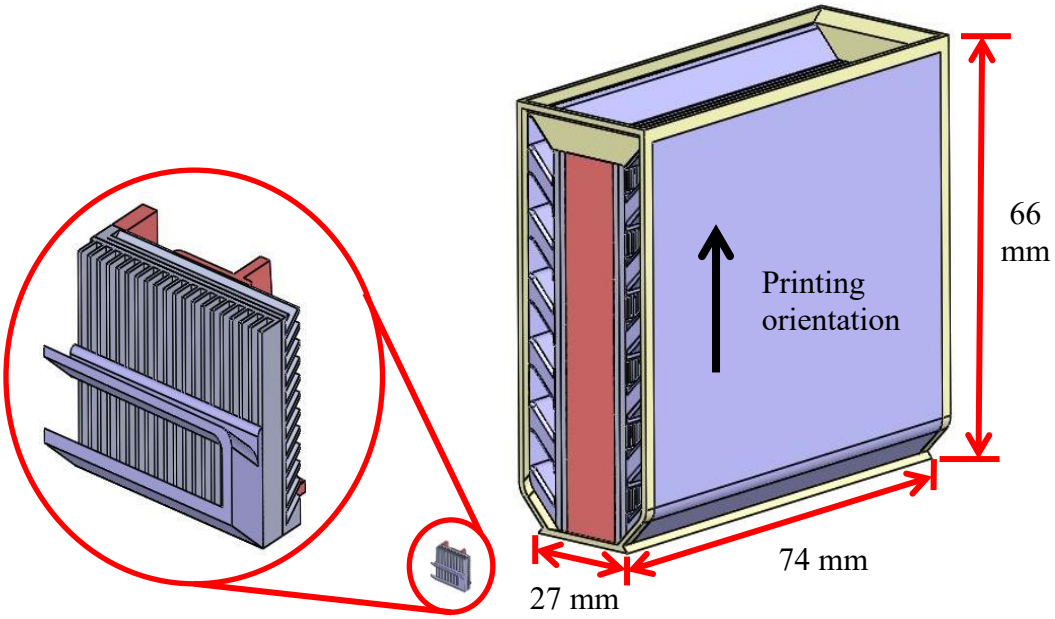

Figure 6-8: A small sectional sample for measuring internal structure dimensions (left); subscale unit printing orientation (right)

It was noticed by Arie [80] that straight manifold channel may induces a large maldistribution when the number of microchannels is high (n > 45), which makes the assumption of uniform flow distribution invalid for the numerical model discussed in the previous chapter. Therefore, the manifold channels on both hot and cold sides were designed as tapered channels for the subscale unit to better control the flow distribution. As shown in Figure 6-9, the flow area in the inlet manifold channels decreases longitudinally as more flow is fed into microchannels. The opposite process occurs for the outlet manifold channel where the flow area increases as more flow leaves the microchannels.

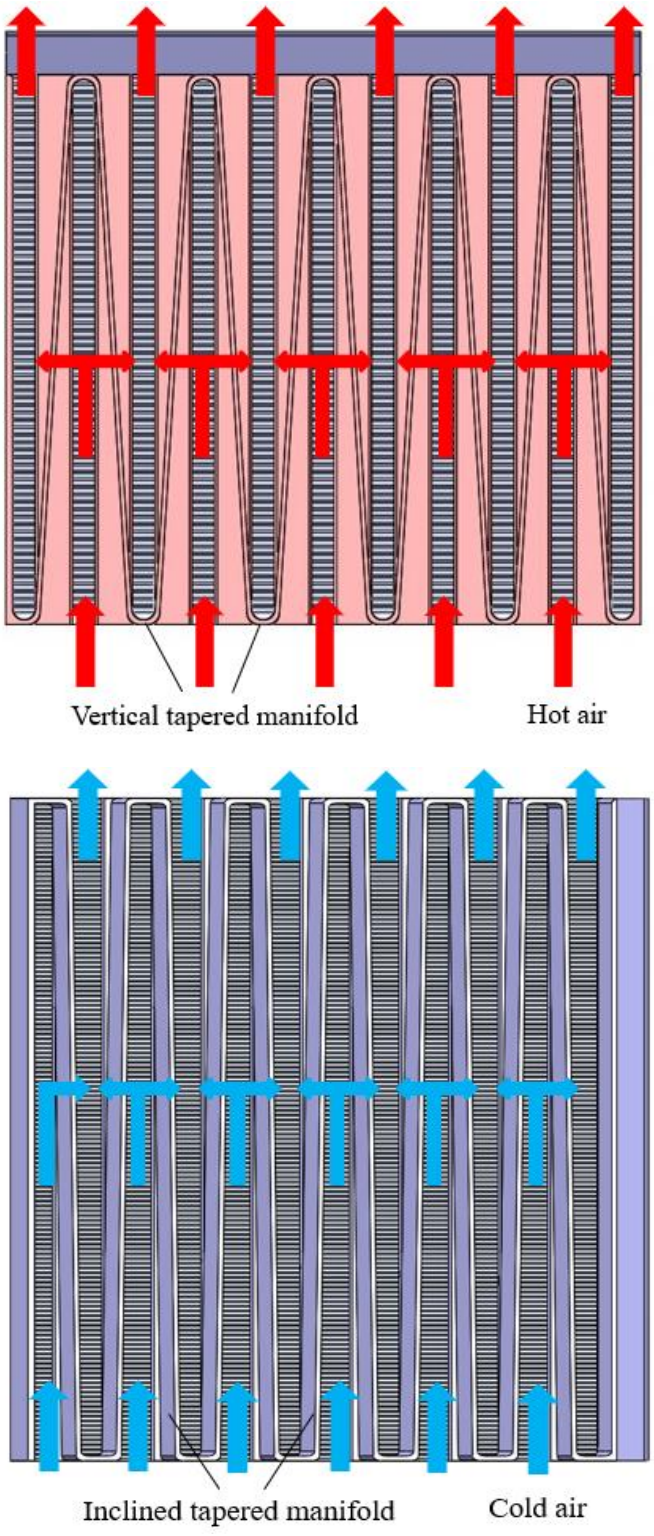

Figure 6-9: Hot-side tapered manifold channel with vertical manifold walls (top); cold-side tapered manifold channel with inclined manifold walls (bottom)

By implementing the fabricated minimum feature dimensions such as the minimum microchannel fin thickness of the test print coupons and minimum microchannel base thickness of the pressure containment test coupons, the subscale unit's design was updated from the initial scaled-down model, and the geometrical parameters of both the hot and cold sides are shown in Table 6-3 (see Figure 6-10 for the definitions of these parameters). Considering the subscale unit might need to be connected to upper-level manifolds (which can also be called as headers) through some conventional assembly processes, a connection interface was added into the design which is marked in yellow as shown in Figure 6-8.

Table 6-3 Geometrical parameters of the subscale unit

Hot Side	
t_{fin}	0.180 mm
W_{chn}	0.390 mm
H_{base}	0.250 mm
Number of microchannels	72
$Wall_{mnd}$	0.500 mm
Cold Side	
t_{fin}	0.165 mm
W_{chn}	0.340 mm
H_{base}	0.250 mm
Number of microchannels	138
$Wall_{mnd}$	0.500 mm
Overall Size	
L	66.0 mm
W	27.0 mm
H	74.0 mm
Mass	211 g

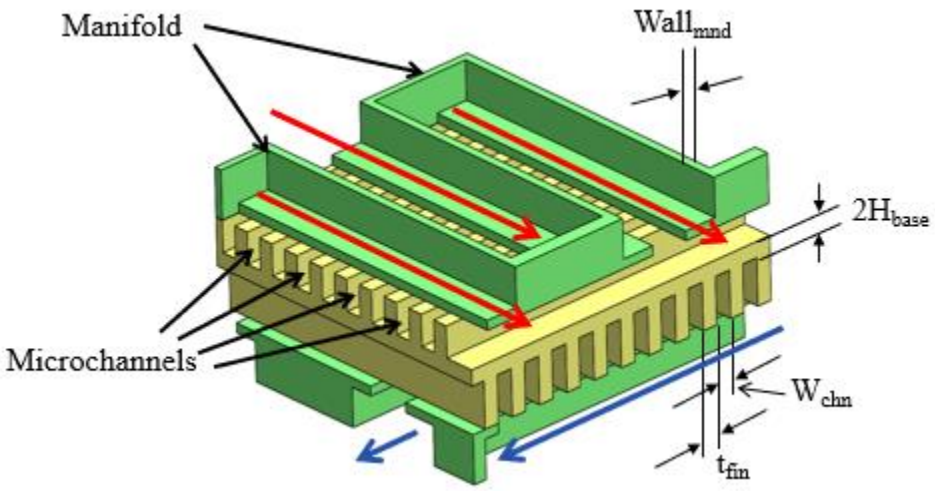

Figure 6-10: Cross-flow manifold-microchannel configuration

6.6. Subscale Unit Fabrication & Evaluation

Based on the subscale unit's final design, the heat exchanger core and the small sectional coupon were successfully fabricated simultaneously in the same build through DMLS as shown in Figure 6-11. The subscale unit was built within 36 hours which was much less than the quoted lead time of any other conventional manufacturing techniques. To ensure there was no powder remaining in the fabricated subscale unit, it was cleaned multiple times using an ultrasonic cleaner. After cleaning, the fabricated minimum feature dimensions were determined based on the measurements of the small sectional coupon, and the overall size of the subscale unit was measured as well. The variations between the fabricated and designed dimensions are shown in Table 6-4 and demonstrate fabrication fidelity within 14% of design values (except fin thickness on both sides, all other dimensions were within 5%). A pressure containment test was also performed on

the 3-D printed subscale unit. The result showed that the heat exchanger core could withstand a system pressure of 110 psig without any leakage from hot to cold sides.

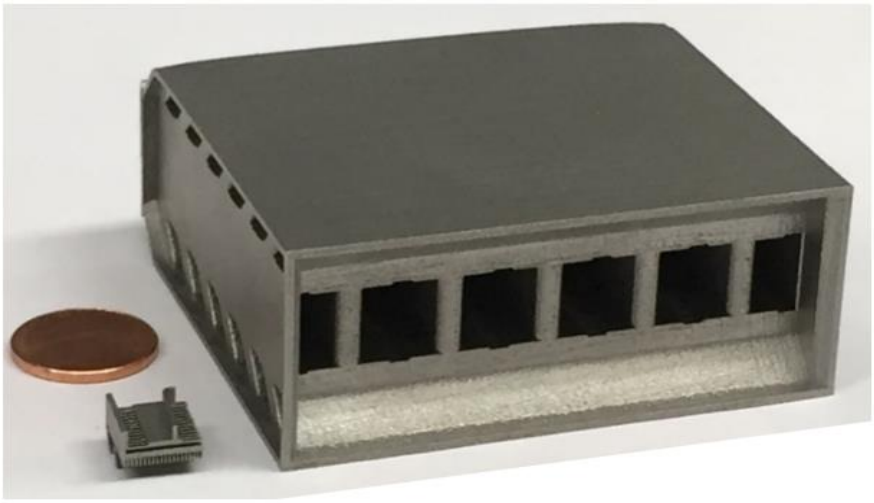

Figure 6-11: Additively manufactured Inconel 718 subscale unit and the small sectional coupon

Table 6-4 Percentage deviation of the fabricated dimensions and mass from the corresponding design values

Hot Side	
t_{fin}	12.20 %
W_{chn}	- 3.50 %
Cold Side	
t_{fin}	13.44 %
W_{chn}	- 4.15 %
Overall Size	
L	0.14 %
W	0.18 %
H	0.03 %
Mass	1.0 %

6.7. Summary

In summary, two test print coupons and two pressure containment test coupons were successfully fabricated through DMLS process using Inconel 718 as the material of choice. Inspection of the fabricated coupons showed that the minimum printable microchannel fin thickness was 165 µm for the vertical fins and 180 µm for the inclined fins. It was also concluded that the minimum microchannel base thickness needs to be 500 µm to prevent leakage from high-pressure (64.7 psia) to low-pressure (14.7 psia) side. By implementing the dimensions measured from the test print coupons in the initial scaled-down model, a subscale unit design was created, and it was successfully fabricated through DMLS using Inconel 718.

Chapter 7: Low-temperature Performance Characterization

7.1. Introduction

This chapter discusses the performance characterization of the 3-D printed subscale gas-to-gas cross-flow manifold-microchannel heat exchanger under low-temperature conditions. The single-manifold-multi-microchannels model is discussed since the subscale unit was modified to meet the new fabrication constraints, and the effect of the tapered manifold channel need to be considered. Experimental tests under low-temperature conditions were performed to evaluate the heat exchanger's performances. Lastly, the experimental results were compared with the numerical predictions.

7.2. Single-Manifold-Multi-Microchannels Model

The numerical model discussed in chapter 5 is based on straight manifold channel geometry and the assumption of uniform flow distribution into the microchannels along the manifold channel. The study from Arie [80] showed that if the flow maldistribution is less than 30%, the modified hybrid method with the single manifold-microchannel CFD model can still predict the performance accurately. The flow maldistribution, F, is defined as the ratio of the standard deviation of mass flow rate among all microchannels to the mean microchannel mass flow rate as

$$F = \frac{\sqrt{\frac{1}{n}\sum_{i=1}^{n}(\dot{m}_{chn,i} - \overline{\dot{m}_{chn}})^2}}{\overline{\dot{m}_{chn}}} \quad (6)$$

where n is the number of microchannels along the manifold channel, and a smaller F value means more uniform flow distribution.

However, since the subscale unit was modified based on the new fabrication constraints, the manifold channel was changed from straight channel to tapered channel as well. In order to confirm the flow maldistribution with the tapered manifold channel design is less than 30% so that the modified hybrid method can still be used to predict the performance, two single-manifold-multi-microchannels (SMMM) CFD models were created for both hot and cold sides based on the final CAD design and measured dimensions. The SMMM model was created with a mesh generation software Gambit 2.4.6, and solved numerically using the commercially available CFD software Fluent. Figure 7-1 shows an example of the SMMM model for the hot side. The goal of this model was to obtain the conductance h_{base} at the microchannel base area instead of the single manifold-microchannel model (as shown in Figure 5-3), and the pressure drop ΔP_{core} from the manifold inlet to manifold outlet (from surface A to surface B).

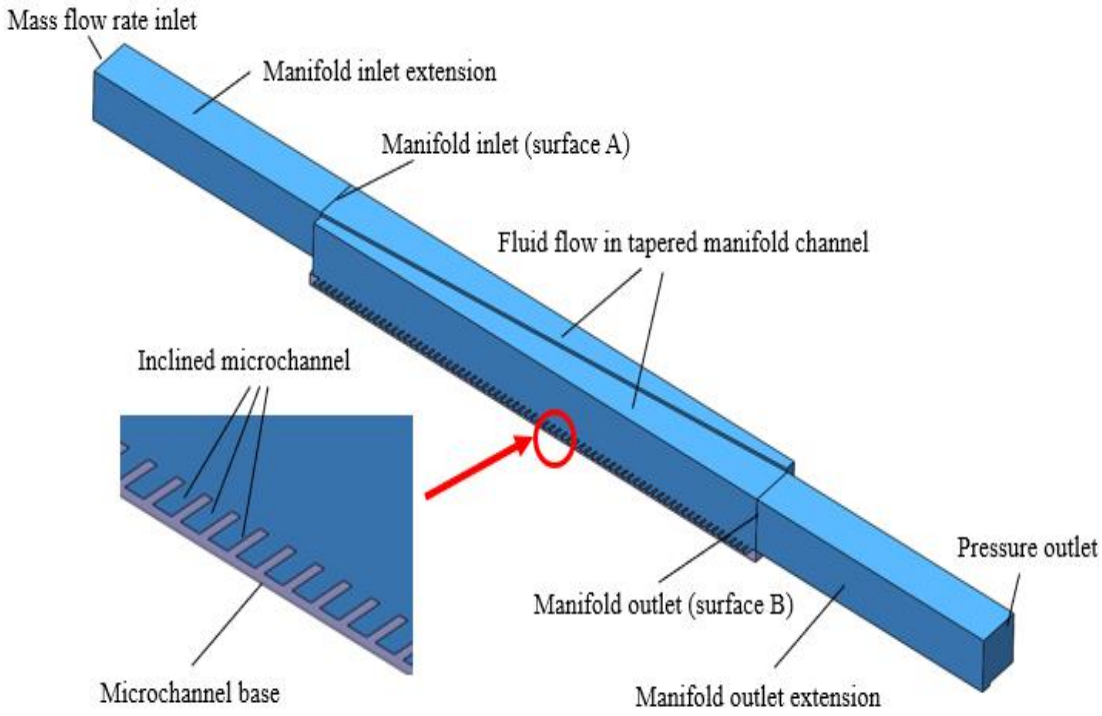

Figure 7-1: SMMM model for CFD simulation on the hot side

To achieve the goal, two assumptions were made for the SMMM model:

1. Mass flow rate in all manifold channels is equal.

2. Symmetric condition exists for both sides and top planes of the SMMM model.

The inlet surface of the manifold channel inlet extension was set to constant mass flow rate boundary condition and constant inlet temperature. The outlet surface of the manifold channel outlet extension was set as the pressure outlet boundary condition. The boundary condition of the microchannel base was set as a constant value calculated initially as the average of hot and cold inlet temperatures. This is based on the assumption that uniform flow was fed into each microchannel, and each layer of the subscale heat exchanger can be divided into hundreds of repeated

unit cells which have the same hot-inlet and cold-inlet temperatures. As a result of the short flow length of each unit cell, a constant base temperature can be assumed. To reduce the computational domain, only a half-section of the manifold was modeled, and symmetry boundary condition was applied on the top plane. A grid independency study was performed to find the minimum computational element number that provides less than 3% error while limiting the computational time. It was concluded that about 4,000,000 computational elements were sufficient for this purpose.

The heat duty (Q), outlet temperature on the hot and cold sides ($T_{hot,out}$ and $T_{cold,out}$), and temperature at the microchannel base (T_{base}) were calculated based on Equations (7) – (11) as there was only one pass on each side.

$$\mathrm{Q}_i = \dot{m}_{hot} C_{p,hot} \left(T_{hot,in} - T_{hot,out}\right) \tag{7}$$

$$\mathrm{Q}_i = \dot{m}_{cold} C_{p,cold} \left(-T_{cold,in} + T_{cold,out}\right) \tag{8}$$

$$\mathrm{Q}_i = h_{hot,base} A_{base} \left(T_{hot,in} - T_{base}\right) \tag{9}$$

$$\mathrm{Q}_i = h_{cold,base} A_{base} \left(-T_{cold,in} + T_{base}\right) \tag{10}$$

$$Q = N_{layer} \times \mathrm{Q}_i \tag{11}$$

where $T_{hot,in}$ and $T_{cold,in}$ are the inlet temperatures on the hot and cold sides, $\mathrm{Q_i}$ is the heat duty for each manifold-microchannel layer, $h_{hot,base}$ and $h_{cold,base}$ are the conductance obtained from the CFD simulations, $\mathrm{A_{base}}$ is the microchannel base

area, and N_{layer} is the number of manifold-microchannel layers. Five unknown variables ($T_{hot,out}$, $T_{cold,out}$, T_{base}, Q_i, and Q) can be solved.

Similar to the one shown in Figure 7-1, another SMMM model was created for the case with straight manifold channel on the hot side. Based on the CFD simulation results, it showed that the flow maldistribution is 11.9% with tapered manifold channel, and 24.7% with straight manifold channel as shown in Figure 7-2. This means a more uniform flow distribution could be achieved for the subscale unit with the tapered manifold channel design. As a result, using the SMMM model with tapered manifold channel, the modified hybrid method would provide a more accurate prediction.

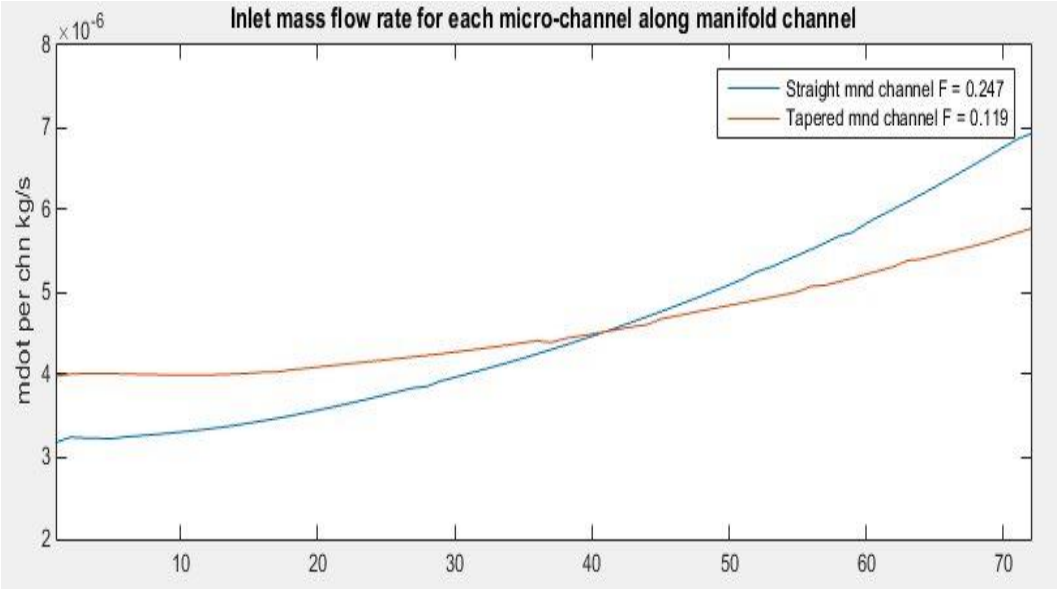

Figure 7-2: Flow distribution along the manifold channel on hot side (y-axis: mass flow rate in each microchannel; x-axis: microchannel location from the beginning to the end of manifold channel; “mnd" stands for manifold)

It was also noticed that the heat transfer performance predictions with both straight and tapered manifold channel SMMM models were close to each other. This is because the geometry was optimized by setting the upper limit constraint on flow maldistribution as 30%, and most of the heat transfer occurs along the microchannels, which means the heat transfer performance might not be affected by the straight or tapered manifold channel design (if the maldistribution of each design is less than 30%). However, the predicted pressure drop with tapered manifold channel was less than the one with straight manifold channel due to a smaller flow maldistribution as shown in Figure 7-3.

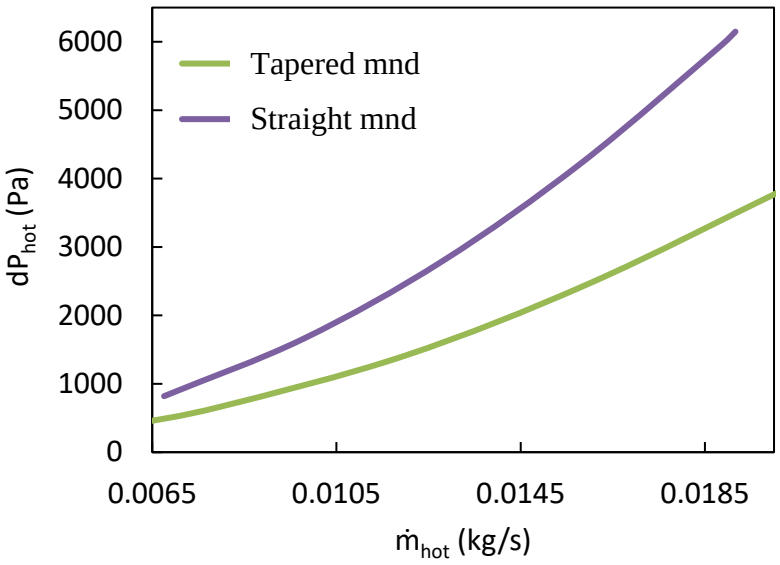

Figure 7-3: Hot side pressure drop prediction with SMMM model (cold side mass flow rate is constant at 0.006 kg/s)

7.3. Low-temperature Experimental Setup

To characterize the performance of the fabricated subscale unit, experiments under low temperature conditions (hot inlet temperature was ~ 43°C and cold inlet

temperature was ~ 13°C) were performed. A schematic diagram of the low-temperature experimental setup is shown in Figure 7-4. An air-to-water heat exchanger was added to adjust the inlet air temperature to the blower, and a variable speed controller was connected to the blower to control the total air flow rate by adjusting the power frequency supplied to the blower. The air flow then was distributed through the T-joint, and the flow rates on hot and cold side were adjusted by the gate valve on cold side. The hot side air was heated by the electric heater to reach the desired temperature. The cold side air temperature was adjusted through another air-to-water heat exchanger which has circulated low-temperature (~ -5 °C) working fluid (ethanol-based water solution) supplied by a chiller. The subscale unit was installed on the end of both hot and cold side as shown in Figure 7-4.

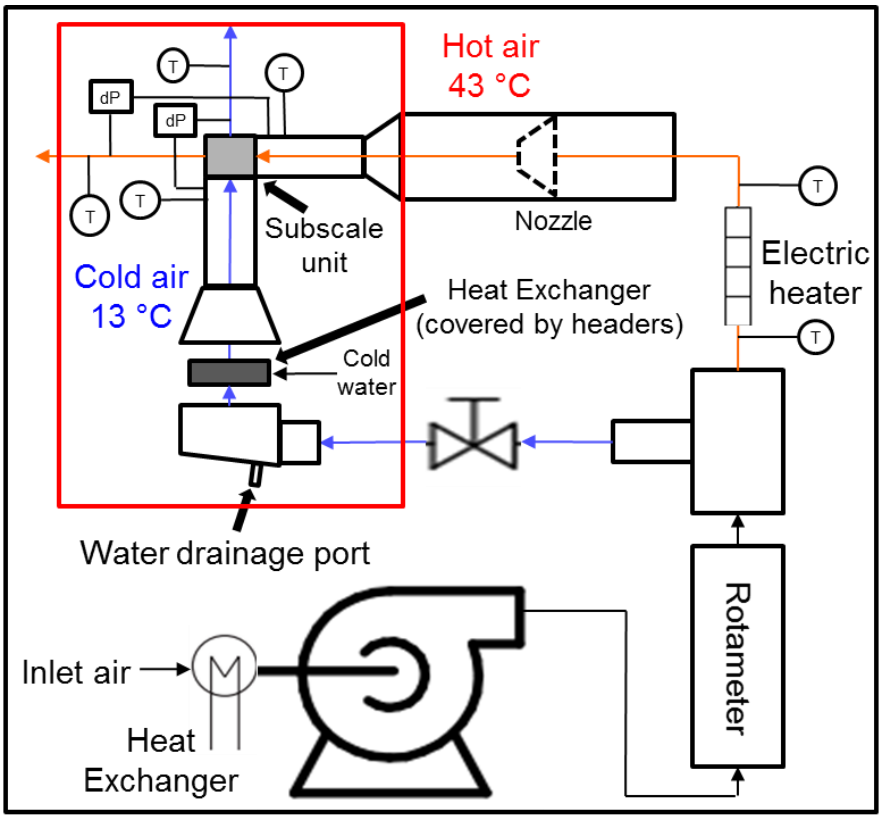

Figure 7-4: Schematic of low-temperature experimental setup

To connect the subscale unit to the low-temperature experiment setup, custom designed hot and cold side headers were created as shown in Figure 7-5 (a). The headers were then fabricated using PLA, which has a glass transition temperature about 60°C, through fused deposition modeling (FDM) process. For FDM, the parts are built by laying down the melted plastic filament through a heated nozzle to form the cross section of the object. Then the next layer of the cross section is formed by repeating the additive process. During the 3-D printing process of FDM, if the original design has an unsupported structure, a sacrificial structure will be added as supporting material to solve the overhang issue based on the printer's control program settings. As shown in Figure 7-5 (b), the 3-D printed headers had been post-processed to remove the unneeded supporting parts, and were connected to the subscale unit with a press-fit design.

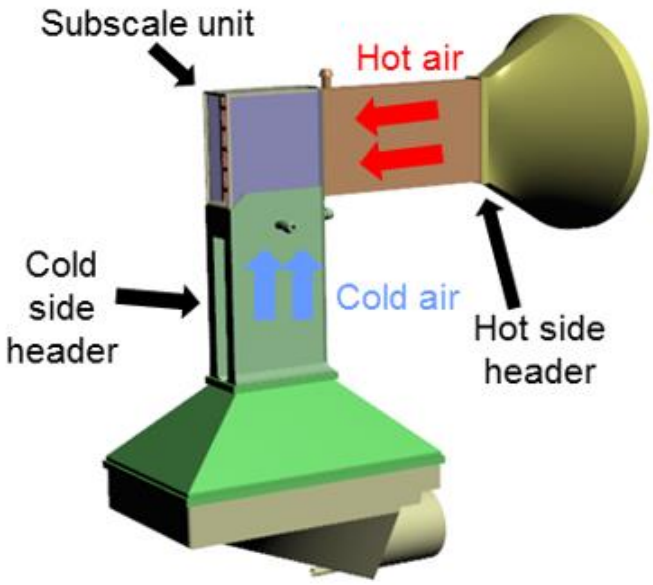

(a)

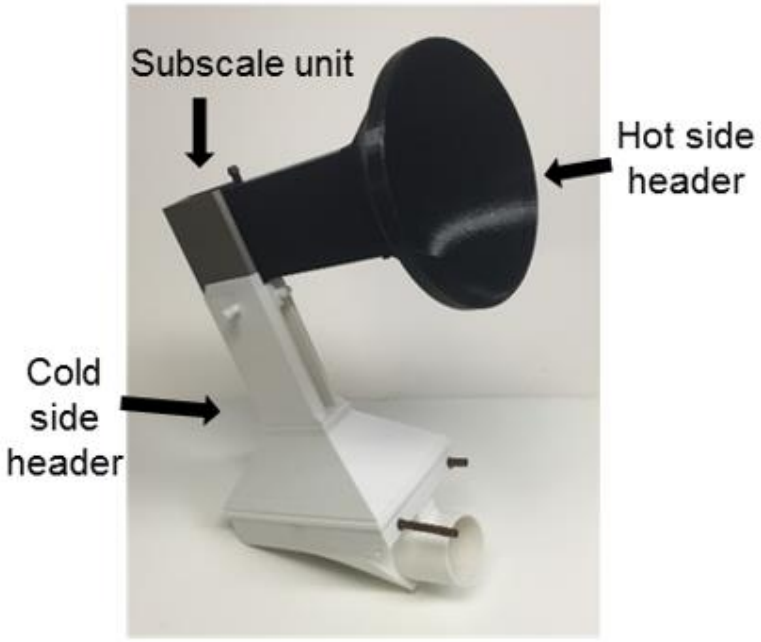

(b)

Figure 7-5: Headers' design for low-temperature experimental setup (a); 3-D printed plastic headers (b)

As shown in Figure 7-6, the headers were connected to the low-temperature experimental setup through either Aluminum tapes (hot side) or rubber couplings with steel duct clamps (cold side). To prevent any leakage from the connection area, silicon glue was applied to seal the gaps. On both hot and cold sides, four T-type thermocouples were inserted into the headers and placed as close as possible to the inlet surface of the subscale unit to measure the inlet temperatures. Another four thermocouples were placed at the subscale unit's outlet surface for outlet temperature measurements. Since the low-temperature tests were under atmospheric pressure conditions, only the inlet surfaces on both hot and cold sides were connected to the pressure transducers to measure the pressure drops across the subscale unit.

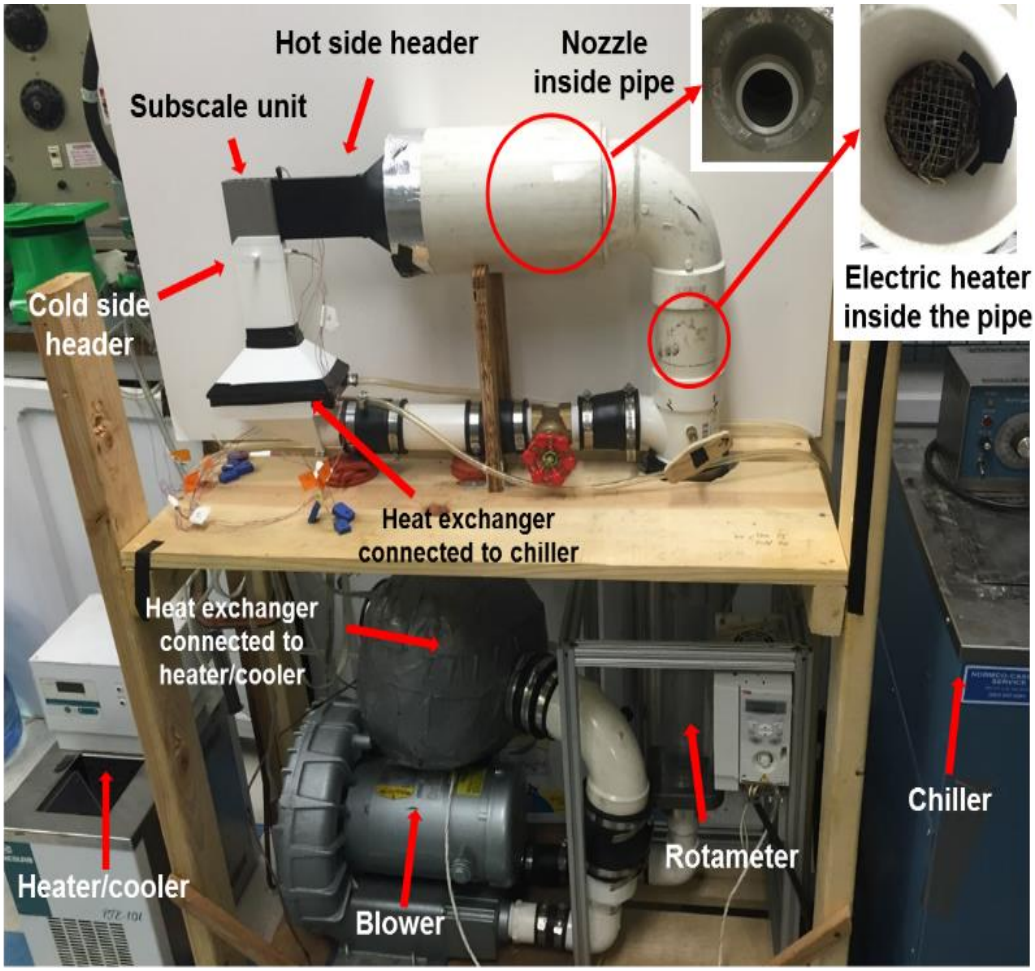

Figure 7-6: Low-temperature experimental setup

The total flow rate entering both hot and cold sides was measured through a rotameter, and a correction correlation was used to calculate the actual flow rate at the operation temperature as:

$$\dot{m}_{tot} = \rho \times \dot{V}^{std}_{measure} \sqrt{\frac{P_{exp} T_{cal} MW_{cal}}{P_{cal} T_{exp} MW_{exp}}} \tag{12}$$

where std means standard volumetric flow rate, exp stands for experiment, cal stands for manufacturing calibration, P is the air pressure, T is the flow temperature

(which is the same as the heater's inlet temperature for T_{exp}), and MW is the molecular weight.

To get a more accurate data, the flow rate on hot side was calculated as the average of the measurements from the nozzle and the electric heater. The flow rate through the nozzle was calculated based on the measured pressure drop across the nozzle as:

$$\dot{m}_{nozzle} = \rho \times Cd \times Ao \times \sqrt{\frac{2\Delta P}{\rho[1-(\frac{Do}{Di})^4]}} \quad (13)$$

where ρ is the air density based on the heater's outlet temperature measurement, Cd is the discharge coefficient from the nozzle's calibration provided by the manufacturer, Ao is the cross-section area of the nozzle throat, Do is the diameter of the nozzle throat, and Di is the diameter of the nozzle inlet cross-section area.

For the electric heater, the flow rate was calculated based on:

$$Qe = Cp \times \dot{m}_{heater} \times (T_{heater,\text{out}} - T_{heater,in}) \quad (14)$$

where Qe is the measured electricity energy input to the heater, and Cp is the specific heat based on the average of the heater's inlet and outlet temperatures. The flow rate on cold side then was the subtraction of hot side flow rate from the total flow rate.

7.4. Low-temperature Experiment Method

The low-temperature experiments were performed under the conditions shown in Table 7-1. Due to the glass transition temperature of header's material, the hot side

air temperature was set at 43°C to avoid any deformation of the header during the tests. In order to achieve a proper temperature difference between hot and cold inlet temperatures, the cold side air temperature was set at 13°C. The experiments were performed twice, the first test is to change hot side flow rate while keeping cold side flow rate constant at 0.006 kg/s. Then, the second one is to change cold side flow rate while keeping hot side flow rate constant at 0.019 kg/s. During the tests, hot side inlet temperature ($T_{hot,in}$), hot side outlet temperature ($T_{hot,out}$), hot side pressure drop (Δp_{hot}), cold side inlet temperature ($T_{cold,in}$), cold side outlet temperature ($T_{cold,out}$), and cold side pressure drop (Δp_{cold}) were measured and recorded.

Table 7-1 Low-temperature experiment conditions

Temperature Condition	
$T_{hot,in}$	43 °C
$T_{cold.in}$	13 °C
Varying Hot Side Flow Rate	
$\dot{V}_{hot}$	0.007-0.018 m^3/s
$\dot{V}_{cold}$	0.005 m^3/s
Varying Cold Side Flow Rate	
$\dot{V}_{hot}$	0.017 m^3/s
$\dot{V}_{cold}$	0.001-0.007 m^3/s

Based on the measurements, the heat transfer rate of the subscale unit was evaluated as:

$$\dot{m}_{hot} = (\dot{m}_{nozzle} + \dot{m}_{heater})/2 \tag{15}$$

$$\dot{m}_{cold} = \dot{m}_{tot} - \dot{m}_{hot} \tag{16}$$

$$Q_{hot} = Cp_{hot} \times \dot{m}_{hot} \times (T_{hot,in} - T_{hot,out}) \tag{17}$$

$$Q_{cold} = Cp_{cold} \times \dot{m}_{cold} \times (-T_{cold,in} + T_{cold,out}) \tag{18}$$

$$Q = (Q_{hot} + Q_{cold})/2 \tag{19}$$

where Cp and ρ are air properties for hot and cold side based on the average temperature between inlet and outlet measurements. A heat balance within 10% between hot and cold sides was recorded during the low-temperature tests.

The overall heat transfer coefficient (U) was evaluated using the log mean temperature difference (LMTD) method for both unmixed cross-flow arrangements as given in Eqs. (20) - (23) as a function of inlet and outlet temperatures on both the hot and cold sides.

$$dT_A = T_{hot,in} - T_{cold,out} \tag{20}$$

$$dT_B = T_{hot,out} - T_{cold,in} \tag{21}$$

$$LMTD = CF \frac{dT_A - dT_B}{\ln(dT_A / dT_B)} \tag{22}$$

$$U = \frac{Q}{N_{layer} A_{base} LMTD} \tag{23}$$

where CF is the configuration correction factor of both unmixed cross-flow, N_{layer} is the number of manifold-microchannel layers, and A_{base} is the microchannel base area (A_{base} = 0.059 m × 0.070 m).

Uncertainty propagation analysis was performed to calculate the uncertainty in the subscale heat exchanger performance parameters (Q, U) due to inaccuracy of the measurements. A list of the measurement equipment is shown in Table 7-2 with the corresponding accuracies. The uncertainty of the calculated quantity Y (U_Y), which is a function of $X_1, X_2, \ldots, X_N$ with uncertainty of $U_{X1}, U_{X2}, \ldots, U_{XN}$, can be calculated using the method explained in NIST Technical Note 1297 [109] as:

$$U_Y = \sqrt{\sum_i (\frac{\partial Y}{\partial X_i})^2 U_{X_i}^2} \tag{24}$$

The uncertainties of the subscale heat exchanger performance parameters (Q, U, ΔP) were included as error bars in the results presented in the next section.

Table 7-2 List of low-temperature measurement equipment and its accuracy

Equipment function	**Equipment name**	**Accuracy**
Total flow rate	Fischer Porter F Rotameter	± 2%
Pressure drop across nozzle	Setra pressure transducer	± 0.14% FS of 1.2 kPa
Temperature	T type thermocouple	± 1.0°C or 0.75% of measurement
Hot-side pressure drop	Setra pressure transducer	± 0.14% FS of 7.5 kPa
Cold-side pressure drop	Setra pressure transducer	± 0.14% FS of 2.5 kPa

7.5. Low-temperature Experiment Results

The subscale unit's performances are shown in Figure 7-7 for the case of varying hot side flow rate while keeping the cold side flow rate constant at 0.006 kg/s. The heat duty, pressure drop on the hot side, and overall heat transfer coefficient are plotted as a function of hot side flow rate. The capacity (Q) is based on a temperature difference of 30°C between hot and cold inlet air. Figure 7-7 (a) shows a maximum capacity of 90 W for the subscale unit under low-temperature conditions. During the low-temperature tests, the hot-side pressure drop (ΔP_{hot}) reached 4000 Pa at maximum hot-side mass flow rate of about 0.019 kg/s as shown in Figure 7-7 (b). The overall heat transfer coefficient (U) of the heat exchanger was in the range of 900 – 1200 W/m^{2}K as shown in Figure 7-7 (c).

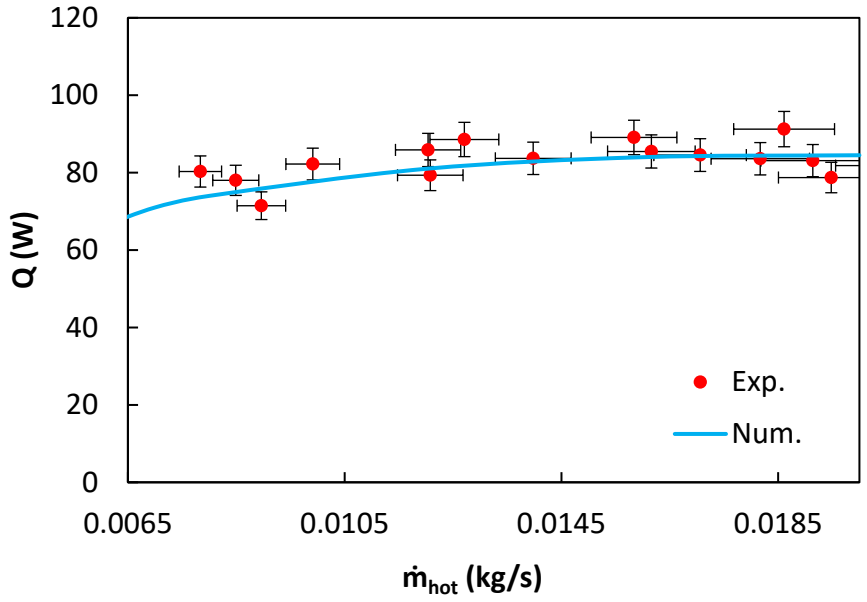

(a)

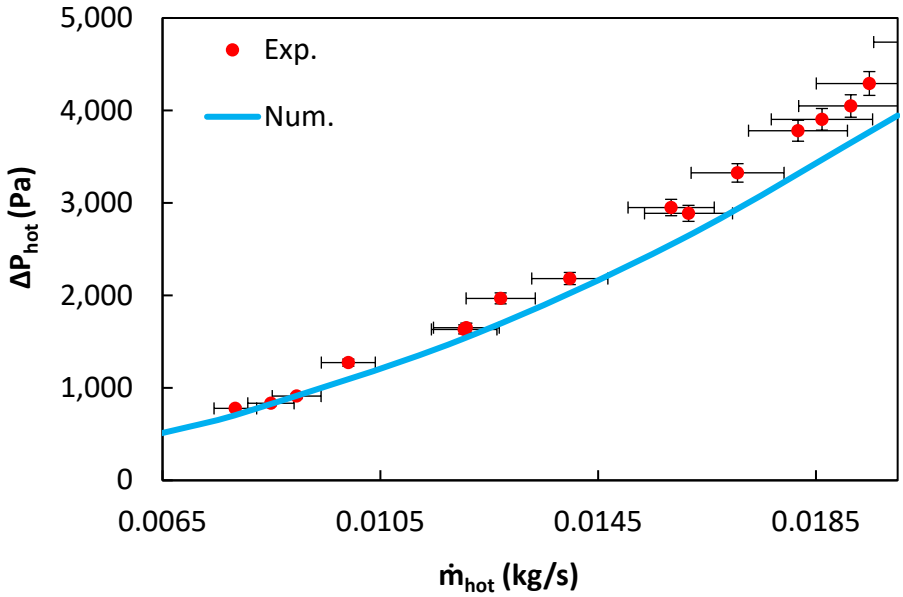

(b)

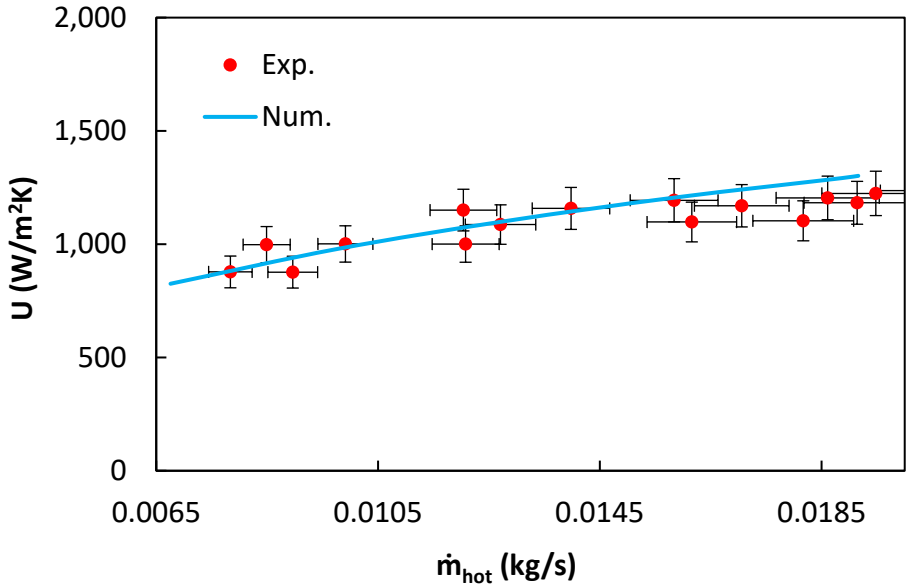

(c)

Figure 7-7: Experimental and numerical results for constant cold-side mass flow rate at 0.006 kg/s and 30°C temperature difference between hot and cold inlet air: heat duty (Q) vs. hot-side mass flow rate ($\dot{m}_{hot}$) (a); hot-side pressure drop (ΔP_{hot}) vs. hot-side mass flow rate ($\dot{m}_{hot}$) (b); overall heat transfer coefficient (U) vs. hot-side mass flow rate ($\dot{m}_{hot}$) (c)

The results showed a decent agreement between the numerical predictions and experimental results. Analysing the overall trend, heat duty, hot-side pressure drop, and overall heat transfer coefficient all increase as hot-side mass flow rate increases. This trend is as expected since the flow in microchannels is in the developing region, increasing flow rate leads in an increase of heat transfer performance as well as pressure drop.

Figure 7-8 is showing the case of varying cold side flow rate while keeping the hot side flow rate constant at 0.019 kg/s. The heat duty, pressure drop on the cold side, and overall heat transfer coefficient are plotted as a function of cold side flow rate. Figure 7-8 (a) shows a maximum capacity of 100 W for the subscale unit with a 30°C temperature difference between both sides' inlet air. A maximum cold-side pressure drop (ΔP_{cold}) of 1360 Pa was recorded when cold-side mass flow rate reached 0.008 kg/s as shown in Figure 7-8 (b). The overall heat transfer coefficient (U) of the heat exchanger was in the range of 800 – 1500 W/m^{2}K as shown in Figure 7-8 (c).

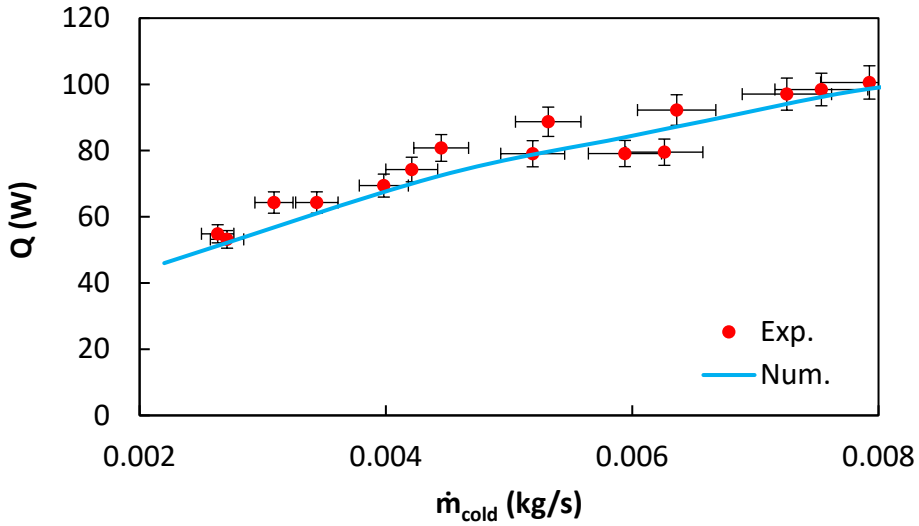

(a)

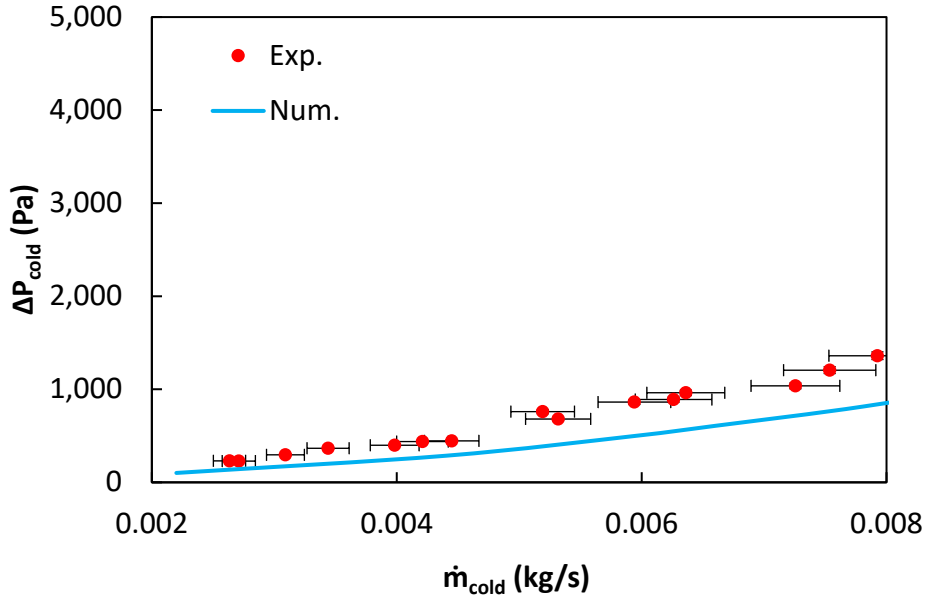

(b)

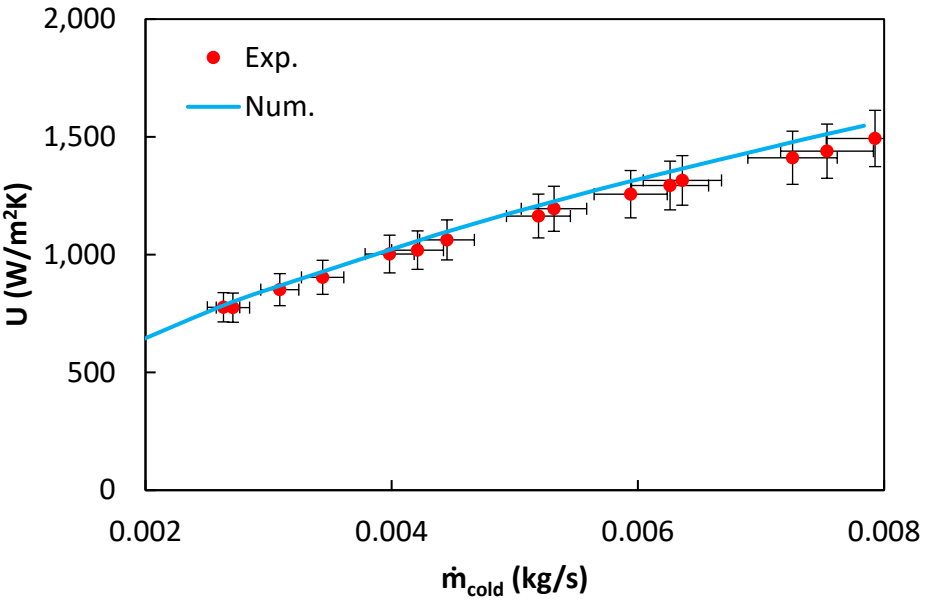

(c)

Figure 7-8: Experimental and numerical results for constant hot-side mass flow rate at 0.019 kg/s and 30°C temperature difference between hot and cold inlet air: heat duty (Q) vs. cold-side mass flow rate ($\dot{m}_{cold}$) (a); cold-side pressure drop (ΔP_{cold}) vs. cold-side mass flow rate ($\dot{m}_{cold}$) (b); overall heat transfer coefficient (U) vs. cold-side mass flow rate ($\dot{m}_{cold}$) (c)

Analyzing the overall trend, it also shows that heat duty, cold-side pressure drop, and overall heat transfer coefficient all increase as cold-side mass flow rate increases. Comparing the trend between Figure 7-7 and Figure 7-8, it shows that cold-side flow rate has more impact on the heat exchanger's thermal performance. This is due to the fact that the cold-side flow rate is much lower (which is almost 50% of the hot-side flow rate). Therefore, the thermal resistance on the cold side is higher than the hot side, and any improvement in cold-side flow rate can positively impact the overall heat transfer performance.

However, it was noticed that the measured cold-side pressure drop was about 40-50% higher than the numerical prediction, while the hot-side was within 10%. Since both side's pressure drops' numerical predictions were based on the SMMM models with tapered manifold channel, the higher pressure drop on cold side might be due to that the cold side header's design induced a non-uniform flow distribution when the flow enters the cold-side manifold channels, which means the mass flow rate in each cold-side manifold channel was not equal. As shown in Figure 7-9, the hot-side header design has several air deflectors to guide the air from the nozzle to the inlet of each hot-side manifold channel. But the cold-side header's design only has two flat channels to separate the inlet air so that it enters either top or bottom manifold channels on the cold side. As a result, the flow entering the cold side might not be as uniform as the flow entering the hot side.

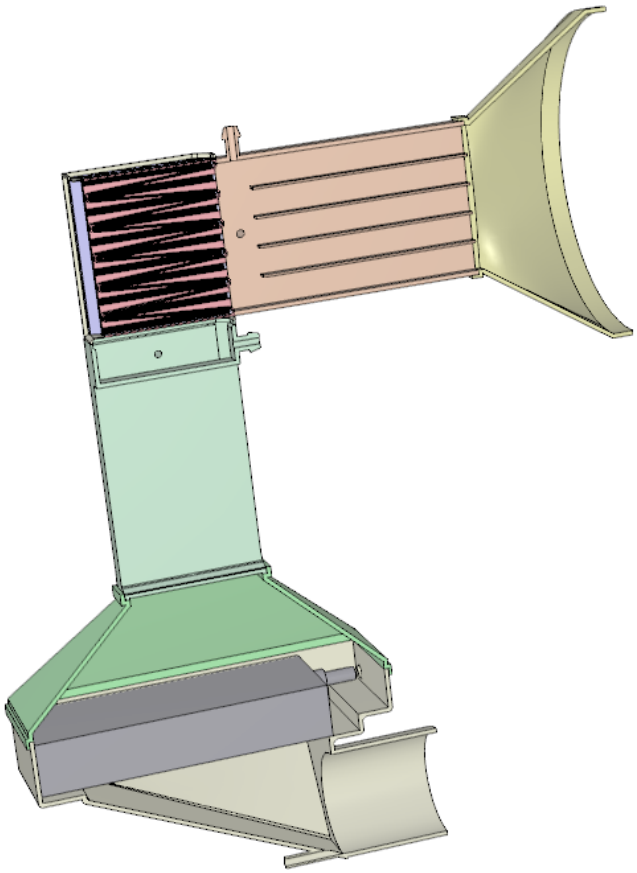

(a)

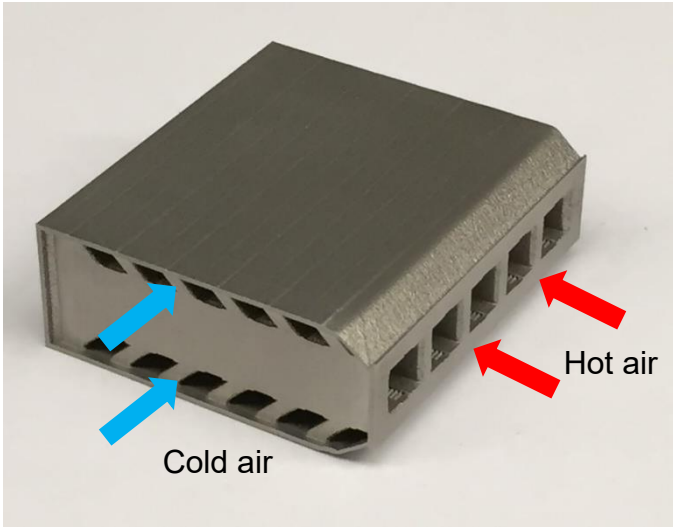

(b)

Figure 7-9: Cross section view of the headers' design (a); hot & cold side of the subscale unit (b)

7.6. Summary

In summary, the single-manifold-multi-microchannels model, which can be used to replace the single manifold-microchannel model in the modified hybrid method, is discussed. It shows that even the flow maldistribution from the straight manifold channel design is less than 30%, a more uniform flow distribution can be obtained with the tapered manifold channel design. The low-temperature experimental setup for performance characterization as well as the test conditions are presented. Based on the low-temperature experimental results, it shows that the measured pressure drop on cold side is 40-50% higher than the numerical prediction, which might be due to the non-uniform flow distribution at the subscale unit's cold-side inlet surface induced by the header's design.

Chapter 8: High-temperature Performance Characterization

8.1. Introduction

Since the gas-to-gas cross-flow manifold-microchannel heat exchanger was designed for high temperature applications, to ensure the fabricated subscale unit can work as expected, this chapter discusses the performance characterization of the 3-D printed subscale unit under high-temperature (600°C) conditions. Considering most material cannot withstand high temperatures, and the press-fit connection does not work well with metal-to-metal interface, custom designed metal headers were created and skillfully welded to the subscale unit. A full CFD model including both inlet/outlet headers and heat exchanger core is discussed since the effect of the headers (such as flow distribution at the inlet surface of the subscale unit and pressure drop induced by the inlet/outlet headers) need to be considered. Experimental tests under high-temperature conditions were performed to evaluate the heat exchanger's performances. Lastly, the experimental results were compared with the numerical predictions and conventional high temperature heat exchanger's performance.

8.2. Headers Design for High-temperature Experiment

For high-temperature experiment, since test temperature is around 600°C, inlet/outlet headers on both sides have to be fabricated with high-temperature-resistant material. Considering the subscale unit was fabricated using Inconel 718 which has an operating temperature up to 750°C, and to save fabrication time for

complex designs which could not be easily built through conventional techniques, the high-temperature headers were designed based on 3-D metal printing (DMLS) using Inconel 718 as well. Based on the low-temperature experimental results, it was found that non-uniform flow induced by the header might increase the measured pressure drop significantly. To improve the uniformity of the flow entering the subscale unit, flow deflectors have been added into each header's design as shown in Figure 8-1.

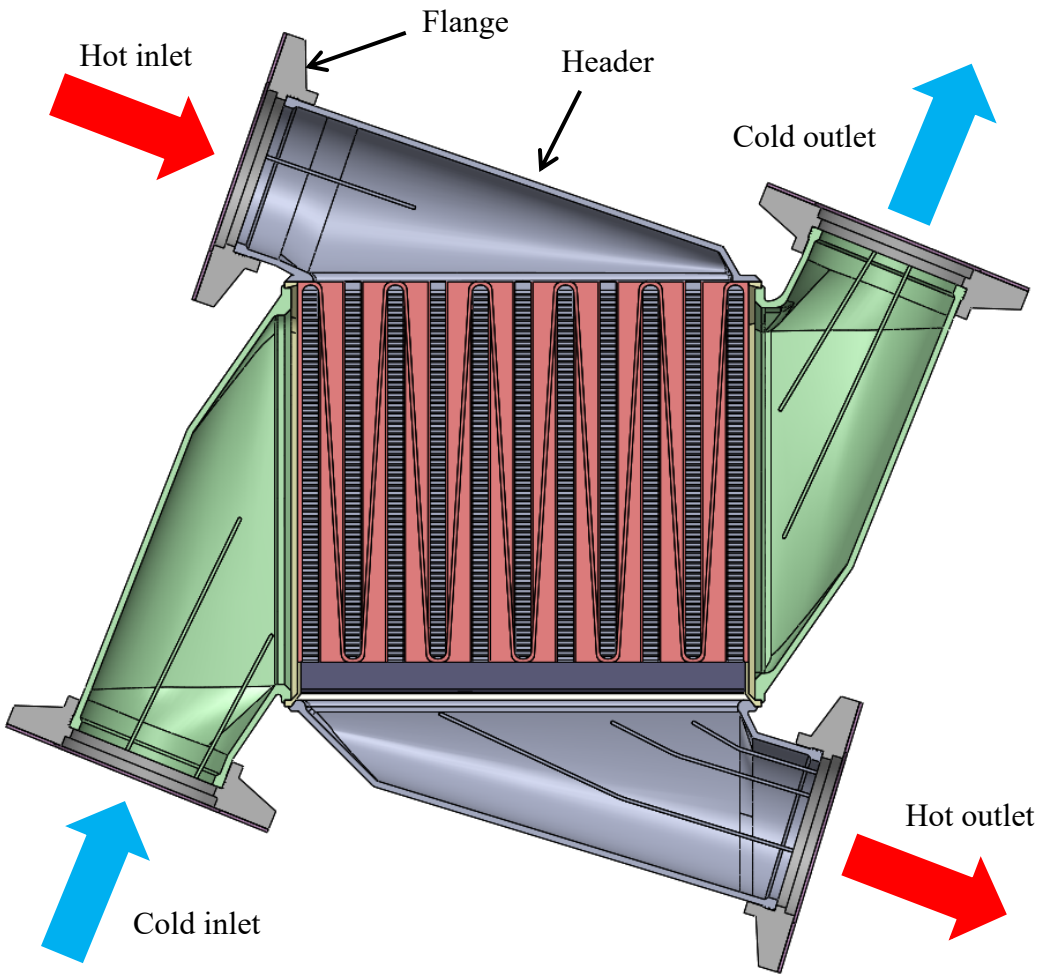

Figure 8-1: Cross section view of headers' design attached to the subscale unit

Large surface area can easily cause very high heat loss when 600°C gas flows inside the headers, which in turn may induce a high heat balance value between hot and cold sides. Compared to the low-temperature headers as shown in Figure 7-5, the high-temperature headers were designed as compact as possible to reduce the surface area. The inlet/outlet of each header was designed as a 1 in OD tube so that the 1 in flanges, which was used to connect the test section to the high-temperature experimental setup, could be welded to the headers. Considering press-fit connection does not work well with metal-to-metal interface under high-temperature conditions, the metal headers were decided to be welded to the subscale unit, and the connection interface of metal headers were modified as shown in Figure 8-2. Due to the interface design of the subscale unit, the hot-side inlet header has more contacting surface area compared to the other three.

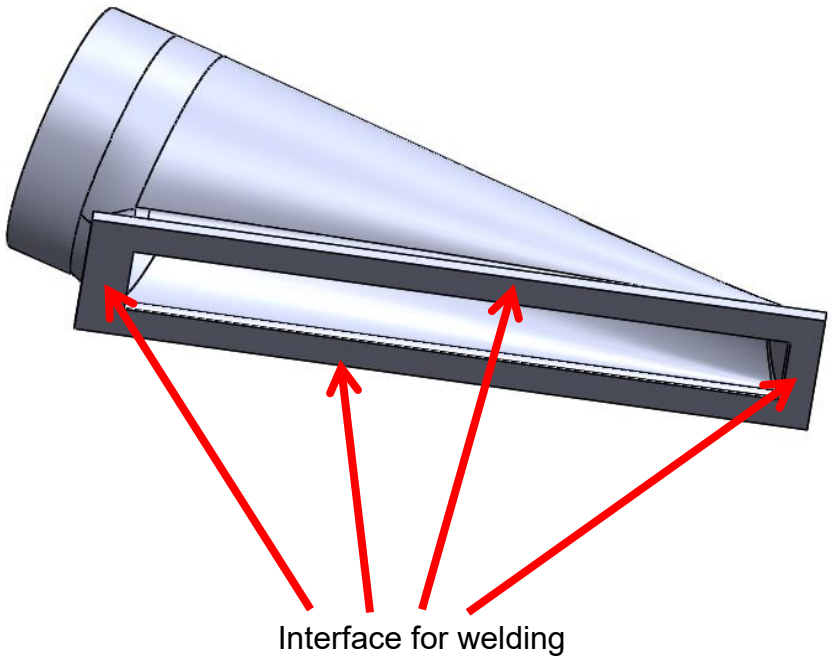

(a)

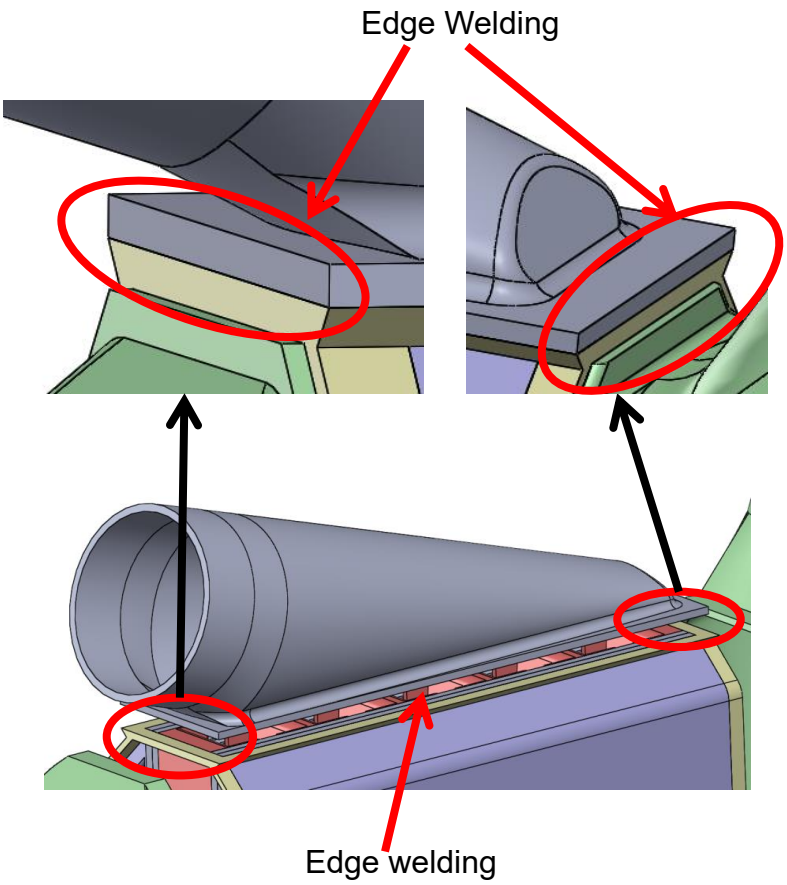

(b)

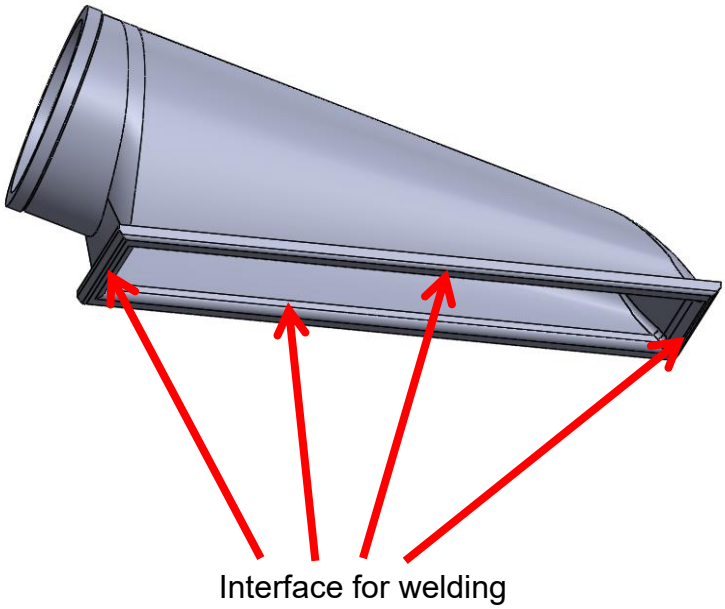

(c)

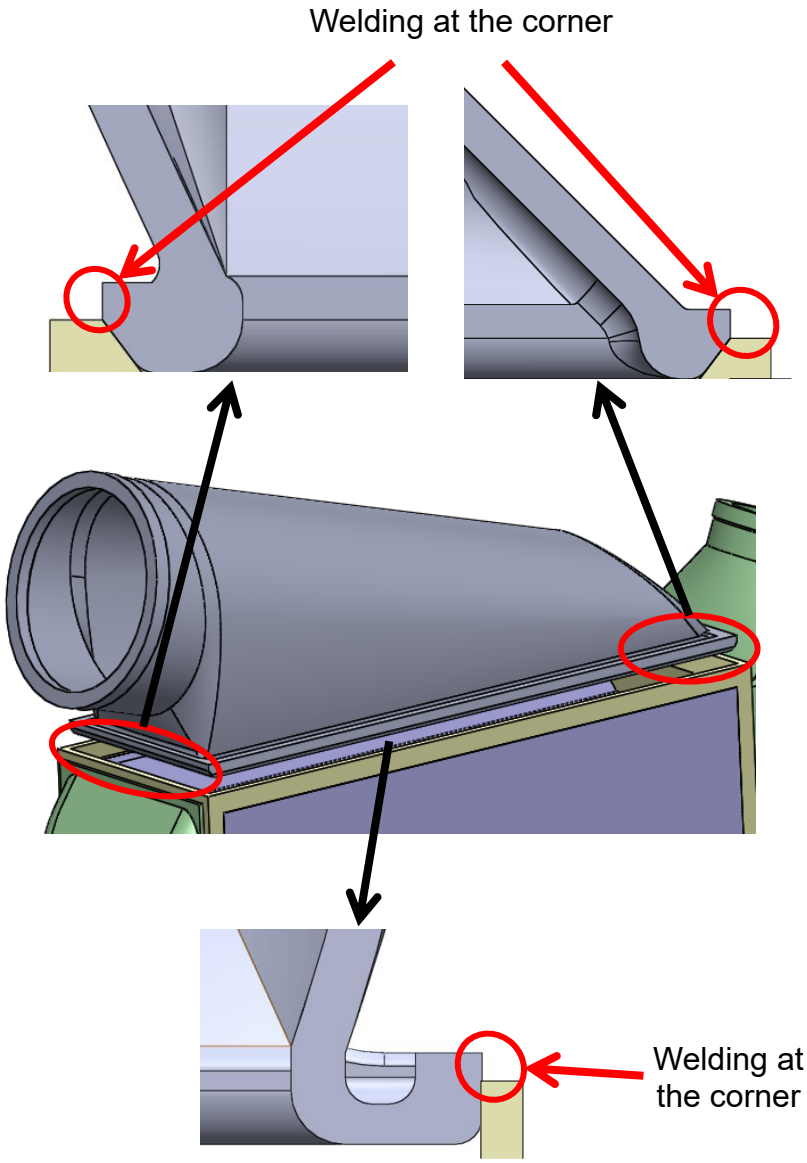

(d)

Figure 8-2: Metal header's connection interface design: for hot-side inlet header (a) & (b); for hot-side outlet and cold-side inlet/outlet headers (c) & (d)

Since metal material's strength reduces at high operating temperature, a welding safety factor calculation was performed considering the required system pressure

on hot side is 64.7 psia and 14.7 psia on cold side. Based on the welding joint design, the force (F_w) it can withstand was calculated as

$$F_w = P \times W \times YS \tag{25}$$

where P is the total length of the weld (which is also the perimeter of the welding edge), W is the width of the weld which is about 0.5 mm, and YS is the yield strength of the as-welded Inconel 718 based on the material spec sheet as shown in Table 8-1.

Table 8-1 Inconel 718 spec sheet [110]

Temperature, °F	Tensile Strength, ksi	Yield Strength (0.2% Offset), ksi
Room	135.0	76.0
1000	119.5	55.5
1200	120.0	72.0
1400	103.0	64.5
1600	74.5	52.5

Note: for high temperature condition, assuming the yield strength reduction ratio of the welded material is similar to parent material, the yield strength of the as-welded material can be about 68 ksi (469 MPa) at 1200°F (650°C).

For the header under system pressure, the force applied to the header (F_p) was calculated as

$$F_p = A \times (N \times P_{sys}) \tag{26}$$

where A is the projected area of the header, N is the design coefficient for system pressure which means the applied pressure is 1.5 times the required value, and P_{sys} is the required system pressure.

Then, the safety factor SF was obtained as

$$SF = \frac{F_w}{F_p} \tag{27}$$

Based on the calculations for both hot- and cold- inlet/outlet headers, the safety factors are included in Table 8-2. As all safety factors are more than 10, it was concluded that connecting the metal headers to the subscale unit through welding would be a safe and reliable approach to prepare the test section (which includes headers, flanges, and the heat exchanger core as shown in Figure 8-1) for the high-temperature experiments.

Table 8-2 Estimated welding safety factor (at 650°C)

Header Name	**P (mm)**	**W (mm)**	**YS (MPa)**	**A (mm^2)**	**N (-)**	**P_{sys} (MPa)**	**SF (-)**
Hot side inlet	186.1	0.5	469	1410	1.5	0.448	46
Hot side outlet	194.3	0.5	469	1,811	1.5	0.448	37
Cold side inlet/outlet	171.7	0.5	469	1,606	1.5	0.101	165

8.3. Flow Simulation with Metal Header

Even though it was considered to add flow deflectors into each header's design to improve the uniformity of the flow entering the subscale unit, no empirical correlations could be used to determine the length, location, and shape of the deflectors. Therefore, considering the computational time, Solidworks flow simulations have been performed as a preliminary method to check whether uniform flow could be obtained through the custom designed flow deflectors inside

each header. By trial and error, a preliminary header design could be created with a flow maldistribution less than 5% based on the flow simulation results using Solidworks.

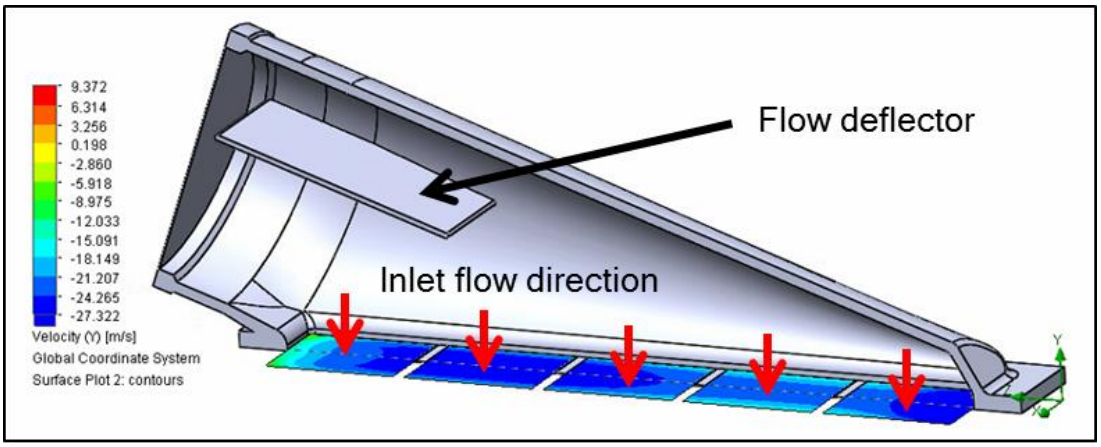

Flow distribution of hot side inlet header at inlet mass flow rate of 0.026 kg/s, negative value of velocity (y) means air is flowing down normal to the surface

(a)

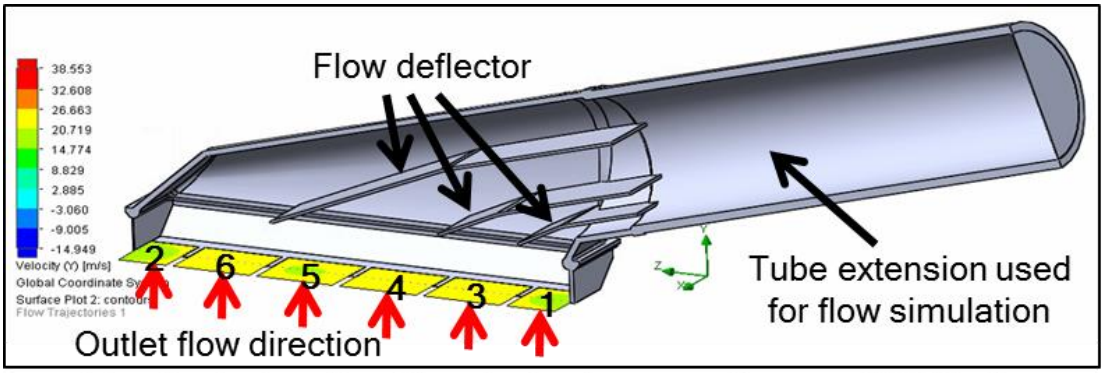

Flow distribution of hot side outlet header at mass flow rate of 0.026 kg/s (surface 1 & 2 are half size channels, surface 3 -6 are full size channels)

(b)

Figure 8-3: Solidworks flow simulation results: hot-side inlet header (a); hot-side outlet header (b)

As shown in Figure 8-3, the flow simulation using Solidworks includes the solid body of the header design. For hot-side inlet header, the 1 in tube surface at inlet was set as mass flow rate inlet with constant inlet temperature. The five uniform manifold channel inlet areas of the subscale unit on the hot side were set as pressure outlet. No symmetry boundary was used as the Solidworks flow simulation includes the entire flow region within the header. The cross-section view in Figure 8-3 is only for the purpose of showing the structure inside header.

For hot-side outlet header, the manifold channel outlet areas of the subscale unit on the hot side were set as mass flow rate inlet with constant temperature. A 1 in tube extension was added at the outlet surface of the header design to avoid re-circulation at the header's outlet surface. The extension's outlet surface was then set as pressure outlet. One thing needs to be noticed is that half manifold channels were observed at the hot-side outlet of the subscale unit as well as cold-side inlet/outlet due to the flow behavior inside the manifold-microchannel heat exchanger. Therefore, the flow maldistribution of hot-side outlet header as well as cold-side inlet/outlet headers was evaluated as

$$F = \sqrt{\frac{\sum_{i=1}^{2}(\dot{m}_i - \frac{\dot{m}_{tot}}{2\times(n-1)})^2}{2\times(\frac{\dot{m}_{tot}}{2(n-1)})^2} + \frac{\sum_{i=3}^{n}(\dot{m}_i - \frac{\dot{m}_{tot}}{n-1})^2}{(n-2)\times(\frac{\dot{m}_{tot}}{n-1})^2}} \qquad (28)$$

where area 1 and 2 are half size manifold channels, area 3 – 6 are full size manifold channels as shown in Figure 8-3 (b).

For cold-side inlet/outlet headers, similar boundary conditions and simulation approach were used. Based on the Solidworks flow simulation results, it showed that the original header design without any flow deflector usually has a flow maldistribution of ~ 20 – 40% with different inclined angles, which is the angle between the contacting surface of the subscale unit and the 1 in tube surface of the header. By adding deflectors inside headers, after multiple design iterations through trial and error, the best flow maldistribution results obtained from Solidworks flow simulation were indicating ~ 4% maldistribution for hot-side inlet header, ~ 8% for hot-side outlet header, ~6% for cold-side inlet header, and ~ 8% for cold-side outlet header.

However, due to the complexity of the subscale unit deign and the small microchannel size, the Solidworks flow simulation cannot include the subscale unit, which means the simulation result may not be accurate since the flow resistance from the heat exchanger core is not considered. To ensure the assumption of uniform flow distribution from headers among all manifold channels, and to get a more accurate and reliable flow simulation result, another Fluent flow simulation (including both inlet/outlet headers and heat exchanger core) was performed to determine whether the mass flow rate in each manifold channel is equal with the header design obtained based on the Solidworks flow simulation results.

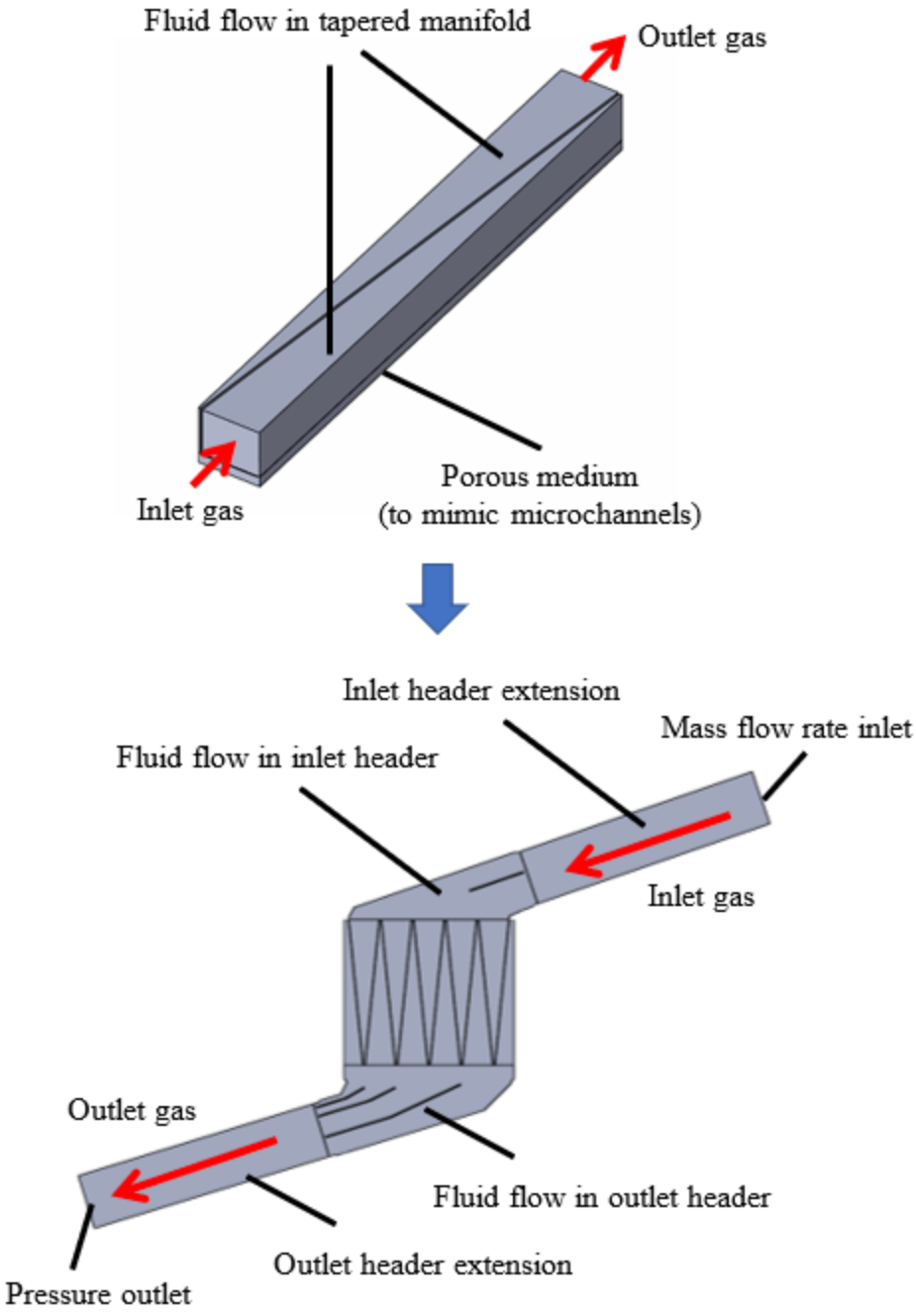

Figure 8-4: Simplified single manifold-porous-medium model (top); hot-side full model with inlet/outlet headers (bottom)

Since the measured pressure drop of the test section includes pressure drop of the inlet and outlet headers, this Fluent simulation can also predict the total pressure drop from the inlet header to the outlet header. As shown in Figure 8-4, in order to reduce computational time, microchannels were replaced with a porous medium in the simplified model. For the simplified single manifold-porous-medium model, the same boundary conditions of the SMMM model were applied. Based on a grid independency study, it was concluded that about 1,300,000 computational elements were sufficient for the simplified model. Starting with the simplified single manifold-porous-medium model, the porous medium parameters were calibrated by matching the pressure drop obtained from the SMMM model for a range of the same mass flow rates as shown in Figure 8-5. Then, the calibrated porous medium parameters were used in the full model to predict the total pressure drop, which includes pressure drops of both the inlet and outlet headers.

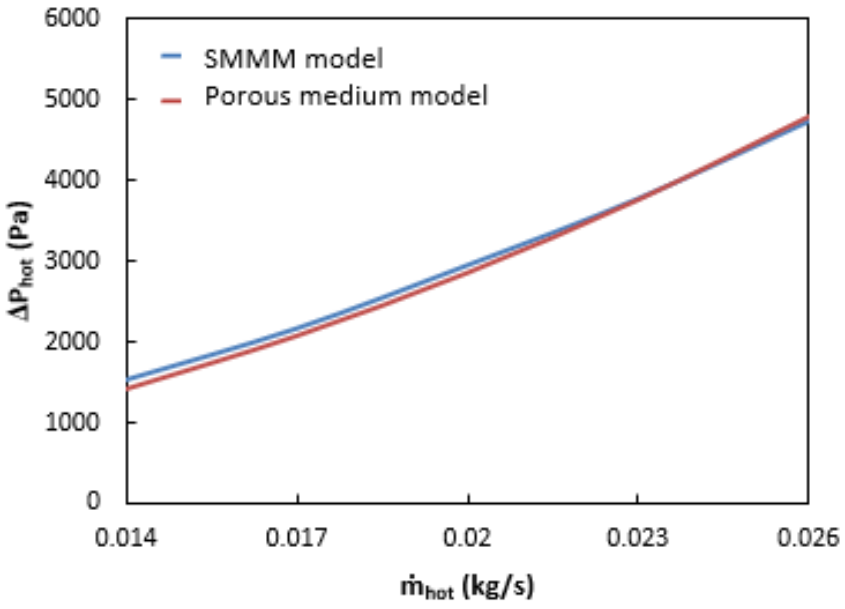

(a)

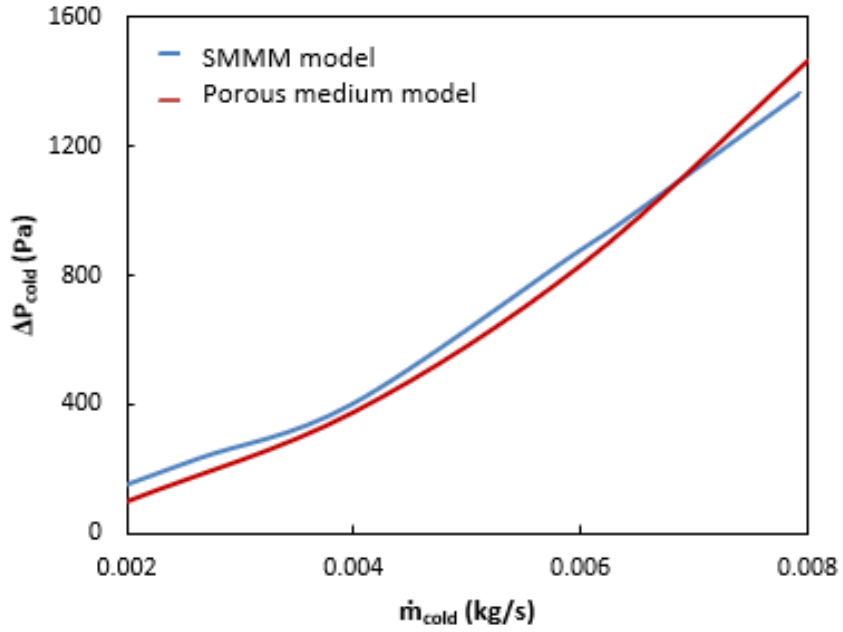

(b)

Figure 8-5: Porous medium calibration: hot-side core pressure drop vs hot-side mass flow rate (a); cold-side core pressure drop vs cold-side mass flow rate (b)

For the full model, the inlet surface of the inlet header extension was set to mass flow rate boundary condition. The outlet surface of the outlet header extension was set as pressure outlet boundary condition. The symmetry boundary condition was applied on the plane where the headers and manifold channels are cut in half. The result of a grid independency study showed that about 8,500,000 computational elements were sufficient for the full model.

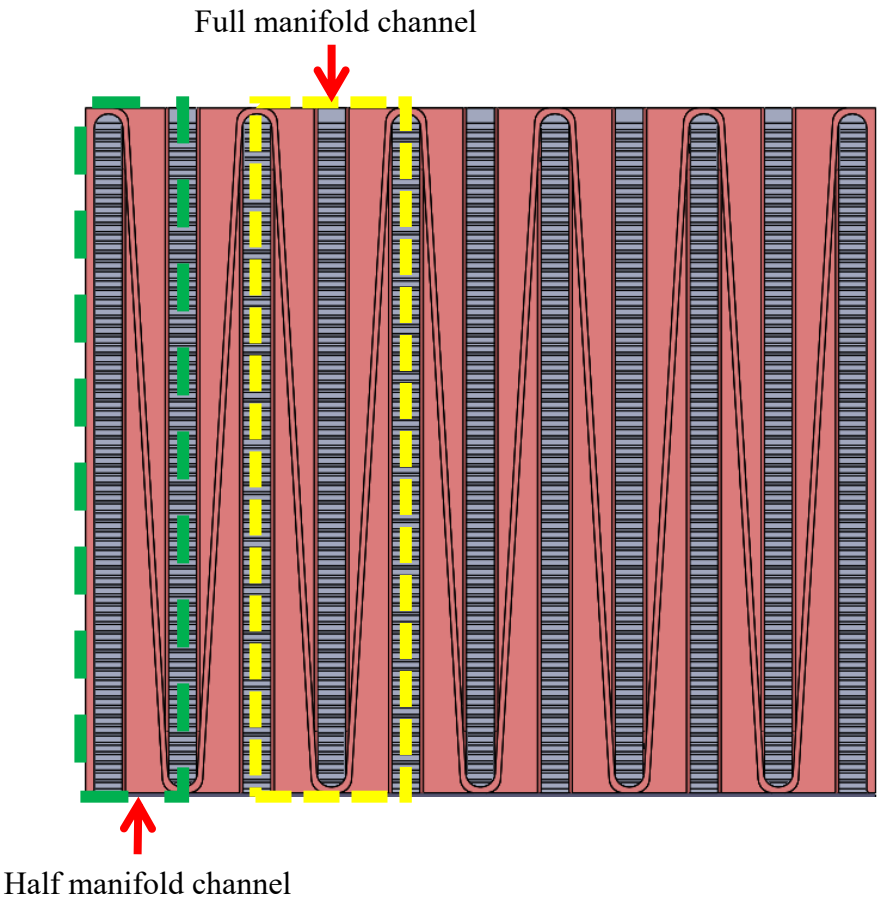

Figure 8-6: Cross-section view of manifold channels on hot side (5 full manifold channels as inlet channel, 2 half & 4 full manifold channels as outlet channel)

As discussed before, due to the characteristics of manifold-microchannel heat exchanger's flow path, half manifold channels were included in the subscale unit design as shown in Figure 8-6. Therefore, a uniform flow distribution means that mass flow rate at the half manifold channel needs to be half of the full manifold channel. Based on the full model's simulation results, the mass flow rate at each manifold channel could be obtained, and it indicated that flow maldistribution is 6 – 8% for hot-side inlet/outlet headers, and 3 – 5% for cold-side inlet/outlet headers as shown in Figure 8-7.

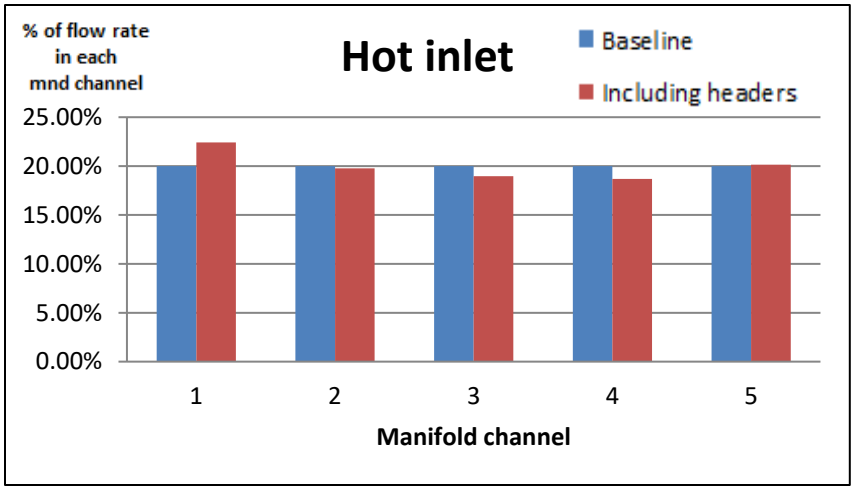
% of flow rate in each mnd channel
Hot inlet
Baseline
Including headers
25.00%
20.00%
15.00%
10.00%
5.00%
0.00%
1
2
3
4
5
Manifold channel

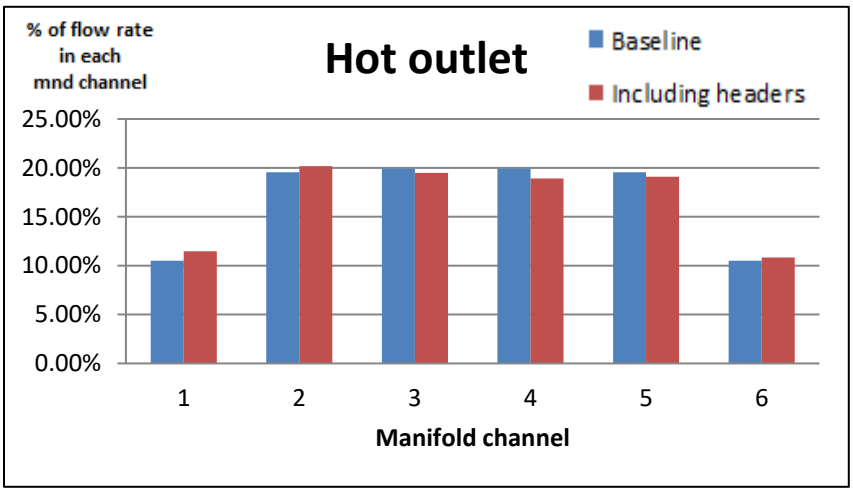
% of flow rate in each mnd channel
Hot outlet
Baseline
Including headers
25.00%
20.00%
15.00%
10.00%
5.00%
0.00%
1
2
3
4
5
6
Manifold channel

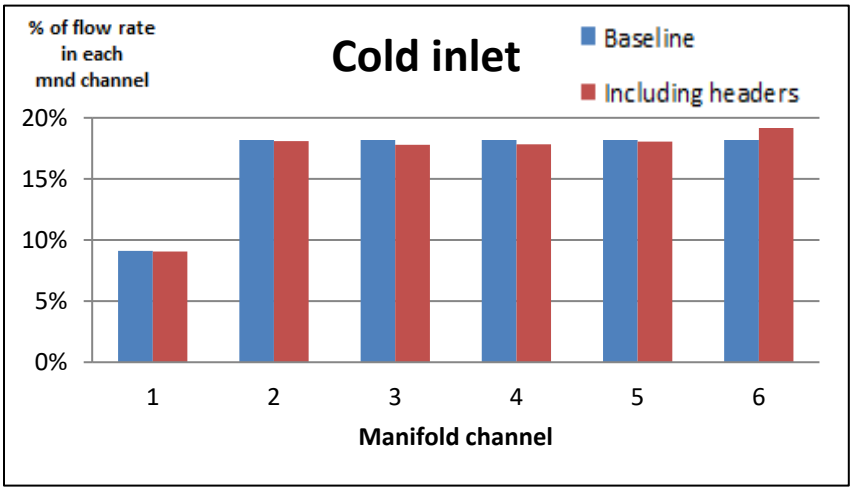
% of flow rate in each mnd channel
Cold inlet
Baseline
Including headers
20%
15%
10%
5%
0%
1
2
3
4
5
6
Manifold channel

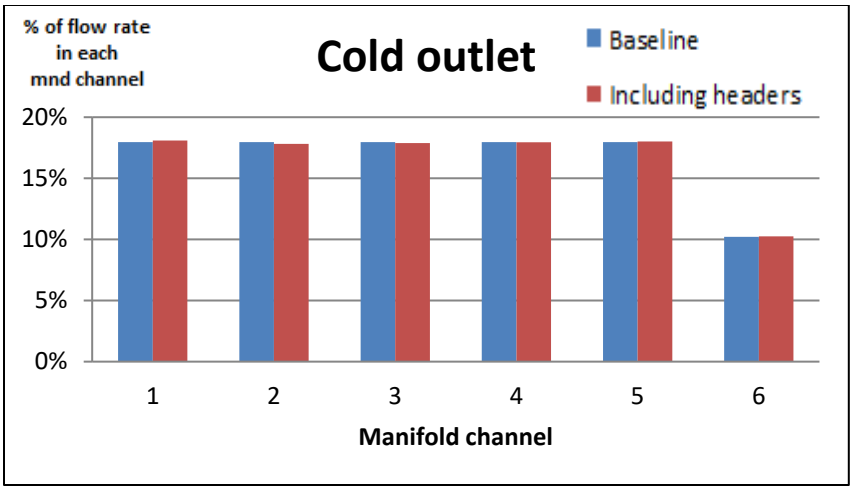

Figure 8-7: Flow distribution in each manifold channel (hot-side mass flow rate at 0.02 kg/s, cold-side mass flow rate at 0.006 kg/s)

8.4. Metal Headers Fabrication & Evaluation

Since the metal header design does not have any small feature (< 0.5 mm) that requires a high-resolution 3-D metal printer, all four headers were fabricated based on the printing orientation shown in Figure 8-8 through the DMLS process with normal resolution (30 μm per layer). However, supporting structures were added by the manufacturer as the welding interface of all headers' design has the overhang issue. After the 3-D printing process, the headers together with the supporting structures were removed through wire EDM. The supporting structures were then removed with a power rotary tool, and the headers were polished using sandpaper to improve the surface finish quality of the overhung welding interface area.

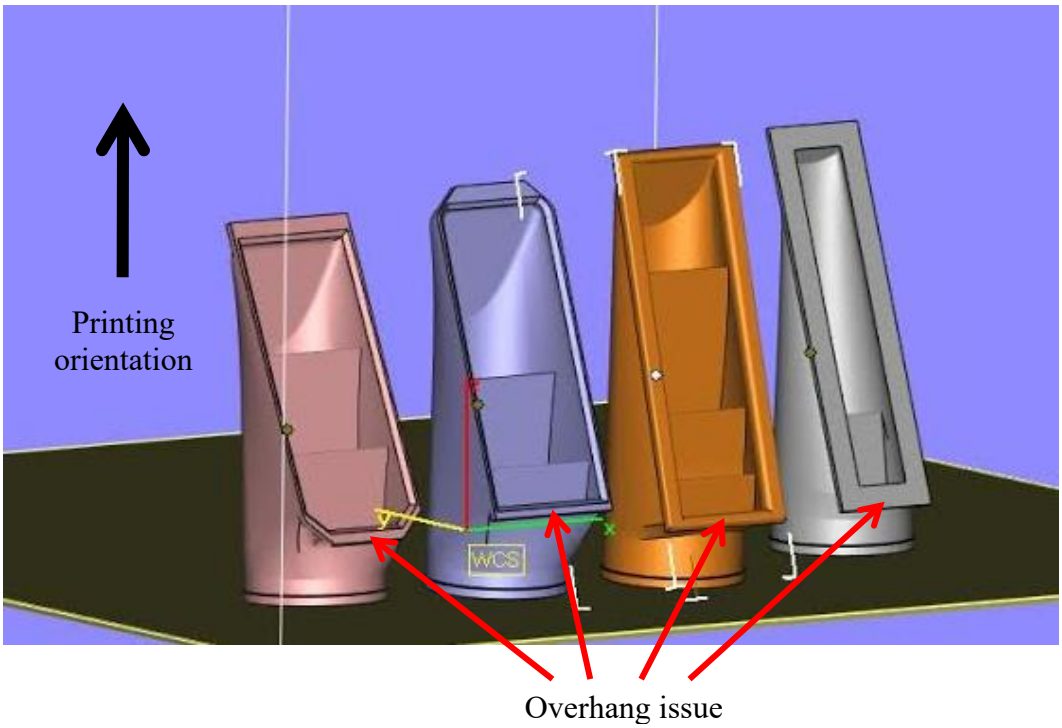

Figure 8-8: 3-D printing orientation of the metal headers

As shown in Figure 8-9, the metal headers' as-built surface finish was stated by the manufacturer as 5 – 10 μm Ra. The density of 3-D printed headers was evaluated by measuring the weight with a scale and measuring the volume with water in a test tube. The results showed the density was ~8.081 g/cm^3, which is 99% of the raw material density for Inconel 718 provided by the manufacturer. It was also noticed that the measured mass of the 3-D printed headers was ~8% less than the design value. According to the manufacturer, this might be due to the volume loss during the post-processing such as that more welding interface was machined away with the power rotary tool when removing the supporting structures.

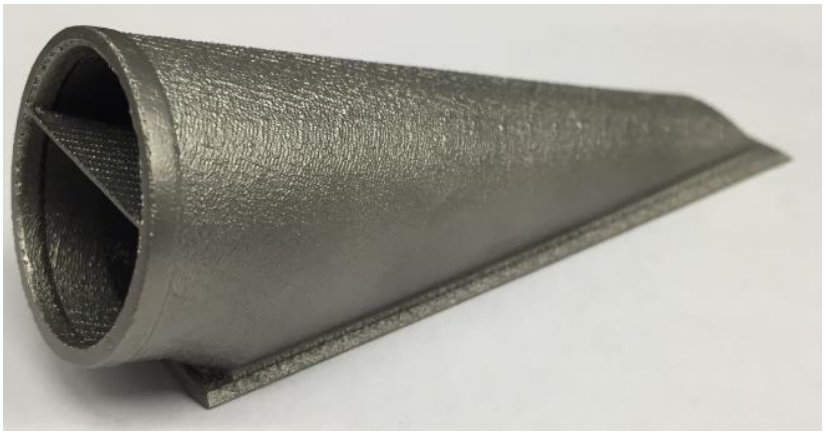

(a)

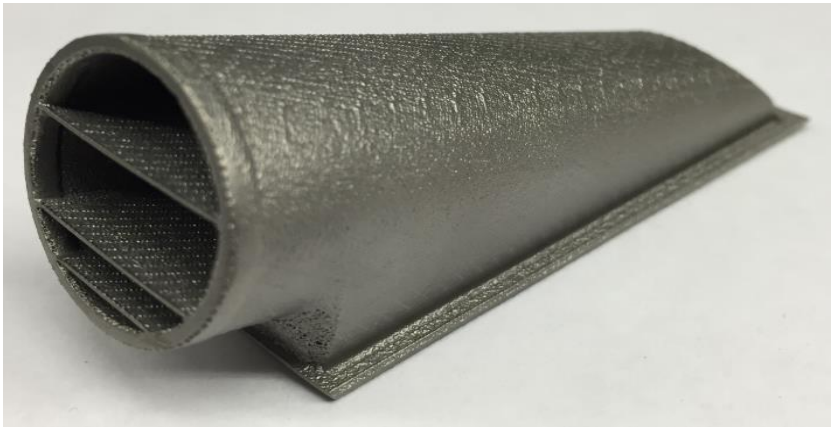

(b)

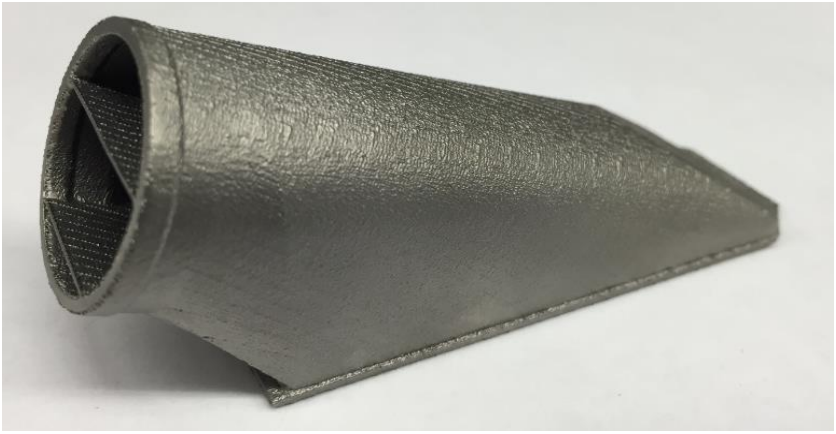

(c)

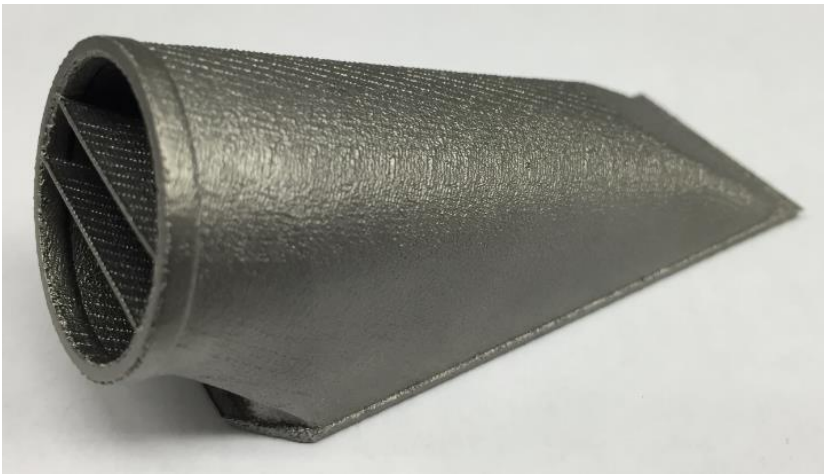

(d)

Figure 8-9: Hot-side inlet header (a); hot-side outlet header (b); cold-side inlet header (c); cold-side outlet header (d)

8.5. Assembled Test Section

As previously discussed, the test section for the high-temperature experiment includes hot- / cold-side headers, flanges, and the heat exchanger core (the subscale unit). All parts were decided to be assembled through welding. However, since headers and the subscale unit were 3-D printed through DMLS process, it was unclear what quality could be obtained after welding these 3-D printed metal pieces together. To ensure a successful welding job, an experienced welder was invited, and a small welding-trial piece was prepared as shown in Figure 8-10 (a). The welder cut the welding-trial piece in half and tried to weld them back-to-back through edge welding as shown in Figure 8-10 (b). According to the welder, these 3-D printed metal pieces were still weldable. However, due to the voids inside the parts (which might have trapped some noble gas such as Argon during the sintering

process), welding 3-D printed Inconel 718 is much more difficult than the raw material.

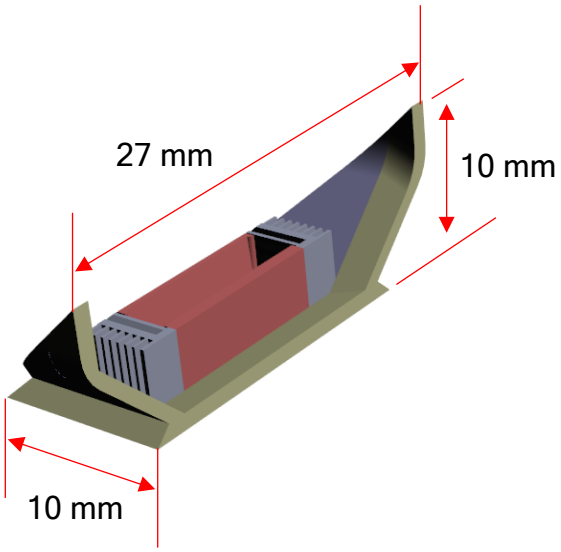

(a)

(b)

Figure 8-10: A section from the subscale unit design (a); Welded 3-D printed welding-trial section through edge welding (b)

In order to connect the test section to the high-temperature experimental setup, flanges and clamps connection was selected. For tube OD of 1 inch, the metal

flanges' burst pressure is rated as 1200 psia at 800°F which is more than 10 times the required system pressure [111]. However, to weld the flanges to the headers, flanges made of Inconel 718 were needed, which are not commonly available in the market. Based on flange's design standard and the welder's suggestion, a modified flange design for use of flat gasket was created (Figure 8-11 (a)). As shown in Figure 8-11 (b), four Inconel 718 flanges were fabricated through conventional machining process. To ensure there is no gas leakage from the contacting surface between two flanges under required system pressure of 64.7 psia, a 0.02-inch-thick Flexible Grafoil gasket was used which has a service temperature up to 815°C.

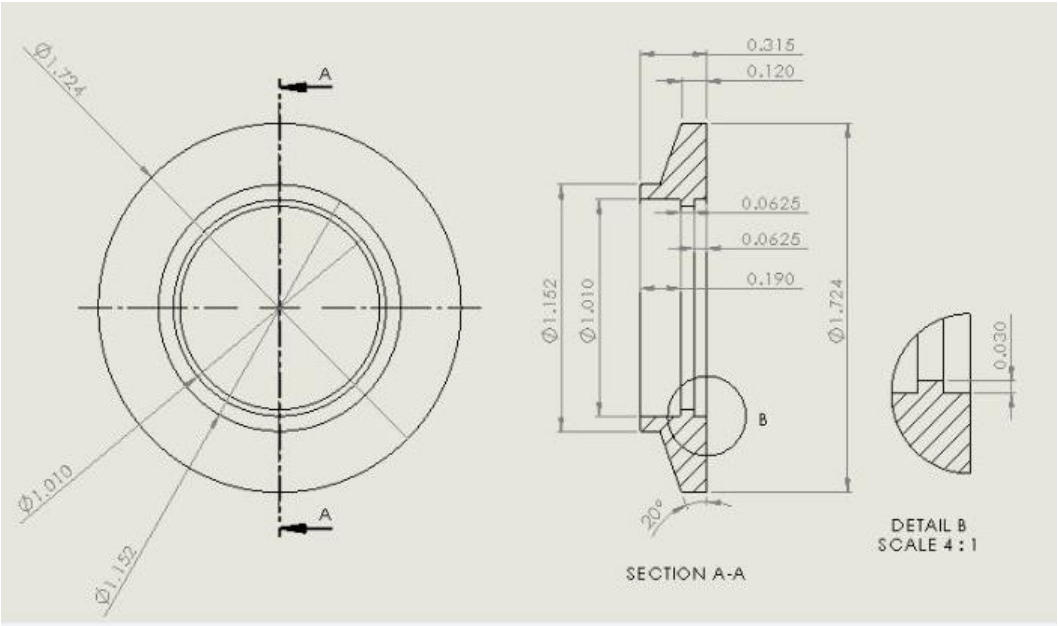

(a)

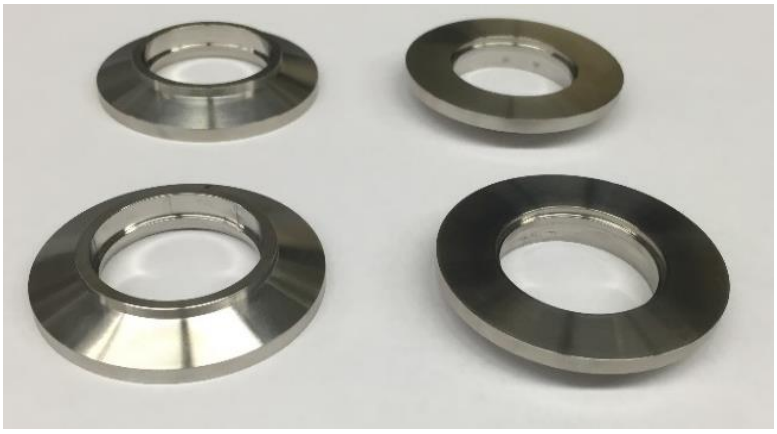

(b)

Figure 8-11: Modified Inconel 718 flange's engineering drawing (unit: inch) (a); fabricated Inconel 718 flanges through conventional machining (b)

Since a tight-fit was required by the welder, and the 3-D printed headers could not directly fit into the subscale unit as well as the flanges, to complete the assembly of the test section, headers and subscale unit were post-processed through a precise machining. After the post-process, all pieces of the test section were fitted into each other tightly before welding as shown in Figure 8-12.

Figure 8-12: Test section including core, headers, and flanges before welding

The test section was successfully welded together, however some leakages were identified after the first welding job. As it was leaking at several points from the welding line to the ambient when the test section was pressurized, more welding was applied to seal the identified leaking points. After multiple trials, the test section was eventually proved to be leak-free (no leakage from hot side to cold side through headers, and no leakage from the pressurized test section to the ambient) as shown in Figure 8-13. This assembly process also demonstrated the feasibility of welding additively manufactured and conventional machined Inconel 718 parts.

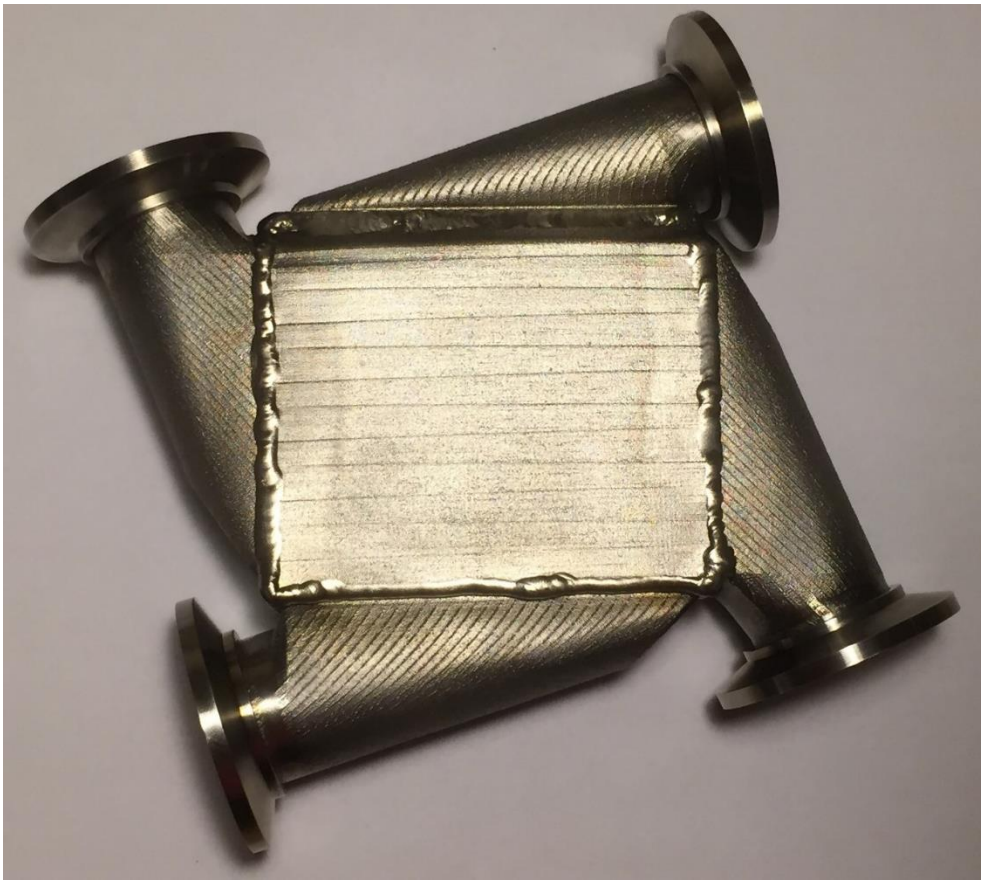

Figure 8-13: Welded test section including core, headers, and flanges

8.6. High-temperature Experimental Setup

A high-temperature experimental setup was built from scratch to characterize the performance of the test section under high-temperature (600°C) conditions. As the hot side has a system pressure of 64.7 psia based on the design requirements discussed in chapter 3, the setup's hot side was initially designed as an open loop with a compressor to supply the pressure and flow rate. However, a compressor which can supply 0.02 kg/s air at 64.7 psia requires at least 15 – 20 HP power supply, has a giant size that required too much laboratory space, and would cause huge noises. Therefore, a close loop was designed for the hot side with a smaller size compressor. To supply the required flow rate within the close loop, a 3 HP oil-free scroll enclosed compressor, which can use pressurized gas as inlet flow, was selected as shown in Figure 8-14.

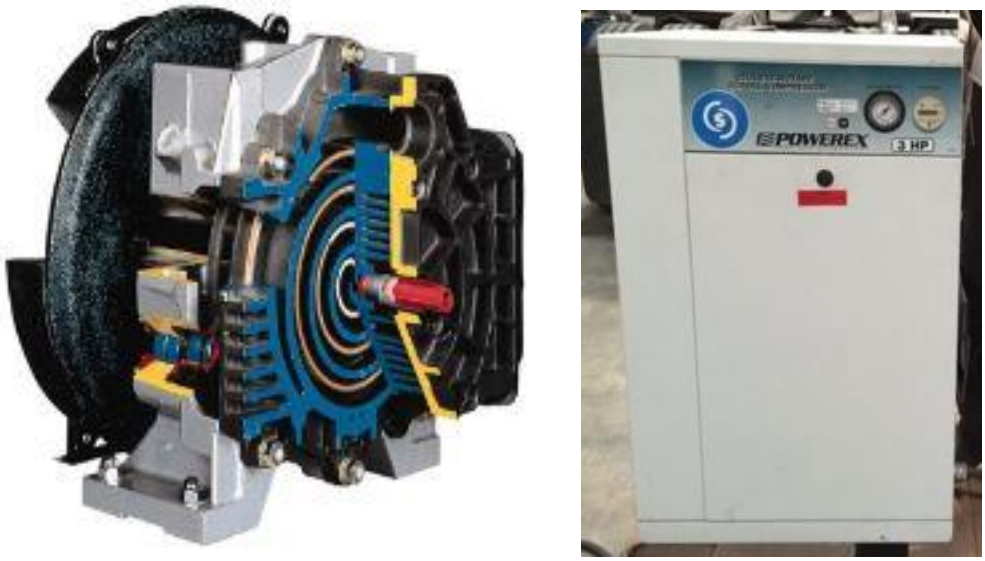

Figure 8-14: Powerex oil-free scroll compressor pump [112] (left); 3 HP scroll compressor system

Because the hot-side inlet temperature for the subscale unit was required as 650°C, a commercial electric heater which has a capacity of 13 kW with 3-phase power (@ 208 V) was selected. Based on the specification, the heater which is made from Stainless Steel 304 could supply a maximum exhaust gas temperature of 704°C (1300°F) and withstand a maximum pressure of 120 psig. With an average Nitrogen temperature of 300°C at the given pressure of 64.7 psia, a pressure drop of ~16 psig is expected when mass flow rate inside the heater is 0.02 kg/s. This high pressure drop is due to the S-shape flow path inside the heater as shown in Figure 8-15, and can be compensated by the selected compressor.

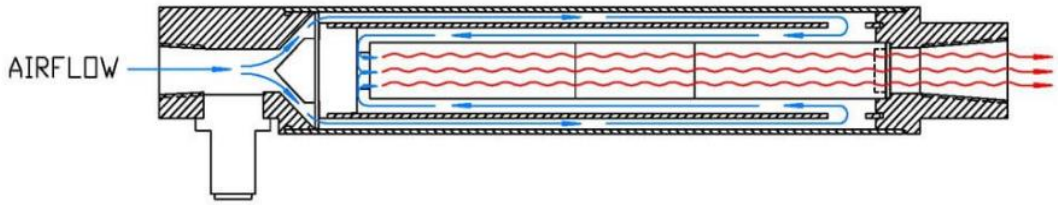

Figure 8-15: Schematic of the commercial heater

However, as a commercial product for standard industrial applications, the heater did not have a connection option as the flange/clamp type used in the high-temperature setup. Therefore, a modified flange design was created to replace the original exhaust fitting ring of the commercial electric heater (as shown in Figure 8-16) so that it could be installed in the setup. The modified flange was then fabricated at University of Maryland and delivered to the heater's manufacturer to be welded to the heater.

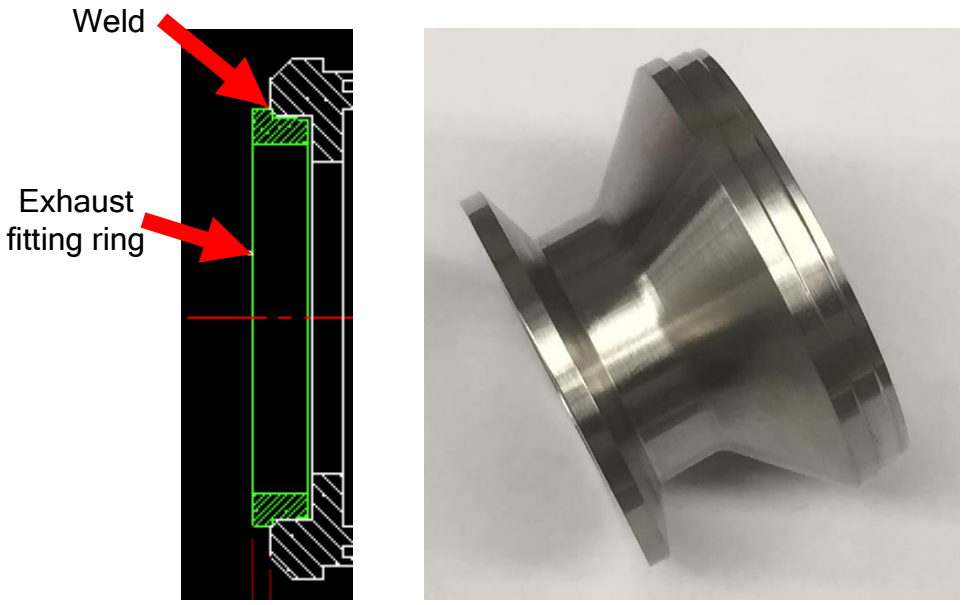

Figure 8-16: Original exhaust fitting ring design on the heater (left); Modified stainless steel 304 flange as replacement of the original exhaust fitting ring (right)

The electric heater was controlled by a PID controller provided by its manufacturer, however, fuses were not included in the control panel due to the large size of the high-current fuse and the limited space within the control box. As a result, custom designed fuse holder was 3-D printed using high-temperature-resistant plastic material (which can withstand a maximum temperature of 200°C), and three 50 Amp fuses were installed inside the fuse holder. As shown in Figure 8-17. Considering most of the risks during the high-temperature experiments (which are discussed at the end of this section) could be related to the electric heater, a 3-phase power emergency switch, a flow rate relay (check hot-side minimum flow rate), and a temperature relay (check compressor inlet temperature) were added in the power system.

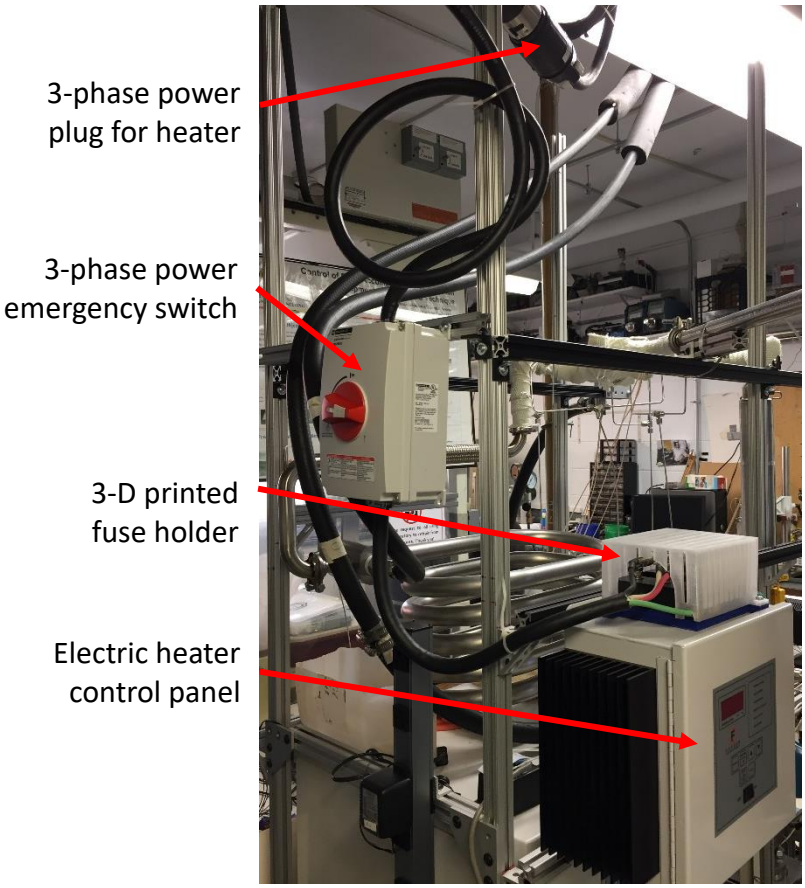

Figure 8-17: Power switch & control panel for the electric heater

Since the subscale unit of the gas-to-gas manifold-microchannel heat exchanger has a cross-flow configuration, it has a chance to create non-uniform flow temperatures at the hot- and cold-outlets. In order to obtain a uniform flow temperature measurement, custom designed mixing chambers were created. To ensure the measured location inside the mixing chamber can represent the average temperature, Solidworks flow simulations were performed by assuming the temperature varies 50°C across the inlet cross-section of the mixing chamber. As shown in Figure 8-18 and Table 8-3, at the measured location, the simulation results for this extreme case show that the measured temperature is almost the same as the

average temperature at mixing chamber's inlet for the range of mass flow rates. Similar results are obtained for other mixing chambers.

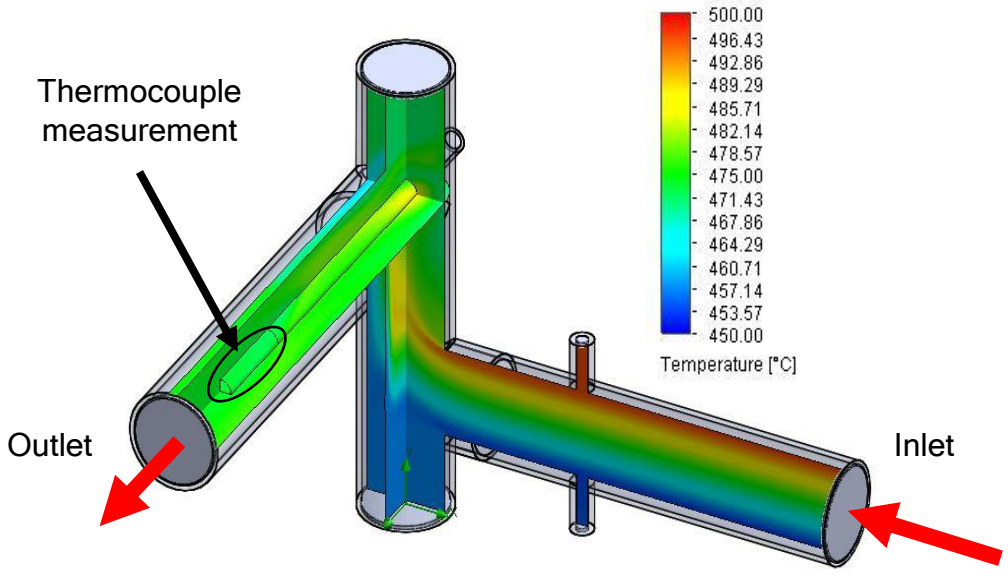

Figure 8-18: Numerical model of hot-side outlet mixing chamber at mass flow rate of 0.02 kg/s

Table 8-3 Flow simulation results of the hot-side outlet mixing chamber

$\dot{m}_{hot}$ (kg/s)	T_{avg} @ inlet (°C)	T_{avg} @ TC location (°C)	ΔT_{avg} (°C)	$\Delta T_{avg}/T_{avg}$ @ inlet (%)
0.010	475.0	472.9	-2.1	-0.44%
0.015	475.0	473.2	-1.8	-0.38%
0.020	475.0	473.0	-2.0	-0.42%

The schematic diagram of the high-temperature experimental setup is shown in Figure 8-19. In summary, to reach the required system pressure, the hot side was built as a closed loop with N_2 gas as the working fluid supplied via a N_2 gas cylinder. A scroll compressor, controlled by a variable speed controller, was used to provide the desired flow rate. A 13-kW electric heater was installed on the hot side to heat the N_2 gas stream to 600°C. A 20-kW chiller and an air-to-water heat exchanger (Heat Exchanger 1) were used on the hot side to cool the N_2 exhaust from the outlet of the test section to ensure the gas temperature at the inlet of compressor was less than 20°C. Coriolis flow meters were used to measure the mass flow rates on both the hot and cold sides. The cold side was built as an open loop with atmosphere system pressure. On the cold side, air was used as the working fluid, and a blower controlled by a variable speed controller was used to provide the desired flow rate. During the high temperature test, the entire setup needs to be run for at least 30 minutes for a proper steady temperature measurement. Because of long operation of the blower, the outlet air from the blower will increase to more than 45°C for an inlet blower temperature of 25°C. A pre-cooler (Heat Exchanger 2) was used on the cold-side to maintain a constant cold-side inlet temperature (~ 38°C). Pressure transducers and high temperature thermocouples were used to measure the pressure drops and temperatures. On both the hot and cold sides, custom designed mixing chambers ensured uniform temperature measurements at both the inlets and outlets of the test section.

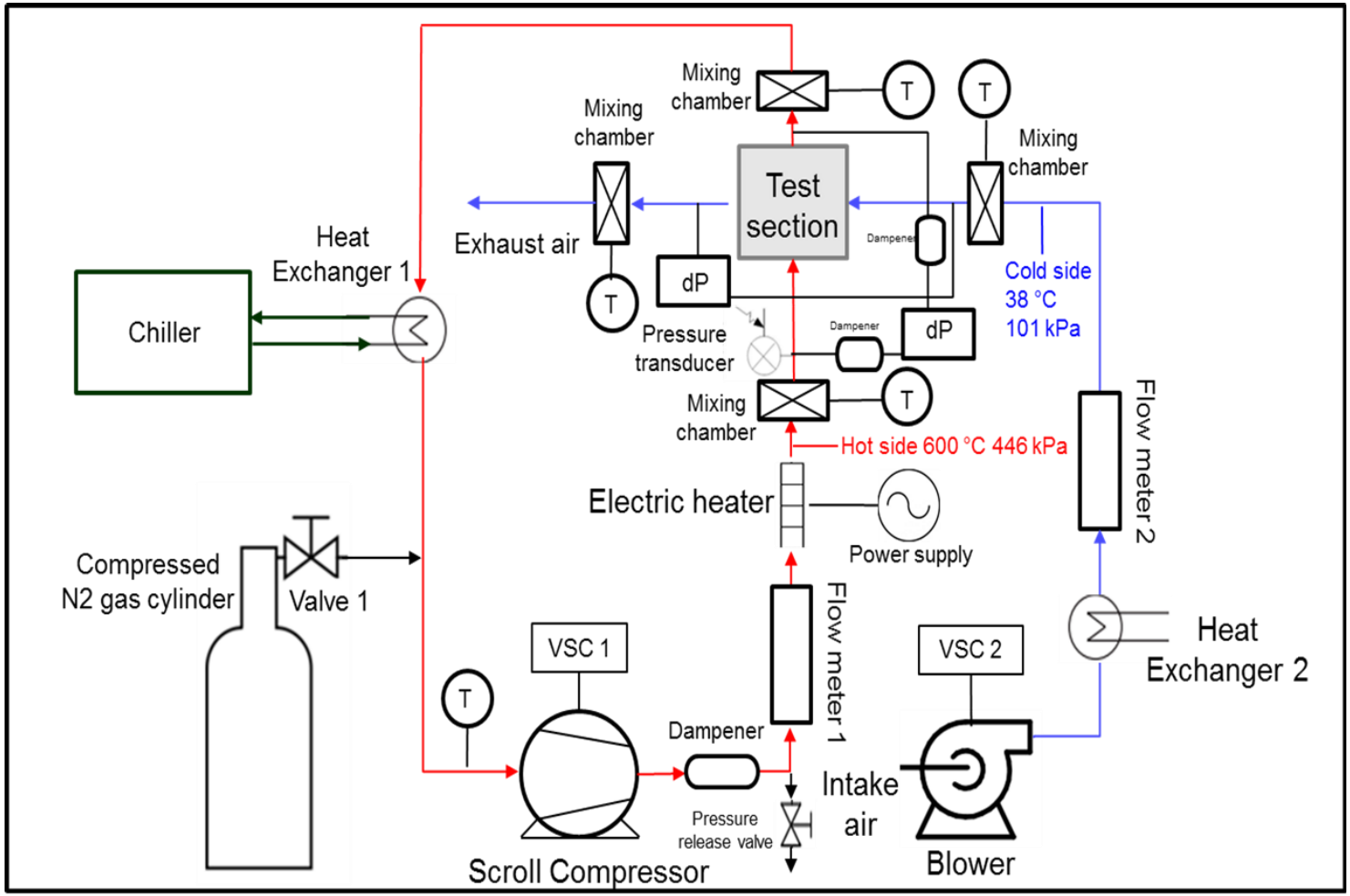

Figure 8-19: Schematic diagram of the high-temperature experimental setup

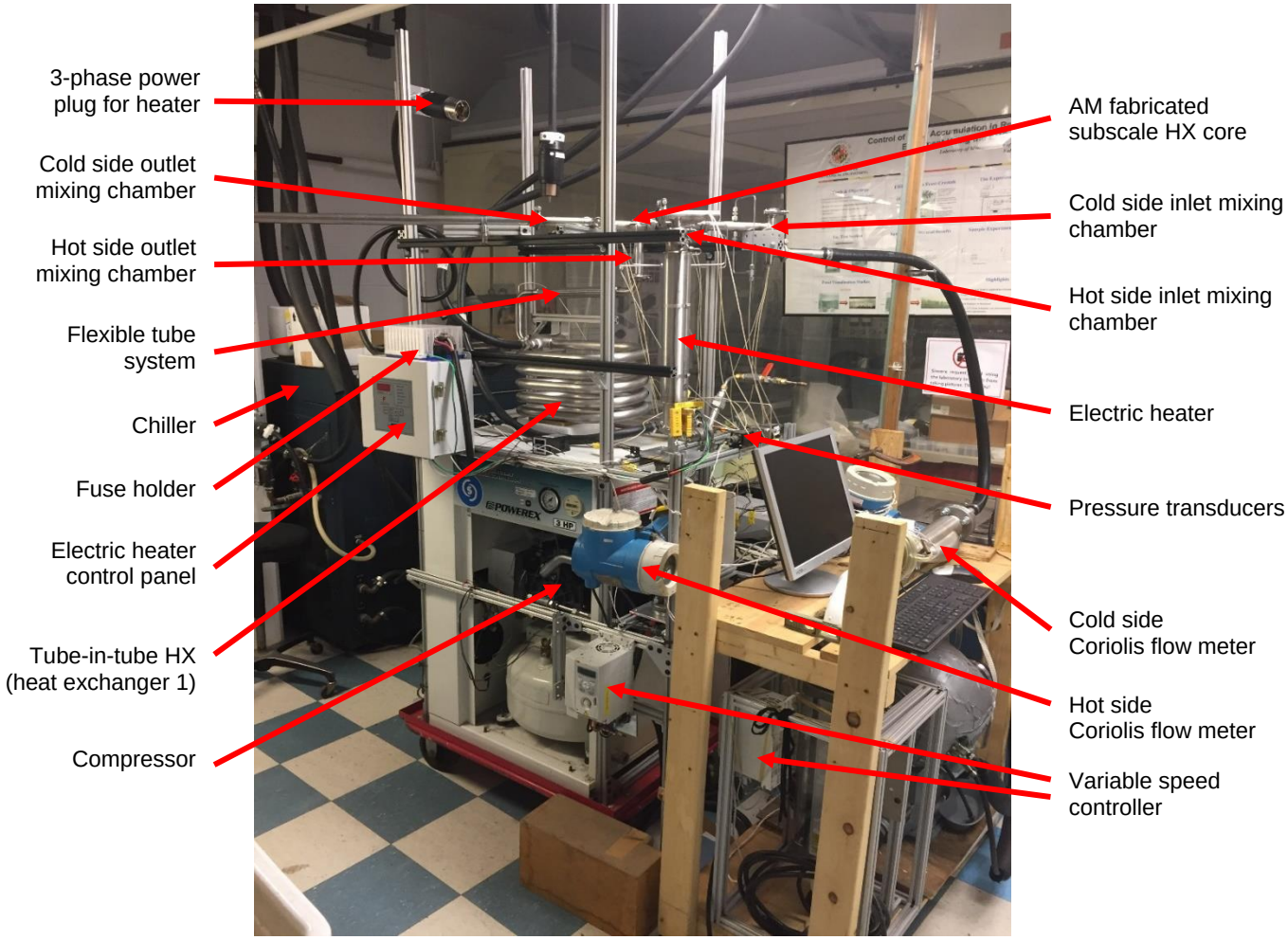

Figure 8-20: High-temperature experimental setup

The high-temperature experimental setup is shown in Figure 8-20, where the test section was connected to the setup through flanges/clamp connection with flexible graphite gasket to prevent leakage from contacting flanges' surfaces. Three thermal insulation layers were also covered the entire test section and all mixing chambers to reduce heat loss during high temperature tests as shown in Figure 8-21.

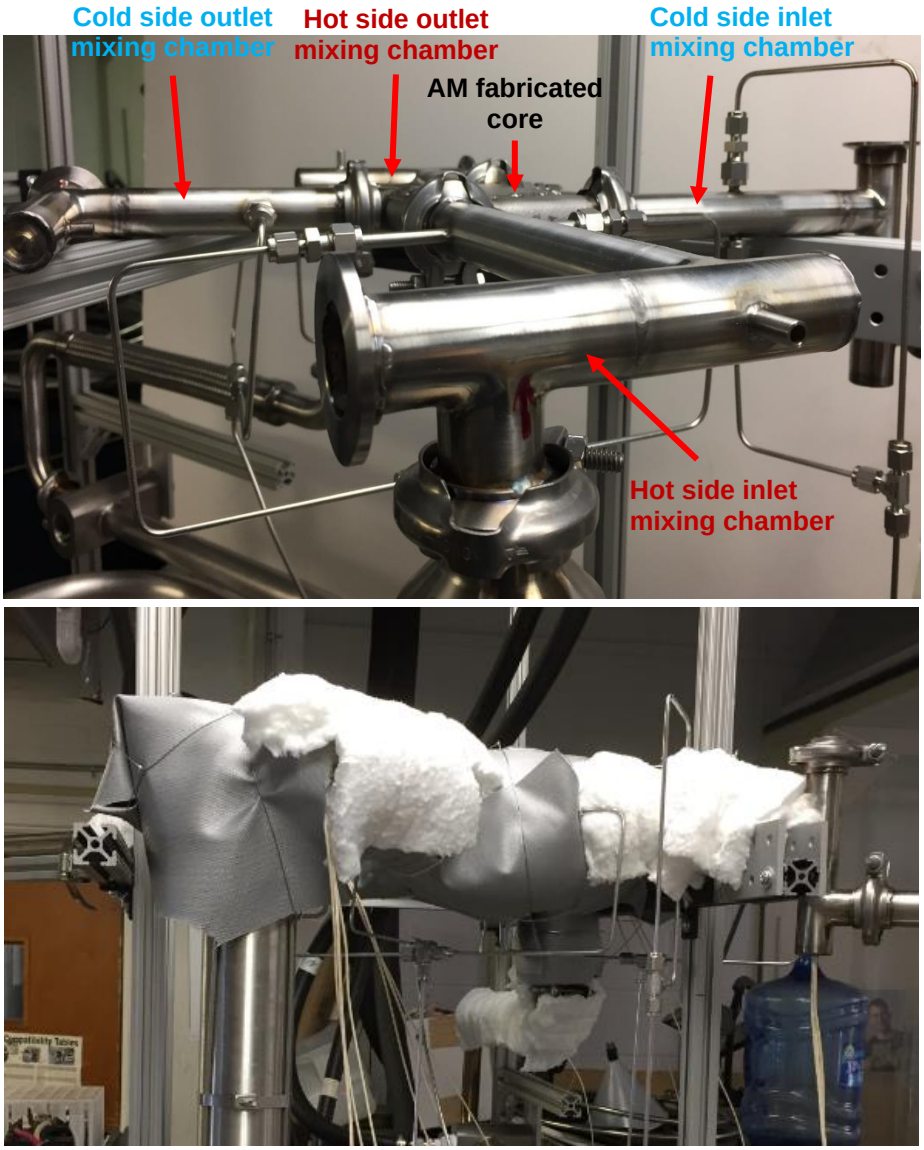

Figure 8-21: Test section & mixing chambers: before installing thermal insulation (top), after installing thermal insulation (bottom)

Considering the risks involved with the high-temperature experiment setup (such as pressurized N_2 gas was heated to 600°C or more through a 13-kW electric heater), a hazard and operability analysis was conducted before the high-temperature tests as shown in Table 8-4. Even the high-temperature setup was well prepared and insulated, if blower or compressor stops working properly, certain risks still need to be considered and methods of mitigation have been concluded in the table as well.

Table 8-4 High-temperature test hazard and operability analysis

	Condition	**Effect**	**Risk**	**Mitigation**
Cold side air flow	No flow	Compressor inlet temperature too high	Compressor damaged	Temperature relay off → heater off
	Low flow	Vent exhaust is hot	Vent paint damaged	Additional cooling fan
	High flow	N/A	N/A	N/A
Hot side N_2 flow	No flow	Heater minimum flow not reached	Heater damaged	Flow relay off → heater off
	Low flow	Heater minimum flow not reached	Heater damaged	Flow relay & Temperature relay off → heater off
	High flow	Compressor inlet temperature too high	Compressor damaged	Temperature relay off → heater off
Chiller water flow	No flow	Compressor inlet temperature too high	Compressor damaged	Temperature relay off → heater off
	Low flow	Compressor inlet temperature too high & boiling water	Compressor & Chiller damaged	Temperature relay off → heater off
	High flow	N/A	N/A	N/A
System pressure	High	Setup burst	Setup damaged	Pressure relief valve @ 95 psia open
	Low	Heater minimum flow not reached	Heater damaged	Flow relay & Temperature relay off → heater off

8.7. High-temperature Experiment Method

The experiments were performed under high-temperature and adiabatic conditions as shown in Table 8-5 and Table 8-6. Four sets of experiments were conducted. For the high-temperature tests, first the hot-side flow rate was varied while keeping the cold-side flow rate constant at 6 g/s. Then, in the second test, the cold-side flow rate was varied while keeping the hot-side flow rate constant at 20 g/s. For the adiabatic tests, which do not involve any heat transfer, first the hot-side flow rate was varied while allowing no flow on the cold-side (flow rate = 0 g/s). Then, the cold-side flow rate was varied while allowing no flow on the hot-side. During the tests, the hot-side inlet temperature ($T_{hot,in}$), the hot-side outlet temperature ($T_{hot,out}$), the hot-side pressure drop (ΔP_{hot}), the hot-side system pressure (P_{hot}), the hot-side mass flow rate ($\dot{m}_{hot}$), the cold-side inlet temperature ($T_{cold,in}$), the cold-side outlet temperature ($T_{cold,out}$), the cold-side pressure drop (ΔP_{cold}), and the cold-side mass flow rate ($\dot{m}_{cold}$) were measured and recorded.

Table 8-5 High-temperature experimental test conditions

	Hot Side	**Cold Side**
Temperature Condition	600 °C	38 °C
System Pressure	448 kPa	101 kPa
Varying Hot Side Flow Rate	10 – 20 g/s	6 g/s
Varying Cold Side Flow Rate	20 g/s	4 – 11 g/s

Table 8-6 Adiabatic experimental test conditions

	Hot Side	**Cold Side**
Temperature Condition	38 °C	38 °C
System Pressure	448 kPa	101 kPa
Varying Hot Side Flow Rate	0 – 20 g/s	0 g/s
Varying Cold Side Flow Rate	0 g/s	0 – 14 g/s

Based on the measurement, the heat duty (Q) of the subscale heat exchanger was evaluated as:

$$Q_{hot} = Cp_{hot}\dot{m}_{hot}(T_{hot,in} - T_{hot,out}) \quad (29)$$

$$Q_{cold} = Cp_{cold}\dot{m}_{cold}(T_{cold,out} - T_{cold,in}) \quad (30)$$

$$Q = (Q_{hot} + Q_{cold})/2 \quad (31)$$

where Cp is the N_2 or air specific heat for the hot- and cold-sides calculated at the average temperature between the inlet and outlet measurements. The typical deviation observed between Q_{hot} and Q_{cold} was about 6 – 8% (it was about 20% before installing the thermal insulation).

The overall heat transfer coefficient was evaluated using the log mean temperature difference (LMTD) method for both unmixed cross-flow arrangements as given in Eqs. (32) - (35) as a function of inlet and outlet temperatures on both hot and cold sides.

$$dT_A = T_{hot,in} - T_{cold,out} \tag{32}$$

$$dT_B = T_{hot,out} - T_{cold,in} \tag{33}$$

$$LMTD = CF \frac{dT_A - dT_B}{\ln(dT_A / dT_B)} \tag{34}$$

$$U = \frac{\mathrm{Q}_i}{A_{base} LMTD} \tag{35}$$

where CF is the configuration correction factor of both unmixed cross-flow (CF ≅ 0.94 – 0.96), A_{base} is the microchannel base area (A_{base} = 0.059 m × 0.070 m), and Q_i is the heat duty for each manifold-microchannel layer (as shown in Figure 8-22, the subscale unit design has two manifold-microchannel layers, and each layer consists of a full cross-flow microchannel surface, a half hot-side manifolds, and a half cold-side manifolds).

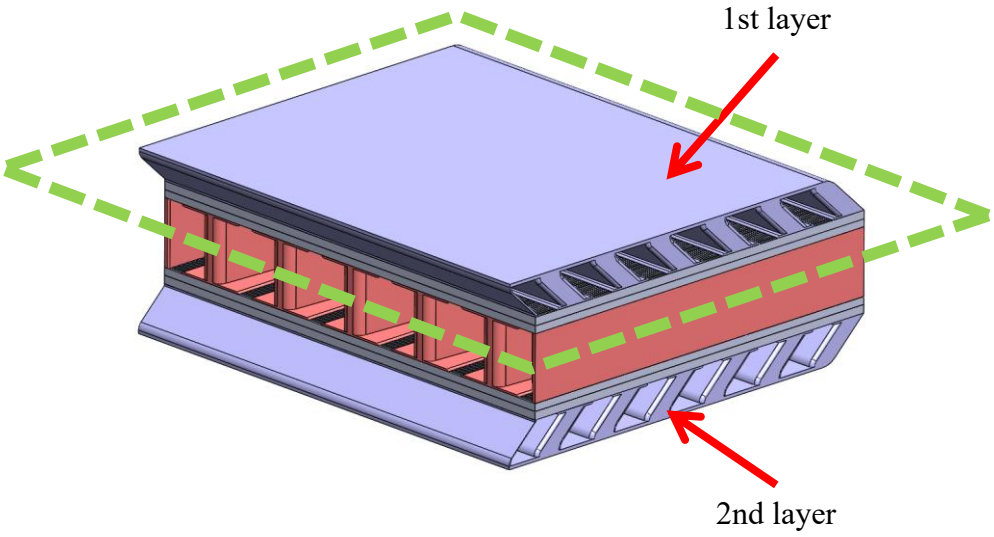

Figure 8-22: Subscale unit's two manifold-microchannel layers

Uncertainty propagation analysis was performed to calculate the uncertainty in the subscale heat exchanger performance parameters (Q, U) due to inaccuracy of the measurements. A list of the measurement equipment is shown in Table 8-7 with the corresponding accuracies. The uncertainty of the calculated quantity Y (U_Y), which is a function of $X_1, X_2, \ldots, X_N$ with uncertainty of $U_{X1}, U_{X2}, \ldots, U_{XN}$, can be calculated using the method explained in NIST Technical Note 1297 [109] as:

$$U_Y = \sqrt{\sum_i \left(\frac{\partial Y}{\partial X_i}\right)^2 U_{X_i}^2} \tag{36}$$

Table 8-7 List of high-temperature measurement equipment and its accuracy

Equipment function	**Equipment name**	**Accuracy**
Hot-side flow rate	Endress Hausser Coriolis flow meter (0.5-inch size)	± 0.5% of measurement
Cold-side flow rate	Endress Hausser Coriolis flow meter (1-inch size)	± 3% of measurement
Temperature	K type thermocouple	± 2.2°C or 0.75% of measurement
Hot-side pressure drop	Validyne P55 pressure transducer	± 0.25% FS of 5.5 kPa
Cold-side pressure drop	Validyne P55 pressure transducer	± 0.25% FS of 5.5 kPa

The uncertainties of the subscale heat exchanger performance parameters (Q, U) were calculated. The maximum uncertainties in Q, U, and ΔP were evaluated as ± 2.50%, ± 5.12%, and ± 0.25% respectively, and the error bars are included in the results presented in the next section.

8.8. High-temperature Experiment Results

The heat transfer performance of the subscale unit for a constant cold-side microchannel Reynolds number is shown in Figure 8-23. The results are plotted as functions of hot-side microchannel Reynolds number ($Re_{chn,\,h}$) which is defined as:

$$Re_{chn,h} = \frac{D_{chn,h}\dot{m}_{chn,h}}{A_{chn,h}\mu_{hot}} \tag{37}$$

where $A_{chn,\,h}$ is the hot-side microchannel cross section area ($A_{chn,\,h}$ = 0.00039 m × 0.00128 m), $D_{chn,\,h}$ is the hot-side microchannel hydraulic diameter ($D_{chn,\,h}$ = 0.0006 m), and $\dot{m}_{chn,h}$ is the mass flow rate per microchannel on the hot-side.

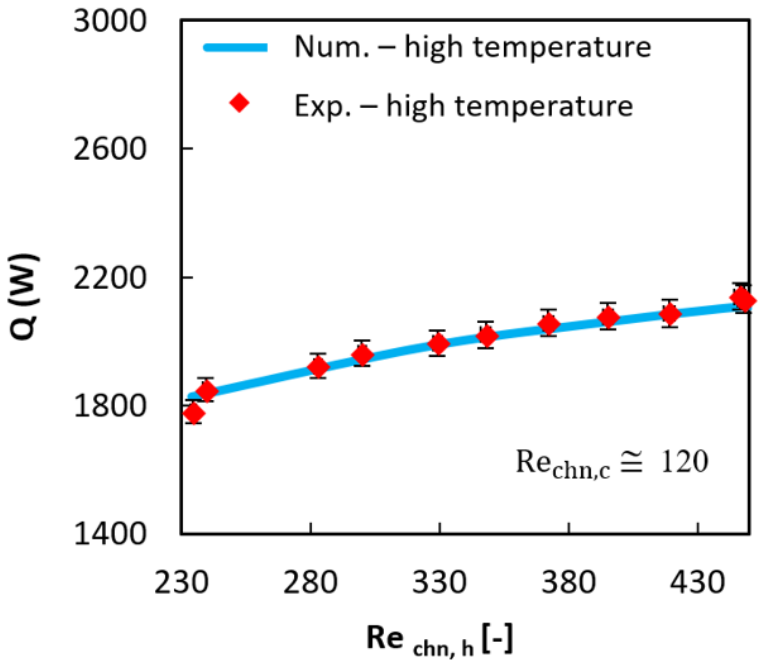

(a)

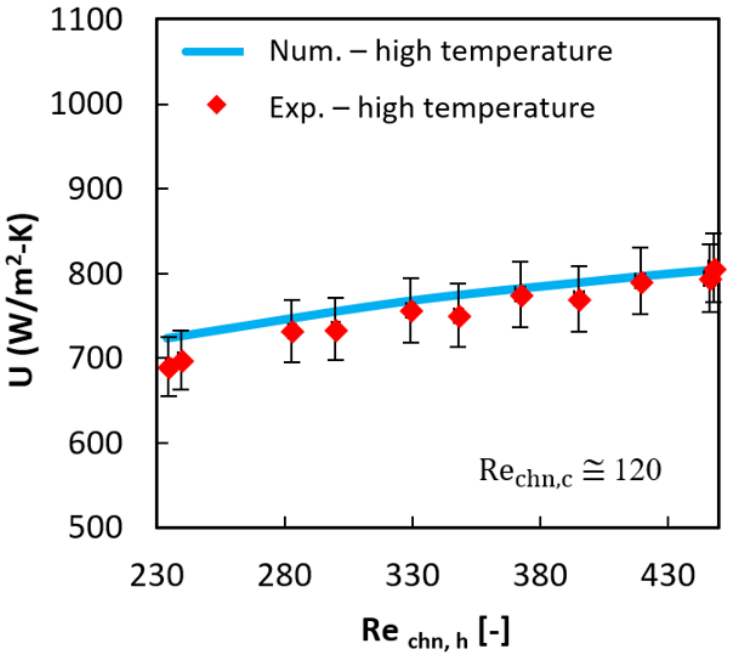

(b)

Figure 8-23: Experimental and numerical results for constant cold-side microchannel Reynolds number ($Re_{chn,c} \cong 120$) and 560°C temperature difference between hot inlet N_2 and cold inlet air: (a) heat duty (Q) vs. hot-side microchannel Reynolds number ($Re_{chn,h}$); (b) overall heat transfer coefficient (U) vs. hot-side microchannel Reynolds number ($Re_{chn,h}$)

Figure 8-23 (a) shows the heat duty variation with the hot-side microchannel Reynolds number for a temperature difference of 560°C between the hot- and cold-sides. Up to 2140 W heat duty was achieved at the hot-side's highest flow rate (when the cold-side microchannel Reynolds number is constant about 120). The overall heat transfer coefficient of the heat exchanger was in the range of 700 – 800 W/m^{2}K as shown in Figure 8-23 (b). This number is higher than the overall heat transfer coefficient of a typical air-cooled heat exchanger with gases as the process fluid,

which is in the range of 50 – 300 W/ m^2K [113]. Heat transfer coefficient in the present design is improved due to the two main facts: 1) high area to volume ratio of the heat exchanger, and 2) the enhancement related to the manifold-microchannel technology as reported in the literature [15, 26]. As expected, the heat duty and overall heat transfer coefficient increase with increase in hot-side microchannel Reynolds number for the test conditions.

The heat transfer performance results for the subscale unit with varying cold-side microchannel Reynolds number ($Re_{chn,c}$) are shown in Figure 8-24. $Re_{chn,c}$ is defined as:

$$Re_{chn,c} = \frac{D_{chn,c}\dot{m}_{chn,c}}{A_{chn,c}\mu_{cold}} \tag{38}$$

where $A_{chn,c}$ is the cold-side microchannel cross section area ($A_{chn,c}$ = 0.00034 m × 0.00101 m), $D_{chn,c}$ is the cold-side microchannel hydraulic diameter ($D_{chn,c}$ = 0.00051 m), and $\dot{m}_{chn,c}$ is the mass flow rate per microchannel on the cold-side.

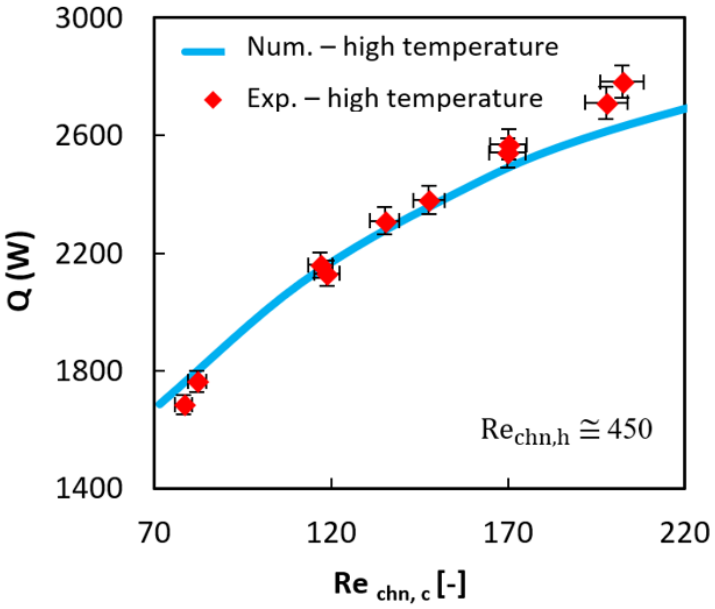

(a)

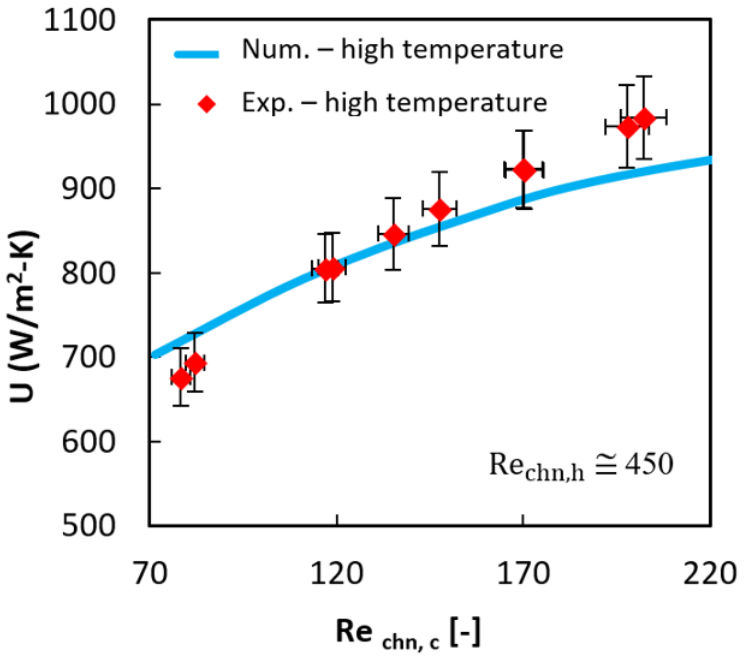

(b)

Figure 8-24: Experimental and numerical results for constant hot-side microchannel Reynolds number ($Re_{chn,h} \cong 450$) and 560 °C temperature difference between hot inlet N_2 and cold inlet air: (a) heat duty (Q) vs. cold-side microchannel Reynolds number ($Re_{chn,c}$); (b) overall heat transfer coefficient (U) vs. cold-side microchannel Reynolds number ($Re_{chn,c}$)

Figure 8-24 (a) shows the heat duty variation with the change in cold-side flow rate for a constant hot-side microchannel Reynolds number of about 450. A maximum of 2780 W heat duty was achieved at cold-side microchannel Reynolds number of 200. The overall heat transfer coefficient of the heat exchanger was in the range of 700 – 1000 W/m^{2}K as shown in Figure 8-24 (b). The graphs also show that heat duty and overall heat transfer coefficient increase with increase in cold-side microchannel Reynolds number. Comparing the trend between Figure 8-23 and Figure 8-24, it shows that cold-side flow rate has more impact on the heat exchanger's thermal

performance. This is due to the fact that the cold-side flow rate is much lower (which is almost 50% of the hot-side flow rate). Therefore, the thermal resistance on the cold-side is higher than the hot-side, and any improvement in cold-side flow rate can positively impact the overall heat transfer performance.

The pressure drop performance of the heat exchanger test section is shown in Figure 8-25. The trend is as expected: pressure drop increases with increased Reynolds number. During the high temperature tests, the hot-side pressure drop reached 4000 Pa at maximum hot-side microchannel Reynolds number of about 450. Maximum cold-side pressure drop was measured as 5200 Pa at maximum cold-side microchannel Reynolds number of about 200. For the adiabatic tests, the hot-side maximum pressure drop was measured as 1410 Pa at maximum hot-side microchannel Reynolds number of about 900. Cold-side maximum pressure drop was measured as 5210 Pa at cold-side microchannel Reynolds number of about 370.

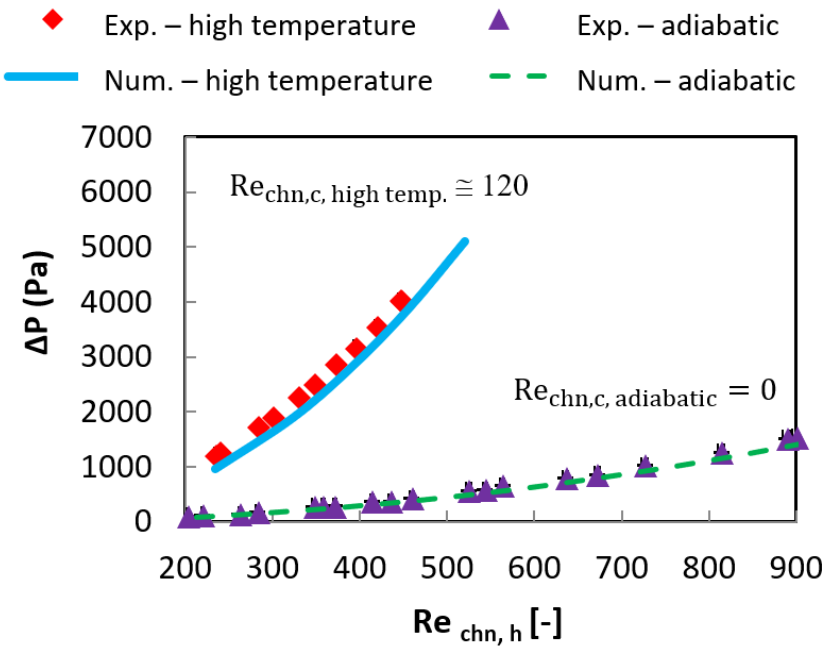

(a)

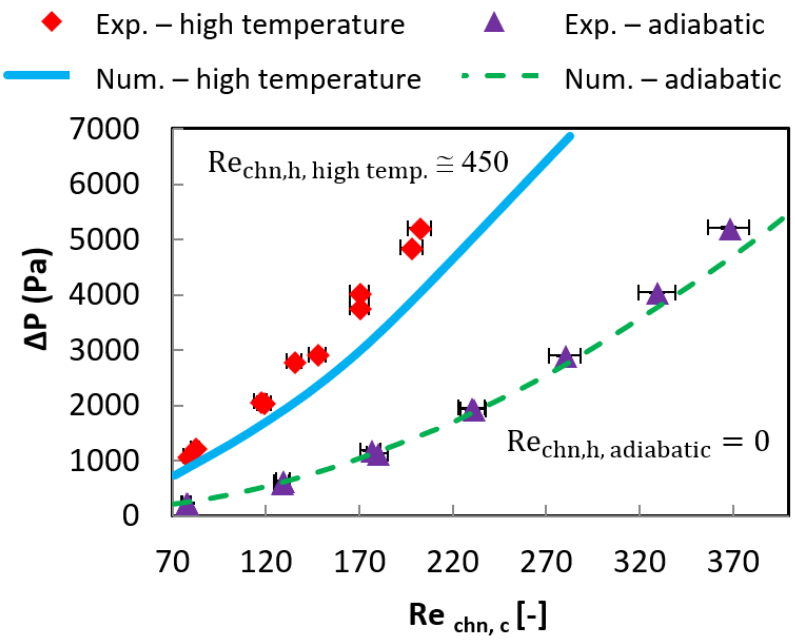

(b)

Figure 8-25: Experimental and numerical results: (a) hot-side pressure drop (ΔP_{hot}) vs. hot-side microchannel Reynolds number ($Re_{chn,h}$); (b) cold-side pressure drop (ΔP_{cold}) vs. cold-side microchannel Reynolds number ($Re_{chn,c}$)

From Figure 8-23 and Figure 8-24, it can be observed that the heat transfer performance results show a decent agreement between the numerical and experimental data. From Figure 8-25, for the high-temperature tests it can be seen that the measured pressure drops are about 10% higher than the numerical predictions on the hot-side, and about 25% higher than the numerical predictions on the cold-side. For the adiabatic tests, the pressure drop measurements are within 5% of the predictions. The deviation observed between the high-temperature tests and adiabatic tests is due to the fact that constant gas properties (calculated at average temperature between inlet and outlet) were assumed in the numerical model used for pressure drop prediction. For the adiabatic tests, since there was no heat transfer involved, the gas

properties did not change during the tests. However, for the high-temperature tests, the gas properties varied along the flow due to the temperature change. The higher deviation observed on the cold-side is due to the temperature difference between cold inlet and outlet, which was about 300°C, while the temperature difference between the hot inlet and outlet was relatively small (~ 100°C).

As shown in Figure 8-26, if the constant air properties at cold inlet temperature (which is the same as the adiabatic test condition) is used in the calculations, the pressure drop prediction on cold side is much lower than the experimental result. If the constant air properties at hot inlet temperature is used, the pressure drop prediction is much higher than the experimental result. In fact, the experimental results fall between two modeling cases: one is that the average value of the cold-side inlet and outlet temperatures is used and another one is that the cold-side outlet temperature is used. From these results, it can be concluded that the most of subscale unit on cold side effectively operates at higher temperatures than the inlet and outlet average temperature. This may not always be the case for other heat exchanger designs since it depends on temperature distribution inside the heat exchanger. However, it seems for this particular subscale unit the deviation observed is due to this temperature effect.

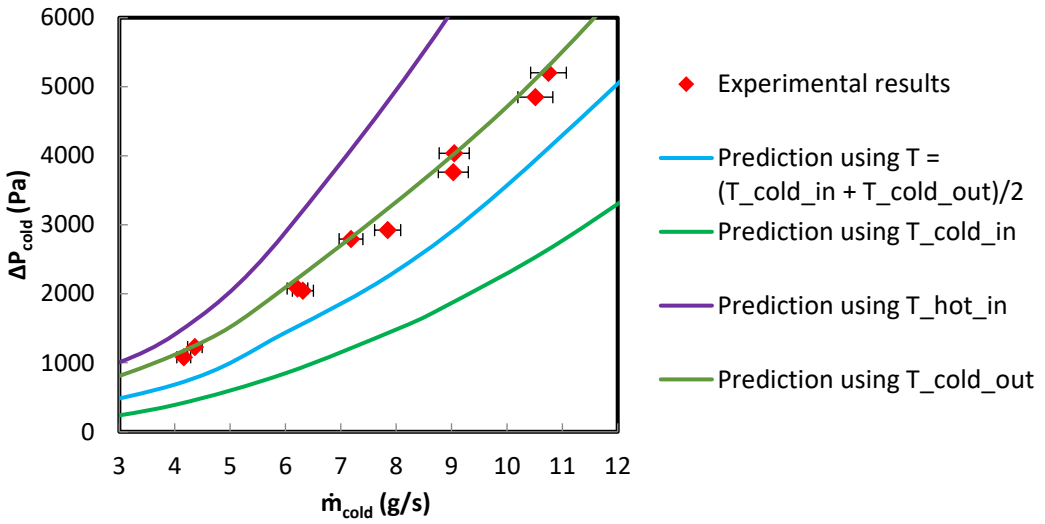

Figure 8-26: Experimental and numerical results: cold-side pressure drop vs cold-side mass flow rate

Considering plate-fin heat exchangers are the most commonly utilized compact high temperature heat exchangers for gas-to-gas heat transfer applications, the experimental results of the additively manufactured manifold-microchannel heat exchanger were compared with plate-fin heat exchangers to assess its superiority. Based on a database provided in Ref. [114] as shown in Table 8-8, the geometries of plate-fin heat exchangers were selected through an optimization using COP of 62 and effectiveness of 60% as the same design point of the subscale unit under the same operating conditions. The COP was evaluated as:

$$COP = \frac{Q}{(\Delta P_{h,core} \times \frac{\dot{m}_{hot}}{\rho_{hot}} + \Delta P_{c,core} \times \frac{\dot{m}_{cold}}{\rho_{cold}})} \quad (39)$$

where $\Delta P_{h,core}$ and $\Delta P_{c,core}$ are the pressure drop of the heat exchanger core on the ho- and cold side, ρ_{hot} and ρ_{cold} are the gas density on the hot and cold sides, $\dot{m}_{hot}$ and $\dot{m}_{cold}$ are the mass flow rates, and Q is the heat duty.

Table 8-8 Key geometrical specifications of plate-fin heat exchanger [114]

Name	Fin pitch (fin/cm)	Plate spacing (cm)
PFHX 1	7.82	0.64
PFHX 2	5.94	1.06
PFHX 3	5.82	0.84
PFHX 4	4.37	0.64

The plate-fin heat exchangers were optimized for a compact size, which was the same to minimize mass (m). The sizing was obtained by fixing the mass flow rates, effectiveness, and COP to match the subscale manifold-microchannel heat exchanger design. The results are presented in the form of heat transfer density (Q/m) versus COP in Figure 8-27. The heat transfer density is defined as the ratio of heat duty (Q) over the heat exchanger core's mass (m). The subscale manifold-microchannel heat exchanger shows improvement of heat transfer density of up to 25% for the same COP compared to the best plate-fin heat exchanger design.

Figure 8-28 shows the comparison among all heat exchangers in terms of the overall heat transfer coefficient. Note that for the conventional plate-fin heat exchangers, the base thickness ($2H_{base}$) is assumed to be 0.3 mm whereas for the manifold-microchannel heat exchanger the fabricated base thickness was 0.5 mm. The result again demonstrates the superiority of manifold-microchannel heat exchanger in terms of thermal performance over the conventional plate-fin heat exchangers.

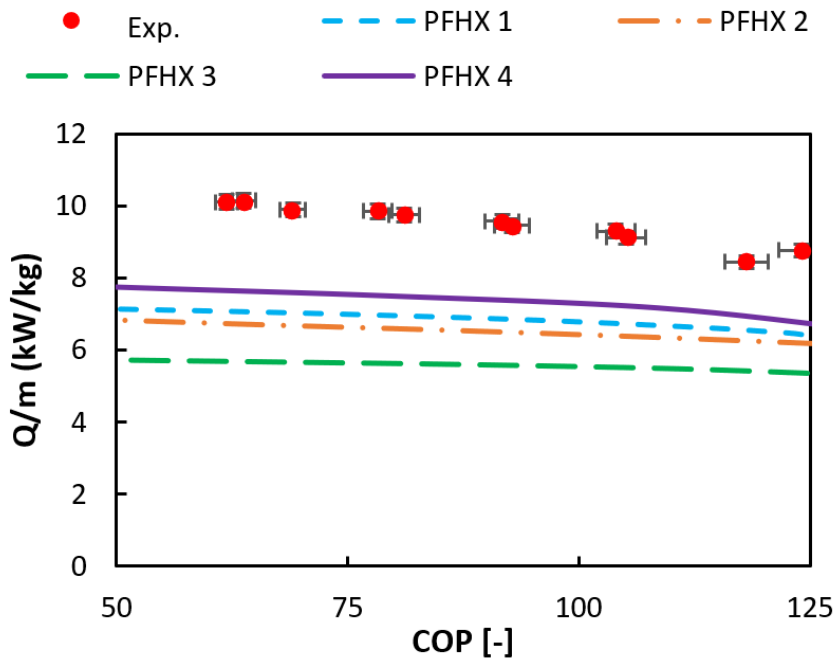

Figure 8-27: Performance comparison between manifold-microchannel heat exchanger with conventional plate-fin heat exchangers

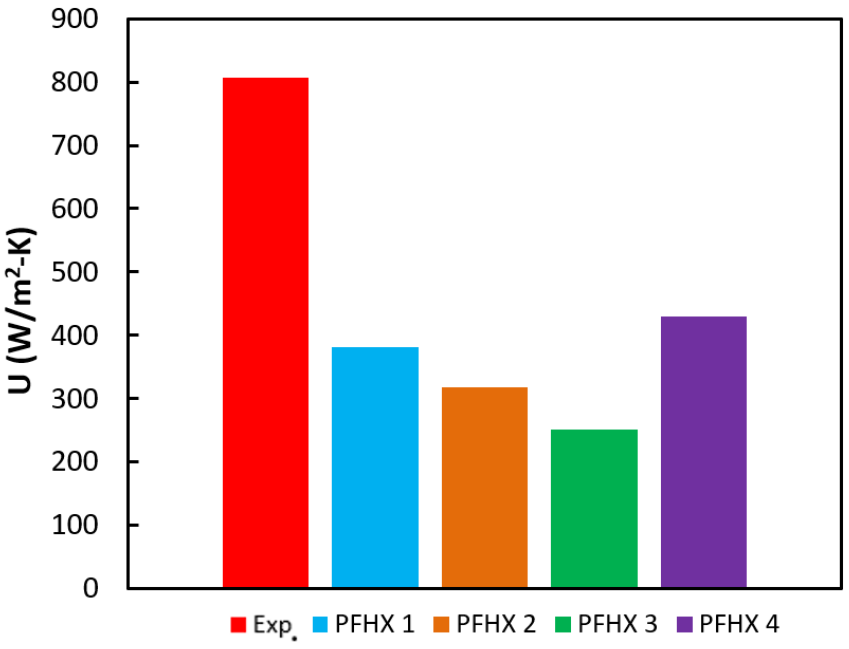

Figure 8-28: Comparison of overall heat transfer coefficient (U) of manifold-microchannel heat exchanger and selected conventional plate-fin heat exchangers

8.9. Summary

In summary, the fabrication of the metal headers and the test section (including headers, flanges, and the subscale unit) demonstrated the feasibility of welding additively manufactured and conventionally machined Inconel 718 parts. A high-temperature experimental setup was built so that high-temperature experiments (up to 650°C with maximum system pressure of 655 kPa) for various high temperature heat exchangers can be conducted. This chapter also demonstrates that the additively manufactured Inconel 718 high temperature gas-to-gas subscale heat exchanger was successfully tested at 600°C with ~ 450 kPa inlet pressure. A maximum heat duty of 2.78 kW and a heat transfer density close to 10 kW/kg was achieved with cold-side inlet temperature of 38°C. The decent agreement between the experimental and the numerical results demonstrates the validity of the updated numerical analysis models used for heat transfer and pressure drop predictions. The performance comparison shows that additive manufacturing can be used to achieve the compact and light-weight high temperature heat exchangers, and benefit the applications where space and weight are constrained.

Chapter 9: Advanced Manifold-microchannel Heat Exchanger

9.1. Introduction

Considering the successful fabrication of the subscale unit through additive manufacturing and the promising experimental results compared to the numerical predictions, this chapter discusses an advanced gas-to-gas cross-flow manifold-microchannel heat exchanger design which was created based on the new design requirement given by the sponsor. More constraints regarding the advanced heat exchanger's overall size were added during the design stage. And a medium-scale unit design was created, which has a heat duty of 20 kW at the design point compared to the 2-kW heat duty of the subscale unit, to further evaluate the maximum building size and fabrication limits of the DMLS process.

9.2. Design Requirement for Advanced Manifold-microchannel Heat Exchanger

Since the fabrication of the subscale unit demonstrated the feasibility of the selected additive manufacturing approach (DMLS), and the experimental results showed that the 3-D printed heat exchanger can be leak-free and withstand required pressure at high temperatures, an advanced design with new operating and physical specifications was requested. As shown in Table 9-1 and Table 9-2, the advanced heat exchanger design must have a size which is equal to or smaller than the given size of the baseline heat exchanger with the same heat duty of 417 kW.

Table 9-1 Physical specifications for full-scale advanced heat exchanger

Overall Volume	≤ 1161 in^3 (0.019 m^3)
Hot-flow Length	≤ 10.5 in (0.27 m)
Cold-flow Length	≤ 9.1 in (0.23 m)
No-flow Length	≤ 12.15 in (0.31 m)
Weight	≤ 82 lb (37.2 kg)
Material	Inconel 625

Table 9-2 Operating specifications for full-scale advanced heat exchanger

Parameter		**Unit**	**Nominal Condition**
Hot Side	Flow	lb/min (kg/s)	212.2 (1.604)
	Temperature	°F (°C)	908 (487)
	Pressure	psia (kPa)	49.2 (339.2)
	Pressure Drop	psid (kPa)	5.43 (37.4)
	Effectiveness	%	52.9
Cold Side	Flow	lb/min (kg/s)	229.9 (1.738)
	Temperature	°F (°C)	74 (23)
	Pressure	psia (kPa)	9.52 (65.6)
	Pressure Drop	psid (kPa)	1.9 (13.1)
	Effectiveness	%	50.9

9.3. Advanced Manifold-microchannel Heat Exchanger Design

A single objective optimization was performed to find the minimum weight of the advanced manifold-microchannel heat exchanger for the given physical and operating conditions listed in the previous section. As shown in Table 9-3, the optimal design achieved a 22% weight reduction with a 5% increase of the no-flow length and a 2% increase of the pressure drop on the cold side.

Table 9-3 Optimized advanced manifold-microchannel heat exchanger design

Q	416 kW (– 0.3%)
L_{hot}	0.267 m
L_{cold}	0.231 m
$L_{no-flow}$	0.323 m (+ 4.8%)
N_{layer}	54
$Mass$	28.9 kg (– 22.2%)
$Volume$	0.0199 m^3 (+ 4.8%)
$dP_{hot\ full}$	37.6 kPa (+ 0.5%)
$dP_{cold\ full}$	13.4 kPa (+ 2.3%)

Compared to the first additively manufactured gas-to-gas cross-flow manifold-microchannel heat exchanger discussed before, the advanced design includes a much shorter manifold height on the hot side, a thinner microchannel base, thinner microchannel fins on both sides, and most importantly, it has vertical fins / manifold walls on both sides. As shown in Table 9-4, the advanced design's hot-side manifold height for each layer is 0.95 mm, the microchannel base thickness is reduced to 0.15 mm (which means the separating sheet thickness is 0.3 mm), and the fin thickness on both sides is ~0.15 mm.

Table 9-4 Comparison between 3-D printed heat exchanger and advanced design

		3-D Printed HX	Advanced Design
Cold side	H_{chn}	1.010 mm	0.876 mm
	t_{fin}	0.165 mm	0.149 mm
	W_{chn}	0.340 mm	0.220 mm
	$H_{chn,base}$	0.250 mm	0.150 mm
	$W_{mnd-\text{chn}}$	4.440 mm	17.657 mm
	H_{mnd}	5.250 mm	3.300 mm
	W_{in}	3.490 mm	3.531 mm
	$Wall_{mnd}$	0.350 mm	0.300 mm
	$H_{mnd,base}$	0.300 mm	0.150 mm
	N_{chn} per in	50	69
	N_{mnd}	11	14
	N_{chn}	138	626
	N_{pass}	1	1
	H_{mnd}/H_{chn}	5.2	3.8
Hot side	H_{chn}	1.280 mm	0.259 mm
	t_{fin}	0.180 mm	0.153 mm
	W_{chn}	0.390 mm	0.310 mm
	$H_{chn,base}$	0.250 mm	0.150 mm
	$W_{mnd-\text{chn}}$	6.100 mm	12.252 mm
	H_{mnd}	4.810 mm	0.950 mm
	W_{in}	2.480 mm	0.196 mm
	$Wall_{mnd}$	0.500 mm	0.300 mm
	$H_{mnd,base}$	0.300 mm	0.150 mm
	N_{chn} per in	32	55
	N_{chn}	72	577
	N_{mnd}	10	18
	N_{pass}	1	1
	H_{mnd}/H_{chn}	3.8	3.7

9.4. Medium-scale Unit Design

Considering the current DMLS printer in the market does not have the capability to print the full-size advanced manifold-microchannel heat exchanger, a medium-scale unit design was created by scaling down the full-size design. During the scaling-down process, channel height (H_{chn}), fin thickness (t_{fin}), channel width (W_{chn}), base thickness ($H_{chn,base}$), and mass flow rate per microchannel were kept the same for the microchannel surface as the full-size design. For the manifold scaling, width of manifold channel ($W_{mnd-\mathrm{chn}}$), manifold wall thickness ($Wall_{mnd}$), inlet width to microchannel (W_{in}), manifold base thickness ($H_{mnd,base}$), and pressure drop in the manifold per manifold channel length (which is the same as flow length) were the same as full-size design. As shown in Table 9-5, the medium-scale unit's manifold height and number of microchannels on both sides were reduced compared to the full-size design.

Table 9-5 Comparison between advanced full-size and medium-scale design

	Cold side		**Hot side**	
	Full-size	**Medium-Scale**	**Full-size**	**Medium-Scale**
H_{chn}	0.876 mm	0.876 mm	0.259 mm	0.259 mm
t_{fin}	0.149 mm	0.149 mm	0.172 mm	0.172 mm
W_{chn}	0.220 mm	0.220 mm	0.291 mm	0.291 mm
$H_{chn,base}$	0.175 mm	0.175 mm	0.175 mm	0.175 mm
$W_{mnd-\mathrm{chn}}$	17.657 mm	17.657 mm	12.252 mm	12.252 mm
H_{mnd}	3.300 mm	1.890 mm	0.950 mm	0.458 mm
$Wall_{mnd}$	0.300 mm	0.300 mm	0.300 mm	0.300 mm
W_{in}	3.531 mm	3.531 mm	0.250 mm	0.250 mm
$H_{mnd,base}$	0.150 mm	0.150 mm	0.150 mm	0.150 mm
N_{chn}	626	204	577	155

However, compared to the 3-D printed subscale unit, the medium-scale design is still ~ 4 times as much as the overall size and 10 times as much as the heat duty as shown in Table 9-6. It can also be noticed from Figure 9-1 that medium-scale design's no-flow length is ~ 4 times the subscale design, and much more manifold-microchannel layers are included in the medium-scale design due to the shorter manifold height on both sides.

Table 9-6 Comparison between subscale unit and medium-scale design

	3D Printed Subscale Core	**Medium-scale Core Design**
L_{hot}	0.059 m	0.072 m
L_{cold}	0.070 m	0.075 m
$L_{no-flow}$	0.027 m	0.114 m
N_{layer}	2	28
Q	2.0 kW *	20.3 kW
$Fin\ type$	Cold vertical / Hot inclined	Cold vertical / Hot vertical

Note: Heat duty (Q) of 3-D printed subscale IN718 heat exchanger core is based on previous operating specifications.

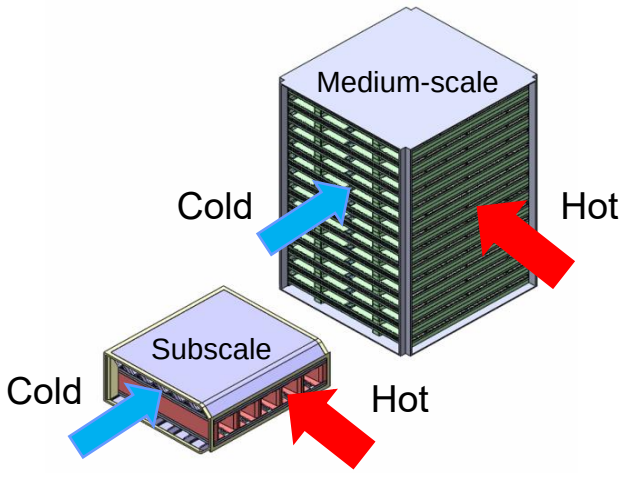

Figure 9-1: Subscale unit design vs. medium-scale unit design

Based on the lesson learnt from the welding of the test section discussed in the previous chapter, the medium-scale unit's welding interface frame was created such that the welding edge has a thickness of 3 mm, and headers on both sides have separate welding edges (by extending the welding interface on all four sides as shown in Figure 9-2) to avoid any potential leakage directly from hot-side header to cold-side header.

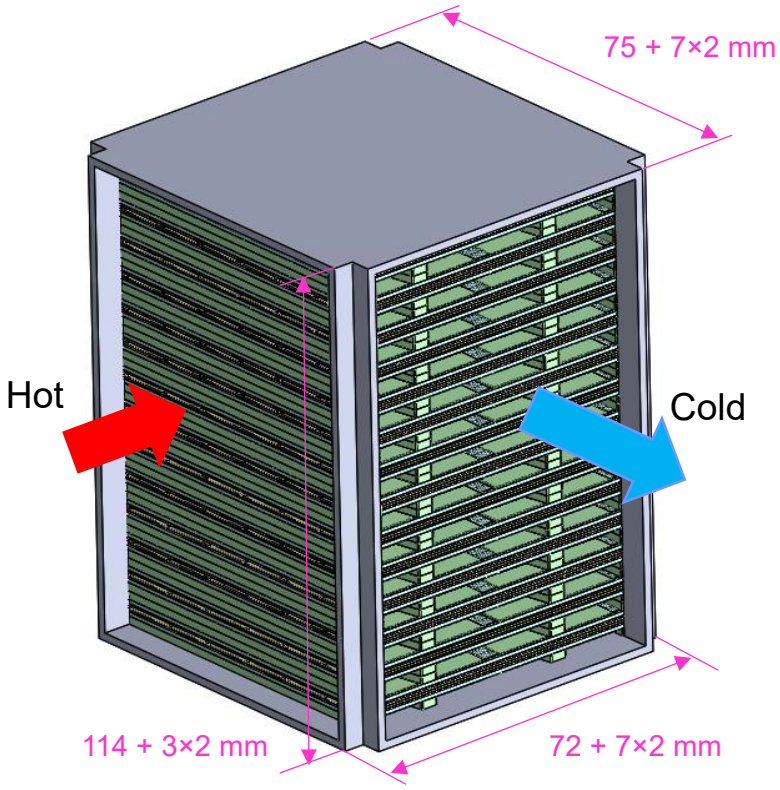

Figure 9-2: Medium-scale design with the welding interface frame (marked in gray)

Because the medium-scale design has vertical microchannel fins and vertical manifold walls on both sides, unlike the 3-D printed subscale unit, a 45-degree printing orientation has to be applied to the medium-scale design so that the cross-flow microchannel fins can still be self-supported during the sintering process as shown in Figure 9-3 (a). However, considering the tapered manifold channel

design, when the medium-scale unit is printing in a 45-degree orientation, half of the manifold walls will raise an overhang concern since they will be printing in an angle less than 45 degrees as shown in Figure 9-3 (b).

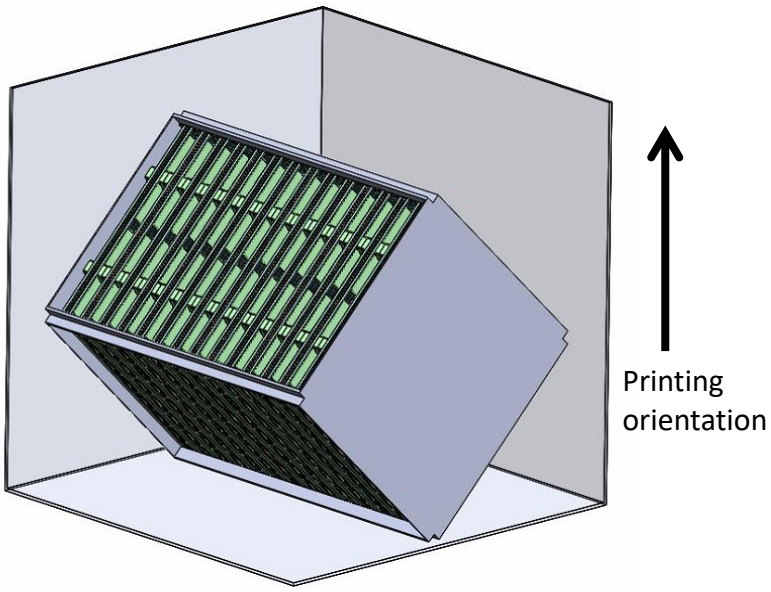

(a)

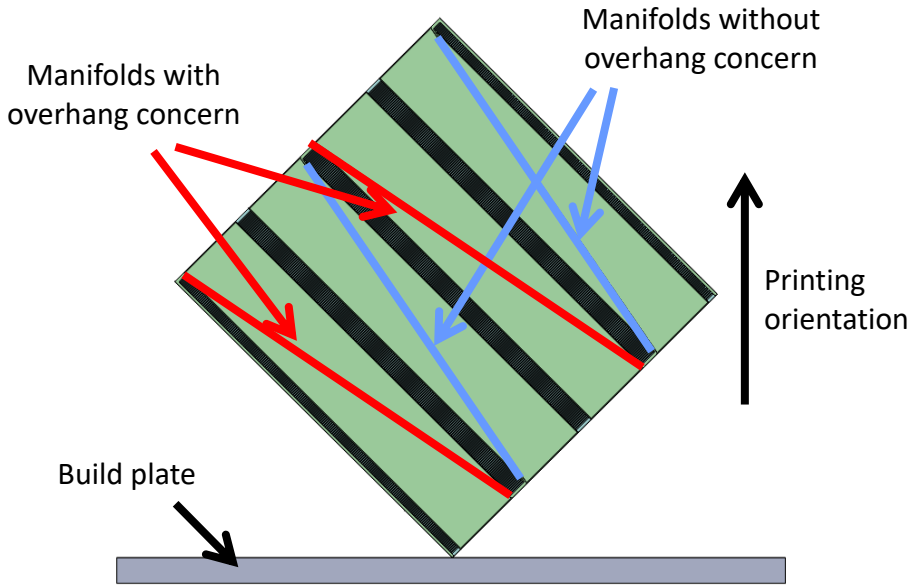

(b)

Figure 9-3: Preferred printing orientation for the medium-scale design (a); tapered manifold channel's overhang concern with 45-degree printing orientation (b)

9.5. Summary

In summary, an advanced manifold-microchannel heat exchanger design was created based on the new design specification which has a required minimum heat transfer density (Q/m) of 11 kW/kg compared to the previously required one of 6.7 kW/kg. To comply with the maximum build envelop size of currently available DMLS printers in the market, a medium-scale unit which has the same microchannel geometrical dimensions was created. By comparing to the 3-D printed subscale heat exchanger, the medium-scale design is 4 times as much as the overall size and 10 times as much as the heat duty at design point. However, since the advanced cross-flow design has vertical microchannels fins on both sides for the purpose of avoiding additional pressure drop included by the inclined fins, the medium-scale unit has to be fabricated with a 45-degree printing orientation.

Chapter 10: Conclusions and Proposed Future Work

10.1. Conclusions

In this dissertation, an additive manufacturing technique (DMLS) was used to fabricate a high-temperature gas-to-gas cross-flow manifold-microchannel heat exchanger. An advanced design optimization scheme was applied to meet the heat transfer density (Q/m) requirement for pre-cooling applications on the aircraft. Although this study focused on an aerospace pre-cooling heat exchanger application, the results can also be of significance to other industries that rely on compact gas-to-gas applications. These include air-cooled condensers (heat pump, refrigeration), air-cooled heat sinks (electronic cooling), air-to-air heat exchangers (economizers), and most importantly, gas-to-gas high-temperature heat exchangers (recuperators for gas turbine power generation).

As the first additively manufactured high-temperature manifold-microchannel heat exchanger, the heat exchanger designed and fabricated for this study was composed of manifold-microchannels on both hot and cold sides in a cross-flow configuration. An optimization utilizing the modified hybrid method was performed to obtain the initial design, which had a minimum weight and met all the design requirements as well as the manufacturing constraints of the DMLS process. For comparison purposes, single-objective optimizations were also performed based on different manufacturing approaches including photo-chemical etching, laser micro-machining, and diffusion bonding for the same performance constraints. The results showed that the 3-D printed heat exchanger offered the highest heat transfer density

(Q/m) compared to other manufacturing approaches (40% higher than photo-chemical etching, and 8% higher than laser micro-machining). This approach allowed the heat exchanger to be fabricated from Inconel 718, which is a very tough material for conventional machining process, as a single piece. The selected approach (DMLS) also eliminated the time-consuming assembly process, which may cause unwanted additional pressure drops across the microchannel section due to clogging. The full-size heat exchanger design was scaled down to a subscale unit that could be fabricated by a 3-D metal printer currently on the market and experimentally tested under the existing constraints of the laboratory at University of Maryland.

Several test print coupons were first fabricated through DMLS using Inconel 718 to evaluate the quality of the 3-D metal printed parts. Different small-feature sizes such as microchannel fin thickness and manifold wall thickness were incorporated in the coupon design. By measuring the fabricated small features under a digital microscope, it was found that the minimum printed vertical microchannel fin thickness was 165 μm (± 7 μm), and the minimum printed inclined fin was 180 μm (± 12 μm) thick. For all other features whose size was greater than 300 μm, the fabricated dimensions were within 7% of the design values. Since the 3-D printed metal piece may have had some porosity issues due to the voids generated during the powder sintering process, two pressure containment test coupons were fabricated to identify the minimum microchannel base thickness (which is the same as separating sheet thickness) needed to prevent leakage from the high-pressure (64.7 psia) to low-pressure (14.7 psia) side. The pressure containment test results

showed a small leakage on the coupon with microchannel base thickness of 0.3 mm at 34.7 psia, and the coupon with 0.5 mm thick microchannel base could be leak-free at the required pressure of 64.7 psia. Another water-based pressure containment test also showed that the leak-free coupon could withstand up to 3000 psig pressure without any deformation.

Based on the knowledge gained from the test print coupons, the subscale cross-flow manifold-microchannel heat exchanger design was modified according to the updated manufacturing constraints and successfully fabricated out of Inconel 718 through the DMLS additive manufacturing technique. The entire unit was 3-D printed within 36 hours, which was much less than the quoted lead time of any other conventional manufacturing techniques. A detailed inspection of the fabricated subscale heat exchanger as well as the small sectional coupon (which was 3-D printed simultaneously in the same build as the subscale heat exchanger for measuring the internal feature size) demonstrated fabrication fidelity within 14% of design values. Except fin thickness on both sides, all other dimensions were within 5%. Since tapered manifold channels were incorporated in the subscale unit's design, to achieve more accurate performance predictions, single-manifold-multi-microchannels (SMMM) models were created to replace the single manifold-microchannel models initially used in the modified hybrid method. The CFD simulation results of the SMMM model also showed that a more uniform flow distribution could be obtained with the tapered manifold channels compared to the straight channels. The flow maldistribution was ~ 12% with the tapered manifold channel and ~25% with the straight manifold channel.

The 3-D printed subscale heat exchanger was experimentally tested under both low-temperature and high-temperature conditions to characterize its performance. The low-temperature test results showed a decent agreement for the heat transfer performance between the experimental data and the numerical prediction using the SMMM model. However, due to the non-uniform flow at the subscale unit's cold-side inlet induced by the low-temperature header design, the measured pressure drop on the cold side was ~ 40 – 50% higher than the numerical prediction. Since the subscale manifold-microchannel heat exchanger was designed for high-temperature applications, a high-temperature experimental setup was built from scratch to characterize the heat exchanger's performance at high temperatures. To address the non-uniform flow induced by the low-temperature header, flow deflectors were added into the high-temperature metal headers and flow simulations using both Solidworks and Fluent were performed to ensure the flow maldistribution from the metal header was less than 8%. Since the full CFD model included both headers and the heat exchanger core, a more accurate prediction including pressure drop across the inlet/outlet headers and pressure drop across the heat exchanger core could be obtained.

A maximum heat duty of 2.78 kW and a heat transfer density close to 10 kW/kg was achieved with cold-side inlet temperature of 38°C during the high-temperature experiments. It was observed that the heat transfer performance results again showed a decent agreement between the numerical and experimental data. Since the high-temperature experiments included two test conditions, for the high-temperature tests the measured pressure drops were about 10% higher than the numerical predictions

on the hot side, and about 25% higher than the numerical predictions on the cold side. For the adiabatic tests (no heat transfer involved), the pressure drop measurements on both sides were within 5% of the predictions. The deviation observed between the high-temperature tests and adiabatic tests was due to the fact that constant gas properties (calculated at average temperature between inlet and outlet) were assumed in the full CFD model used for pressure drop prediction. For the adiabatic tests, the gas properties did not change during the tests, as there was no heat transfer involved. However, for the high-temperature tests, the gas properties varied along the flow due to the temperature change. The higher deviation observed on the cold side was due to the temperature difference between cold inlet and outlet, which was about 300°C, while the temperature difference between the hot inlet and outlet was relatively small (~ 100°C). The performance of the subscale heat exchanger was also compared to selected conventional plate-fin heat exchangers (which are the most common compact high temperature heat exchangers for gas-to-gas applications) under the same operating conditions. The subscale manifold-microchannel heat exchanger showed improvement of heat transfer density of up to 25% for the same COP compared to the best plate-fin heat exchanger design.

Considering the good agreement between experimental and numerical results, the method used to predict the additively manufactured manifold-microchannel heat exchanger was verified, and the process of the method is summarized as following:

1. Obtain optimal heat exchanger design based on the operating specifications and manufacturing constraints through the optimization using modified hybrid method with single manifold-microchannel models.

2. Create single-manifold-multi-microchannels (SMMM) models to obtain more accurate performance predictions if tapered manifold channel and/or inclined microchannel fins are utilized in the final heat exchanger design.

3. Design headers (with flow deflectors if needed) using Solidworks flow simulation as the preliminary approach to obtain the minimum flow maldistribution among the manifold channels at the inlet and outlet of the manifold-microchannel heat exchanger.

4. Create simplified single manifold-porous-medium models in which the microchannel section is replaced with porous medium to reduce computational time, and calibrate the porous medium parameters by matching mass flow rate vs. pressure drop based on the predictions obtained from the single-manifold-multi-microchannels (SMMM) models.

5. Conduct Fluent flow simulations including inlet/outlet headers and heat exchanger core (with the simplified single manifold-porous-medium models) to obtain more accurate flow distribution among inlet/outlet manifold channels and pressure drops (including $\Delta P_{header,\ inlet}$, $\Delta P_{header,\ outlet}$, and ΔP_{core}).

Given the successful fabrication of the subscale heat exchanger through additive manufacturing and the promising experimental results compared to the numerical predictions, an advanced high-temperature gas-to-gas manifold-microchannel heat exchanger was designed based on the newly identified physical and operating specifications. As a more compact design, the advanced heat exchanger's manifold height on both sides was significantly reduced, and vertical fins were incorporated

on both sides of the cross-flow microchannel surface to improve the overall performance. To further evaluate the maximum building size of currently available DMLS printers on the market, a medium-scale design which was 4 times larger than the overall size of the subscale heat exchanger was created and incorporated the recommended 45-degree printing orientation.

10.2. Proposed Future Work

Several directions for future work in the areas of numerical modeling of manifold-microchannel heat exchangers, additive manufacturing enhancement, and other aspects associated with continuity of the project are proposed in this section.

10.2.1. Numerical modeling

The single-manifold-multi-microchannels (SMMM) model discussed in this dissertation did not consider the change of gas properties due to different temperatures along the flow path inside the manifold-microchannel heat exchanger. As mentioned in chapter 8, the deviation of the pressure drop prediction from the experimental results on the cold side shows that when the temperature difference between inlet and outlet is large, the pressure drop may be greatly underestimated with improper gas properties. To improve the SMMM model, a temperature-dependent flow simulation should be studied, and the gas properties as a function of local temperature should be implemented in the SMMM model.

During the design stage of the high-temperature manifold-microchannel heat exchanger, the heat exchanger's material properties were considered at a constant

temperature of 600°C to ensure that the heat exchanger structure would be strong enough to withstand the required system pressure under high-temperature conditions. However, as the temperature inside the heat exchanger may change significantly from 600°C to 40°C, some structures inside the heat exchanger could be designed with a much smaller thickness to further reduce the heat exchanger's weight. Such design can only be created if a thermal-mechanical model is applied or developed.

Currently, both the single manifold-microchannel model and the single-manifold-multi-microchannels model used in the modified hybrid method to predict the manifold-microchannel heat exchanger's performance are based on CFD simulations running with a commercially available software (ANSYS Fluent). If a universal meta-model that includes the most possible flow characteristics of different manifold-microchannel heat exchanger geometries could be created, the computational time of the optimization process for a manifold-microchannel heat exchanger design could be shortened considerably. However, such universal meta-model may need thousands of different manifold-microchannel heat exchangers as the initial samplings, considering there are at least six variables on each side of the manifold-microchannel heat exchanger: microchannel height (H_{chn}), microchannel fin thickness (t_{fin}), microchannel width (W_{chn}), width of manifold channel ($W_{mnd-chn}$), height of manifold channel (H_{mnd}), and inlet width to microchannel (W_{in}).

10.2.2. Additive manufacturing

In the field of additive manufacturing, more work is needed to improve the fabrication quality of DMLS. To obtain the highest heat transfer performance from the advanced manifold-microchannel design, the microchannel fin thickness on both sides should be ~ 150 μm. But since the minimum vertical fin thickness of the fabricated subscale heat exchanger was 165 μm, either a different DMLS printer (the one used to fabricate the subscale heat exchanger is built by Concept Laser, but there are other 3-D metal printers built by EOS or 3D Systems) or different printing settings are needed to achieve a cross-flow microchannel surface with fin thickness of 100 μm or even smaller in some designs.

Because most of a manifold-microchannel heat exchanger's weight is from the microchannel base, or separating sheet, a thinner microchannel base would not only improve the heat transfer by decreasing the thermal resistance between hot and cold streams, but also significantly reduce the mass of the heat exchanger. However, to prevent leakage directly from the high-pressure to low-pressure side, the printed minimum microchannel base was 0.5 mm. This minimum base thickness could be reduced to 0.3 mm if the porosity issue of the DMLS process could be resolved by either using smaller size metal powder or adjusting the laser power during the sintering process. Considerable trial-and-error testing will be needed to achieve a thinner leak-free separating sheet for all heat exchanger designs that plan to use additive manufacturing as the fabrication approach.

Even though many studies have shown that the manifold-microchannel technique can significantly improve heat transfer compared to conventional heat exchanger designs, and this dissertation has demonstrated that a gas-to-gas cross-flow manifold-microchannel heat exchanger can be successfully fabricated using additive manufacturing, there is no DMLS printer on the market that can print a full-scale manifold-microchannel heat exchanger with a minimum overall size of $127 \times 127 \times 127$ mm^3. The overall size of the medium-scale design, which was obtained by scaling down the full-scale advanced heat exchanger, was $86 \times 89 \times 120$ mm^3. This was the maximum build size among the DMLS printers that could print a minimum feature size of 150 μm. When a larger build size is desired, a major limitation of current 3-D metal printers is that the minimum feature size will be about 500 μm due to the fixed location of the laser head. Since industrial-size heat exchangers require both large build size and small feature size, current 3-D metal printers will need to be modified, such as by incorporating an adjustable laser header, if they are to be used to fabricate such heat exchangers.

10.2.3. Project Continuity

For continuity of the project, the medium-scale advanced manifold-microchannel heat exchanger should be fabricated. Based on the knowledge gained from the subscale unit's fabrication, new test print coupons should be 3-D printed using the recommended 45-degree orientation to evaluate the fabrication quality. If the tapered manifold wall cannot be fabricated due to the overhang issue discussed in the previous chapter, either the tapered angle needs to be modified as shown in Figure 10-1 so that a smaller tapered angle can be used by reducing the inlet width

of manifold channel ($W_{mnd-chn-in}$), or a straight manifold channel which may cause a high flow maldistribution needs to be re-incorporated.

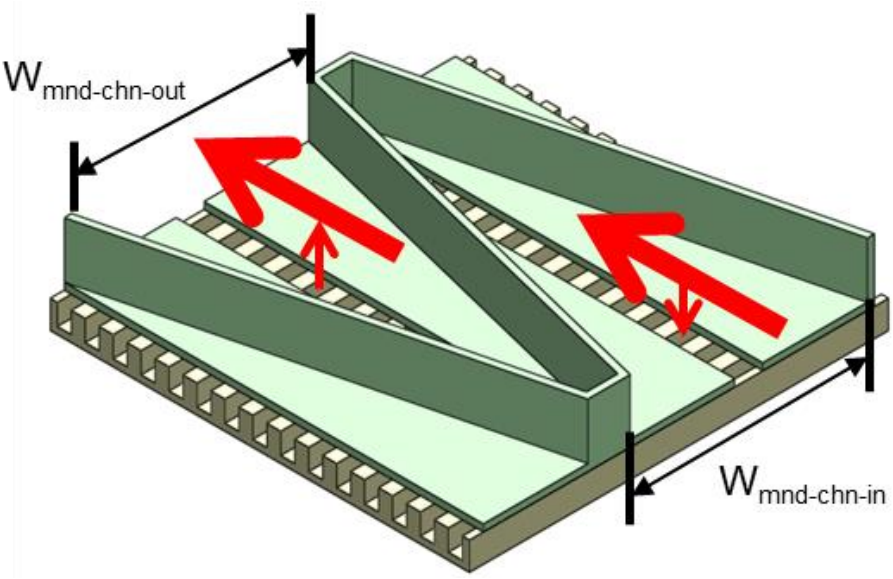

(a)

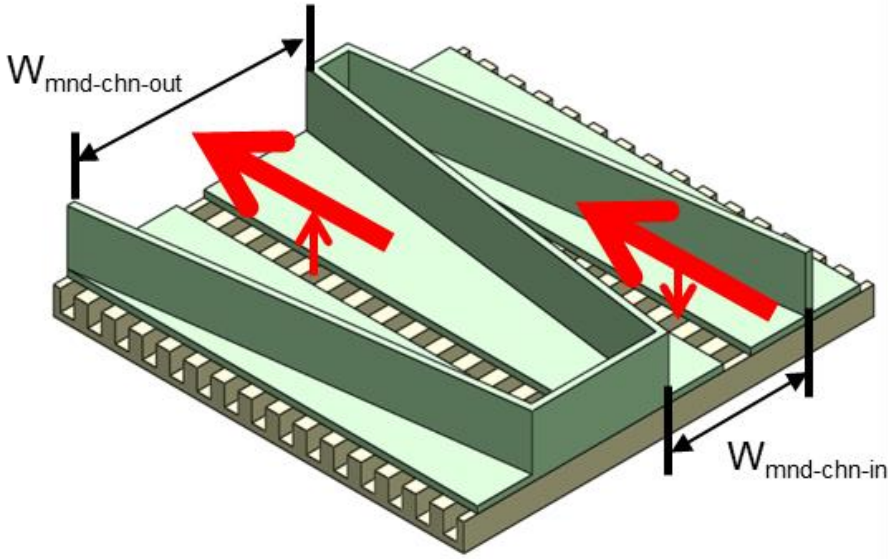

(b)

Figure 10-1: Tapered manifold channel design: large tapered angle (a); small tapered angle (b)

Based on the evaluation of the new test print coupons, the medium-scale design should be updated accordingly. The optimization can be re-run if considerable changes are identified regarding the manufacturing constraints such as minimum printable microchannel fin thickness (or minimum microchannel width which can help to reduce fin thickness). If a new numerical model which can consider the effect of different manifold channel's tapered angles is developed, a new advanced manifold-microchannel design that can meet all the new design requirements (such as shorter manifold height so that no-flow length is also equal to or less than the required value) will be possible.

Considering some high temperature heat exchangers need to operate under both high-temperature and high-pressure (≥600°C & ≥80 bars) conditions, a thermal-mechanical model, which can predict the structural stress conditions at different locations and temperatures inside a heat exchanger, should be developed so that more reliable manifold-microchannel heat exchanger designs can be obtained. And for certain case when the operating temperature is more than 1000°C, using ceramics as the material of fabrication will be more demanding with the thermal-mechanical model.

Appendices

Pre-test Procedures for High Temperature Experimental Setup

Instruments

- Validyne differential pressure transmitter
    - Hot/cold side
        - Range: 0 – 5.5 kPa
          (this can be adjusted by replacing the diaphragm)
        - Uncertainty: +/- 0.25% FS

- Sensotec absolute pressure transducer
    - Hot side
        - Range: 0 – 200 psia
        - Uncertainty: +/- 0.10% FS

- Endress Hausser Coriolis flow meter
    - Hot side (flow meter 1, meter size DN 15)
        - Range: 0 – 105 g/s
        - Uncertainty: measured error less than 1% (when flow rate ≥ 6 g/s)

    - Cold side option 1 (flow meter 2, meter size DN 50)
        - Range: 0 – 250 g/s
        - Uncertainty: measured error less than 5% (when flow rate ≥ 20 g/s)

    - Cold side option 2 (flow meter 2, meter size DN 25)
        - Range: 0 – 150 g/s
        - Uncertainty: measured error less than 3% (when flow rate ≥ 4 g/s)

- Omega high-temperature-glass K type thermocouple
    - Hot/cold side
        - Range: 0 – 704°C
        - Uncertainty: standard limits of error (above 0 °C) is 2.2°C or 0.75% of measurement

Experimental Instrumentation Check

To ensure measurements are as accurate as the instruments can have, all instruments will be checked and calibrated individually before the tests

- Pressure transmitter/transducer calibration
    - Differential pressure transmitter's output voltage reading will be calibrated based on water column level reading or special differential pressure calibration tool
    - Absolute pressure transducer's output voltage reading will be calibrated based on N_2 gas tank's pressure gauge reading

- Coriolis flow meter
    - Two Coriolis flow meters will be tested in series with a fixed flowrate blower, both readings should be the same as the blower's rated flowrate. Otherwise, the flow meters will be sent back to manufacturer for re-calibration

- High temperature thermocouple
    - High temperature K type thermocouple will be tested in ice bath to check if temperature reading is 0°C

Setup Preparation

To ensure no leakage issue will be found during the tests (which may either cause inaccurate measurement or damage the setup), all individual components and the assembled test setup will be checked before the tests

- Individual Component Check
    - Electric heater
        - Pressure containment test will be conducted on the electric heater's body, no bubble (leak point) should be noticed when the body is covered with soap

    - Tube-in-tube heat exchanger (heat exchanger 1)
        - Pressure containment test will be conducted, no bubble (leak point) should be noticed on both outer and inner tubes when the heat exchanger is submerged underwater

    - Mixing chambers
        - Pressure containment tests will be conducted on all four mixing chambers (hot/cold side inlet/outlet), no bubble (leak point) should be noticed when the mixing chambers are submerged underwater

    - Test Section
        - Pressure containment test will be conducted on the test section (both hot and cold side), no bubble (leak point) should be noticed when the test section was submerged underwater

- Setup Assembly Check
    - Assembled setup
        - Pressure containment test will be conducted on the assembled setup's hot side, no bubble (leak point) should be noticed along fittings (NPT fittings, compression fittings, flange/clamp connections) and pipes (welded flexible metal hose) when they are covered with soap

- Heat loss check
    - At the beginning of test, only hot side will be running
    - Once desired mass flow rate is reached, wait until flow meter reading is stable
    - Turn on the heater to heat the hot side gas to desired temperature, wait for 20 – 30 minutes until both inlet and outlet temperature is stable
    - Take thermal images of the test section and inlet/outlet mixing chambers to locate any existing hot spot
    - If big hot spot is found along the insulated area, and calculated heat loss is more than acceptable range (5% of desired capacity), turn off hot side
    - Wait until hot side is completely cooled, check the hot spot area, and add more insulation layers
    - Repeat previous steps until calculated heat loss is within acceptable range

Experiment Tests

- Adiabatic test
    - Before high temperature tests, in order to quickly assess the quality of the heat exchanger (mainly to check whether microchannels are clogged), only one side (hot or cold) will be running at room temperature (electric heater will be off), and only pressure drop data will compared to numerical prediction
- Standard high temperature test procedures
    - Turn on the chiller and ensure chilling water is flowing through the tube-in-tube heat exchanger
    - Turn on cold side blower, check cold side flow rate and pressure drop readings
    - Pressurize hot side to desired system pressure, turn on hot side compressor, check hot side flow rate and pressure drop readings

- When hot side mass flow rate is more than 6 g/s, turn on the electric heater
- Heat up hot side gas flow to desired temperature while ensure the exhaust gas is cooled down to room temperature through tube-in-tube heat exchanger
- Wait until both test section's inlet and outlet temperature are stable, then record the measurements (including test section's hot/cold side inlet/outlet temperatures, hot/cold side pressure drops, hot/cold side mass flow rates, and hot side system pressure)
- Change flow rate on hot and/or cold side, adjust the electric heater to control test section hot side inlet temperature, wait until both test section's inlet and outlet temperature are stable
- Repeat the process based on the pre-determined experiment data sets
- After all date sets are collected, turn off electric heater while keep both hot and cold side running with room temperature gas flow to cool down the setup
- Turn off hot side compressor when all hot side temperature are stable as room temperature, then turn off cold side blower
- Turn off the chiller, and depressurize hot side to atmosphere pressure

- Heat balance check
  - During the test, if calculated heat balance is more than acceptable range (10%), take thermal images to check if any hot spot can be found along test section and mixing chambers
  - If no hot spot is found, turn off heater
  - Check flow meter to see if mass flow rate reading is consistent and correct based on previously calibrated data
  - When the test loop is cooled down (less than 50°C), use soap to check if there is any leakage along fittings and pipes

- If no issue can be found on flow meter, and no leakage can be identified along fittings and pipes, turn off hot side and take out the thermocouples
- Test the thermocouples in ice bath and boiling water to check if any issue with thermocouples' reading
- If thermocouples' issue is resolved, turn on hot side, and re-check if heat balance is within acceptable range

High Temperature Setup Operation Checklist

- **Please read this checklist carefully**
- **Always request a second person when running the high temperature test**
- **Be aware if you see or smell anything that looks like burning/melting, turn off the heater immediately by turning off the control panel**

- **Before test**
  - Ensure all thermocouples, pressure transducers, and flowmeters are connected to the data acquisition system
  - Ensure all power plugs (including dP transducers, temperature switch, scroll compressor, blower, flowmeters, and data acquisition system) are safely connected
  - Turn on the chiller and ensure chilling water is flowing through the pipe
  - Set the cooling temperature on the chiller to 10-15°C (push the bottom while changing cooling temperature set point)
  - Open the valve on the N2 gas cylinder, ensure there are enough N2 gas for the following test (A full cylinder with 2500 psi reading can last about 10 hours)
  - Open the hot side charging valve (as shown below) to start filling the hot side loop with N2 gas

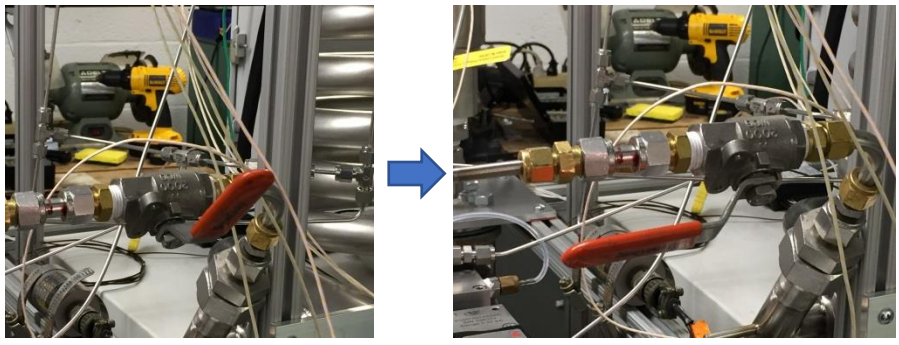

  - Start the data acquisition system, ensure all the readings make sense for non-operation conditions
  - Ensure the bypass valve for hot side dP transducer is open, then slowly increase the hot side system pressure through the pressure regulator, and

ensure hot side dP reading does not exceed the max reading of the dP transducer

- Turn on the 3-phase power switch for electric heater's control panel (at this point, be careful when standing around the test setup, do not touch any 3-phase power cable)

- **During test**
  - Turn on the blower by push the start bottom (the green one), slowly increase the flow rate by increasing the frequency showing on the variable frequency controller's monitor
  - Check the mass flow rate based on the cold side flowmeter's reading, and ensure the cold side dP reading does not exceed the max reading of the dP transducer
  - Close the bypass valve for hot side dP transducer
  - Turn on the scroll compressor by push the start bottom (the green one), slowly increase the flow rate by increasing the frequency showing on the variable frequency controller's monitor
  - Check the mass flow rate based on the hot side flowmeter's reading, and ensure the hot side dP reading does not exceed the max reading of the dP transducer
  - When hot side mass flow rate is more than 6 g/s, turn on the electric heater's control panel
    - Note: the heater has a minimum mass flow rate requirement of 5.5 g/s
  - When hot side and cold side mass flow rate reach the desired point, change the heater's control panel set point to 70°C, then start the heater by click "heat on/off"
  - Slowing increase the heating set point to desired temperature (e.g. wait 2-3 min then increase the set point by 50-80°C each time, and at the beginning, it may take 20-30 min for all the temperature measurement to be stable)
    - Note: remember to check the mass flow rate reading since temperature change may cause mass flow rate change as well

- For the heater's control panel, in the setup mode, turn on the "auto tune" function if a stable exhaust temperature (± 1-2°C) is desired (for more information regarding how to set up the heater's control panel and the alarm system, please read through the heater's control panel operation manual)

- **After test**
  - Turn off the electric heater by click "heat on/off"
  - When the process temperature showing on the heater's control panel monitor is less than 40°C, turn off the heater's control panel
  - Turn off the 3-phase power switch for electric heater's control panel
  - Slowly decrease the mass flow rate on cold side to about 3 g/s, and slowly decrease the mass flow rate on hot side to 6 g/s
  - Let the system cool down for 10-15 min
  - Open the bypass valve for hot side dP transducer
  - Close the valve on the N2 gas cylinder
    - Note: when hot side system pressure is reducing, the hot side mass flow rate is reducing as well, no need to increase it or keep it constant at 6 g/s anymore
  - When the system pressure reduced to atmosphere pressure (when the pressure gauge of the pressure regulator shows 0 psi), release the pressure regulator by rotate the regulator valve through counter-clock direction
  - Close the hot side charging valve
  - After ensuring all the temperature measurement reading is less than 30°C, turn off the chiller, wait for 5 min, close the yellow valve
  - Decrease the frequency on both scroll compressor and blower's variable frequency controller to 0 Hz, then click the red button
  - Disconnect the power plugs (including dP transducers, temperature switch, scroll compressor, blower, flowmeters, and data acquisition system)

References

[1] W. A. Whittenberger, G. W. Brunson, and J. H. Becker, "High-temperature heat exchanger," U.S. Patent US8047272, 2011.

[2] D. Stevenson, D. L. Vrable, and R. J. Watts, "Development of an intermediate temperature carbon-carbon heat exchanger for aircraft applications," *presented at the 44th International SAMPE Symposium*, 1999.

[3] C. F. McDonald and D. G. Wilson, "The utilization of recuperated and regenerated engine cycles for high-efficiency gas turbines in the 21st century," *Applied Thermal Engineering*, vol. 16, no. 8-9, pp. 635-653, 1996.

[4] J. K. Min, J. H. Jeong, M. Y. Ha, and K. S. Kim, "High temperature heat exchanger studies for applications to gas turbines," *Heat and Mass Transfer*, vol. 46, no. 2, pp. 175-186, 2009.

[5] X. Liu, Y. Deng, K. Zhang, M. Xu, Y. Xu, and C. Su, "Experiments and simulations on heat exchangers in thermoelectric generator for automotive application," *Applied Thermal Engineering*, vol. 71, no. 1, pp. 364-370, 2014.

[6] T. Wang, Y. Zhang, J. Zhang, G. Shu, and Z. Peng, "Analysis of recoverable exhaust energy from a light-duty gasoline engine," *Applied Thermal Engineering*, vol. 53, no. 2, pp. 414-419, 2013.

[7] D. Aquaro and M. Pieve, "High temperature heat exchangers for power plants: Performance of advanced metallic recuperators," *Applied Thermal Engineering*, vol. 27, no. 2-3, pp. 389-400, 2007.

[8] R. E. Mizia, "Next generation nuclear plant intermediate heat exchanger acquisition strategy," Idaho National Laboratory (INL), Idaho Falls, ID (United States), 2008.

[9] K. Hada, I. Nishiguchi, Y. Muto, and H. Tsuji, "Developments of metallic materials and a high-temperature structural design code for the HTTR," *Nuclear engineering and design*, vol. 132, no. 1, pp. 1-11, 1991.

[10] L. Chordia, M. A. Portnoff, and E. Green, "High temperature heat exchanger design and fabrication for systems with large pressure differentials," Thar Energy, LLC, Pittsburgh, PA (United States), 2017.

[11] Q. Li, G. Flamant, X. Yuan, P. Neveu, and L. Luo, "Compact heat exchangers: A review and future applications for a new generation of high temperature solar receivers," *Renewable and Sustainable Energy Reviews*, vol. 15, no. 9, pp. 4855-4875, 2011.

[12] X. Zhang, H. Keramati, M. Arie, F. Singer, R. Tiwari, A. Shooshtari, and M. Ohadi, "Recent developments in high temperature heat exchangers: a review," *Frontiers in Heat and Mass Transfer*, vol. 11, no. 18, 2018.

[13] G. M. Harpole and J. E. Eninger, "Micro-channel heat exchanger optimization," in *Semiconductor Thermal Measurement and Management Symposium, 1991. SEMI-THERM VII. Proceedings., Seventh Annual IEEE*, 1991, pp. 59-63: IEEE.

[14] M. Arie, A. Shooshtari, S. Dessiatoun, E. Al-Hajri, and M. Ohadi, "Numerical modeling and thermal optimization of a single-phase flow

manifold-microchannel plate heat exchanger," *International Journal of Heat and Mass Transfer,* vol. 81, pp. 478-489, 2015.

[15] M. A. Arie, A. Shooshtari, S. Dessiatoun, and M. Ohadi, "Thermal optimization of an air-cooling heat exchanger utilizing manifold-microchannels," in *Thermal and Thermomechanical Phenomena in Electronic Systems (ITherm), 2014 IEEE Intersociety Conference on*, 2014, pp. 807-815: IEEE.

[16] M. A. Arie, A. H. Shooshtari, and M. M. Ohadi, "Experimental characterization of an additively manufactured heat exchanger for dry cooling of power plants," *Applied Thermal Engineering,* vol. 129, pp. 187-198, 2018.

[17] V. Jha, S. Dessiatoun, M. Ohadi, A. Shooshtari, and E. Al-Hajri, "High performance micro-grooved evaporative heat transfer surface for low grade waste heat recovery applications," in *ASME 2011 Pacific Rim Technical Conference and Exhibition on Packaging and Integration of Electronic and Photonic Systems*, 2011, pp. 277-283: American Society of Mechanical Engineers.

[18] V. Jha, S. Dessiatoun, A. Shooshtari, E. S. Al-Hajri, and M. M. Ohadi, "Experimental characterization of a nickel alloy-based manifold-microgroove evaporator," *Heat Transfer Engineering*, vol. 36, no. 1, pp. 33-42, 2015.

[19] D. Boyea, A. Shooshtari, S. V. Dessiatoun, and M. M. Ohadi, "Heat transfer and pressure drop characteristics of a liquid cooled manifold-microgroove condenser," in *ASME 2013 Heat Transfer Summer Conference collocated with the ASME 2013 7th International Conference on Energy Sustainability and the ASME 2013 11th International Conference on Fuel Cell Science, Engineering and Technology*, 2013: American Society of Mechanical Engineers.

[20] M. Ohadi, K. Choo, S. Dessiatoun, and E. Cetegen, *Next generation microchannel heat exchangers*. Springer, 2013.

[21] E. Kermani, S. Dessiatoun, A. Shooshtari, and M. M. Ohadi, "Experimental investigation of heat transfer performance of a manifold microchannel heat sink for cooling of concentrated solar cells," in *Electronic Components and Technology Conference, 2009. ECTC 2009. 59th*, 2009, pp. 453-459: IEEE.

[22] E. Cetegen, "Force fed microchannel high heat flux cooling utilizing microgrooved surfaces," Ph.D thesis, University of Maryland, College Park, 2010.

[23] M. Arie, A. Shooshtari, S. Dessiatoun, M. Ohadi, and E. Al Hajri, "Simulation and thermal optimization of a manifold microchannel flat plate heat exchanger," in *ASME 2012 International Mechanical Engineering Congress and Exposition*, 2012, pp. 209-220: American Society of Mechanical Engineers.

[24] L. Boteler, N. Jankowski, P. McCluskey, and B. Morgan, "Numerical investigation and sensitivity analysis of manifold microchannel coolers," *International Journal of Heat and Mass Transfer,* vol. 55, no. 25-26, pp. 7698-7708, 2012.

[25] M. A. Arie, A. Shooshtari, and M. Ohadi, "Air side enhancement of heat transfer in an additively manufactured 1 kW heat exchanger for dry cooling applications," in *Thermal and Thermomechanical Phenomena in Electronic Systems (ITherm), 2017 16th IEEE Intersociety Conference on*, 2017, pp. 1-8: IEEE.

[26] R. S. Andhare, A. Shooshtari, S. V. Dessiatoun, and M. M. Ohadi, "Heat transfer and pressure drop characteristics of a flat plate manifold microchannel heat exchanger in counter flow configuration," *Applied Thermal Engineering*, vol. 96, pp. 178-189, 2016.

[27] D. L. Bourell, J. J. Beaman, M. C. Leu, and D. W. Rosen, "A brief history of additive manufacturing and the 2009 roadmap for additive manufacturing: looking back and looking ahead," *Proceedings of RapidTech*, pp. 24-25, 2009.

[28] SPI Lasers. *Metal Additive Manufacturing*. Available: http://www.spilasers.com/whitepapers/metal-additive-manufacturing [Accessed Jan 2, 2018].

[29] C. Hutter, D. Büchi, V. Zuber, and P. Rudolf von Rohr, "Heat transfer in metal foams and designed porous media," *Chemical Engineering Science*, vol. 66, no. 17, pp. 3806-3814, 2011.

[30] M. Wong, I. Owen, C. J. Sutcliffe, and A. Puri, "Convective heat transfer and pressure losses across novel heat sinks fabricated by Selective Laser Melting," *International Journal of Heat and Mass Transfer*, vol. 52, no. 1, pp. 281-288, 2009.

[31] S. Tsopanos, C. Sutcliffe, and I. Owen, "The manufacture of micro cross-flow heat exchangers by selective laser melting," in *Enhanced, Compact and Ultra-Compact Heat Exchangers: Science, Engineering and Technology*, 2005: ECI Symposium Series.

[32] S. M. Thompson, Z. S. Aspin, N. Shamsaei, A. Elwany, and L. Bian, "Additive manufacturing of heat exchangers: a case study on a multi-layered Ti–6Al–4V oscillating heat pipe," *Additive Manufacturing*, vol. 8, pp. 163-174, 2015.

[33] M. Arie, A. Shooshtari, S. Dessiatoun, and M. Ohadi, "Performance characterization of an additively manufactured titanium (Ti64) heat exchanger for an air-water cooling application," in *ASME 2016 Heat Transfer Summer Conference collocated with the ASME 2016 Fluids Engineering Division Summer Meeting and the ASME 2016 14th International Conference on Nanochannels, Microchannels, and Minichannels*, 2016: American Society of Mechanical Engineers.

[34] W. D. Gerstler and D. Erno, "Introduction of an additively manufactured multi-furcating heat exchanger," in *Thermal and Thermomechanical Phenomena in Electronic Systems (ITherm), 2017 16th IEEE Intersociety Conference on*, 2017, pp. 624-633: IEEE.

[35] M. A. Arie, A. H. Shooshtari, R. Tiwari, S. V. Dessiatoun, M. M. Ohadi, and J. M. Pearce, "Experimental characterization of heat transfer in an additively manufactured polymer heat exchanger," *Applied Thermal Engineering*, vol. 113, pp. 575-584, 2017.

[36] L. Leslie. (2016). *Metal Additive Manufacturing Enables Lean, Green Heat Exchanger*. Available: http://www.makepartsfast.com/metal-additive-manufacturing-enables-lean-green-heat-exchanger/ [Accessed March 31, 2018].

[37] Q. Wang, X. Han, A. Sommers, Y. Park, C. T'Joen, and A. Jacobi, "A review on application of carbonaceous materials and carbon matrix composites for heat exchangers and heat sinks," *International Journal of refrigeration*, vol. 35, no. 1, pp. 7-26, 2012.

[38] Y. Mori, A. E. Sheĭndlin, and N. H. Afgan, *High temperature heat exchangers* (Proceedings of the International Centre for Heat and Mass Transfer; 22.). Washington, D.C.: Hemisphere Pub. Corp., 1986.

[39] L. M. Crosbie and D. Chapin, "Hydrogen production by nuclear heat," *GENES4/ANP2003*, Kyoto, Japan, 2003.

[40] C. Mansilla, J. Sigurvinsson, A. Bontemps, A. Maréchal, and F. Werkoff, "Heat management for hydrogen production by high temperature steam electrolysis," *Energy*, vol. 32, no. 4, pp. 423-430, 2007.

[41] L. Magistri, A. Traverso, A. Massardo, and R. Shah, "Heat exchangers for fuel cell and hybrid system applications," *Journal of fuel cell science and technology*, vol. 3, no. 2, pp. 111-118, 2006.

[42] G. Musgrove, R. LePierres, and Nash J., "Heat exchangers for supercritical CO2 power cycle applications," in *The 4th International Symposium on Supercritical CO2 Power Cycles*, Pittsburgh Pennsylvania, 2014.

[43] I. Johnson, W. T. Choate, and A. Davidson, "Waste heat recovery. Technology and opportunities in US industry," BCS, Inc., Laurel, MD (United States), 2008.

[44] K. Brun, P. Friedman, and R. Dennis, *Fundamentals and applications of supercritical carbon dioxide (sCO2) based power cycles*. Woodhead Publishing, 2017.

[45] C. F. McDonald, "The role of the ceramic heat exchanger in energy and resource conservation," *Journal of Engineering for Power*, vol. 102, no. 2, pp. 303-315, 1980.

[46] Marlin Steel. (2016). *4 Inconel Machining Tips You Need to Know*. Available: https://www.marlinwire.com/blog/inconel-machining-tips [Accessed March 31, 2018].

[47] Continental Steel & Tube Company. (2015). *Considerations when Machining Nickel Alloys*. Available: https://continentalsteel.com/blog/considerations-when-machining-nickel-alloys/ [Accessed March 31, 2018].

[48] M. M. Ohadi and S. G. Buckley, "High temperature heat exchangers and microscale combustion systems: applications to thermal system miniaturization," *Experimental Thermal and Fluid Science*, vol. 25, no. 5, pp. 207-217, 2001.

[49] C. F. McDonald, "Low-cost compact primary surface recuperator concept for microturbines," *Applied Thermal Engineering*, vol. 20, no. 5, pp. 471-497, 2000.

[50] X. Zhang, M. Arie, D. Deisenroth, A. Shooshtari, S. Dessiatoun, and M. Ohadi, "Impact of additive manufacturing on performance enhancement of heat exchangers: a case study on an air-to-air heat exchanger for high temperature applications," in *IX Minsk International Seminar on Heat Pipes, Heat Pumps, Refrigerators, Power Sources, Minsk, Belarus*, 2015.

[51] M. A. Arie, A. H. Shooshtari, V. V. Rao, S. V. Dessiatoun, and M. M. Ohadi, "Air-side heat transfer enhancement utilizing design optimization and an additive manufacturing technique," *Journal of Heat Transfer*, vol. 139, no. 3, 2017.

[52] S. Kandlikar, S. Garimella, D. Li, S. Colin, and M. R. King, *Heat transfer and fluid flow in minichannels and microchannels*. elsevier, 2005.

[53] E. Utriainen and B. Sundén, "Evaluation of the cross corrugated and some other candidate heat transfer surfaces for microturbine recuperators," *Journal of Engineering for Gas Turbines and Power*, vol. 124, no. 3, pp. 550-560, 2002.

[54] J. Stasiek, "Experimental studies of heat transfer and fluid flow across corrugated-undulated heat exchanger surfaces," *International Journal of Heat and Mass Transfer*, vol. 41, no. 6-7, pp. 899-914, 1998.

[55] S. Foerster and M. Kleemann, "Compact metallic and ceramic recuperators for gas turbines," in *ASME 1978 International Gas Turbine Conference and Products Show*, 1978: American Society of Mechanical Engineers.

[56] J.-W. Seo, C. Cho, S. Lee, and Y.-D. Choi, "Thermal characteristics of a primary surface heat exchanger with corrugated channels," *Entropy*, vol. 18, no. 12, 2015.

[57] R. Shah and D. Sekulic, "Heat exchangers," in *Handbook of Heat Transfer*, Warren M. Rohsenow, James P. Hartnett, and Y. I. Cho, Eds. 3rd ed. New York: McGraw-Hill, 1998.

[58] E. Lara-Curzio, P. J. Maziasz, B. A. Pint, M. Stewart, D. Hamrin, N. Lipovich, and D. DeMore, "Test facility for screening and evaluating candidate materials for advanced microturbine recuperators," *presented at the Volume 1: Turbo Expo 2002*, 2002.

[59] A. Franco and C. Casarosa, "Thermoeconomic evaluation of the feasibility of highly efficient combined cycle power plants," *Energy*, vol. 29, no. 12-15, pp. 1963-1982, 2004.

[60] G. Xiao, T. Yang, H. Liu, D. Ni, M. L. Ferrari, M. Li, Z. Luo, K. Cen, and M. Ni, "Recuperators for micro gas turbines: a review," *Applied Energy*, vol. 197, pp. 83-99, 2017.

[61] K. Takase, H. Furukawa, and K. Nakano, "A preliminary study of an inter-cooled and recuperative microgasturbine below 300 kW," in *ASME Turbo Expo 2002: Power for Land, Sea, and Air*, 2002, pp. 1009-1016: American Society of Mechanical Engineers.

[62] J. Kesseli, T. Wolf, J. Nash, and S. Freedman, "Micro, industrial, and advanced gas turbines employing recuperators," in *ASME Turbo Expo 2003, collocated with the 2003 International Joint Power Generation Conference*, 2003, pp. 789-794: American Society of Mechanical Engineers.

[63] C. M. Parker K, "Development in plate-fin heat exchangers," *ASME Publication HTD,* vol. 10, pp. 171–179, 1979.
[64] C. F. McDonald, "Compact buffer zone plate-fin IHX—the key component for high-temperature nuclear process heat realization with advanced MHR," *Applied Thermal Engineering,* vol. 16, no. 1, pp. 3-32, 1996.
[65] G. Lagerström and M. Xie, "High performance and cost effective recuperator for micro-gas turbines," no. 36061, pp. 1003-1007, 2002.
[66] A. Muley and B. Sundén, "Advances in recuperator technology for gas turbine systems," in *ASME 2003 International Mechanical Engineering Congress and Exposition*, 2003, pp. 161-169: American Society of Mechanical Engineers.
[67] M. A. Wilson, K. Recknagle, and K. Brooks, "Design and development of a low-cost, high temperature silicon carbide micro-channel recuperator," in *ASME Turbo Expo 2005: Power for Land, Sea, and Air*, 2005, pp. 1029-1034: American Society of Mechanical Engineers.
[68] H. Antoine and L. Prieels, "The ACTE spiral recuperator for gas turbine engines," in *ASME Turbo Expo 2002: Power for Land, Sea, and Air*, 2002, pp. 1025-1031: American Society of Mechanical Engineers.
[69] J. I. Oswald, D. A. Dawson, and L. A. Clawley, "A new durable gas turbine recuperator," in *ASME 1999 International Gas Turbine and Aeroengine Congress and Exhibition*, 1999: American Society of Mechanical Engineers.
[70] R. A. Proeschel, "Proe 90™ recuperator for microturbine applications," in *ASME Turbo Expo 2002: Power for Land, Sea, and Air*, 2002, pp. 1033-1044: American Society of Mechanical Engineers.
[71] H. Schönenborn, E. Ebert, B. Simon, and P. Storm, "Thermomechanical design of a heat exchanger for a recuperative aero engine," in *ASME Turbo Expo 2004: Power for Land, Sea, and Air*, 2004, pp. 187-193: American Society of Mechanical Engineers.
[72] R. Cook, R. Exner, and L. Graham, "Post-service examination of a 10 MW helium-helium heat exchanger and comparison with long term behaviour in laboratory tests," *High temperature metallic materials for gas-cooled reactors,* p. 129, 1989.
[73] M. E. Collings, B. A. Dockter, D. R. Hajicek, A. K. Henderson, J. P. Hurley, P. L. Kleven, and G. F. Weber, "High-temperature heat exchanger testing in a pilot-scale slagging furnace system,"; University of North Dakota (US), 1999, Available: http://www.osti.gov/scitech/servlets/purl/824978.
[74] M. Anheden, "Analysis of gas turbine systems for sustainable energy conversion," Ph.D thesis, Trita-KET, Kemiteknik, Stockholm, 2000.
[75] K. A. Al-attab and Z. A. Zainal, "Performance of high-temperature heat exchangers in biomass fuel powered externally fired gas turbine systems," *Renewable Energy,* vol. 35, no. 5, pp. 913-920, 2010.
[76] I. Martinez. *Aircraft Environmental Control*. Available: http://webserver.dmt.upm.es/~WoSdoro/tc3/Aircraft%20ECS.pdf [Accessed March 31, 2018].

[77] Bombardier Inc., "System and method for operating a precooler in an aircraft," 2012. Available: https://patents.justia.com/patent/9624831.

[78] H. Tsuji, *High temperature air combustion : from energy conservation to pollution reduction* (Environmental and energy engineering series; Environmental and energy engineering series.). Boca Raton, FL :: CRC Press, 2003.

[79] S. A. David, J. A. Siefert, J. N. DuPont, and J. P. Shingledecker, "Weldability and weld performance of candidate nickel base superalloys for advanced ultrasupercritical fossil power plants part I: fundamentals.," *Science and Technology of Welding and Joining*, vol. 20, no. 7, pp. 532-552., 2015.

[80] M. A. Arie, "Air side heat transfer enhancement in heat exchangers utilizing innovative designs and the additive manufacturing technique," Ph.D thesis, Univerisity of Maryland, College Park, 2016.

[81] S. K. Mylavarapu, X. Sun, R. N. Christensen, R. R. Unocic, R. E. Glosup, and M. W. Patterson, "Fabrication and design aspects of high-temperature compact diffusion bonded heat exchangers," *Nuclear Engineering and Design*, vol. 249, pp. 49-56, 2012.

[82] Heatric. *Typical characteristics of diffusion-bonded heat exchangers*. Available: https://www.heatric.com/typical_characteristics_of_PCHEs.html [Accessed March 31, 2018].

[83] Heatric. *The exceptional performance of Heatric PCHE heat exchangers*. Available: https://www.heatric.com/heat_exchanger_performance.html [Accessed March 31, 2018].

[84] E. Cetegen, "Force fed microchannel high heat flux cooling utilizing microgrooved surface," Ph.D thesis, University of Maryland, College Park, 2010.

[85] D. Copeland, M. Behnia, and W. Nakayama, "Manifold microchannel heat sinks: isothermal analysis," *IEEE Transactions on Components, Packaging, and Manufacturing Technology – Part A*, vol. 20, no. 2, pp. 96-102, 1997.

[86] S. T. Poh and E. Y. K. Ng, "Investigative study of manifold microchannel heat sinks for electronic cooling design," *Journal of Electronics Manufacturing*, vol. 9, no. 2, pp. 155-166, 1999.

[87] S. T. Poh and E. Y. K. Ng, "Heat transfer and flow issues in manifold microchannel heat sinks: a CFD approach," *presented at the 2nd Electronics Packaging Technology Conference*, Singapore, 1998.

[88] Y. H. Kim, W. C. Chun, J. T. Kim, B. C. Pak, and B. J. Baek, "Forced air cooling by using manifold microchannel heat sinks," *Journal of Mechanical Science and Technology*, vol. 12, no. 4, pp. 709-718, 1998.

[89] J. H. Ryu, D. H. Choi, and S. J. Kim, "Three-dimensional numerical optimization of a manifold microchannel heat sink," *International Journal of Heat andMass Transfer*, vol. 46, no. 9, pp. 1553-1562, 2003.

[90] Y. Wang and G. F. Ding, "Numerical analysis of heat transfer in a manifold microchannel heat sink with high efficient copper heat spreader," *Microsystem Technologies*, vol. 14, no. 3, pp. 389-395, 2008.

[91] W. Escher, T. Brunschwiler, B. Michel, and D. Poulikakos, "Experimental investigation of an ultrathin manifold microchannel heat sink for liquid-cooled chips," *Journal of Heat Transfer,* vol. 132, 2010.
[92] L. M. Boteler, "Microfabrication and analysis of manifold microchannel coolers for power electronics," Ph.D thesis, University of Maryland, College Park, 2011.
[93] L. Boteler, N. Jankowski, P. McCluskey, and B. Morgan, "Numerical investigation and sensitivity analysis of manifold microchannel coolers," *International Journal of Heat and Mass Transfer,* vol. 55, no. 25, pp. 7698-7708, 2012.
[94] R. Mandel, S. Dessiatoun, P. McCluskey., and M. Ohadi, "Embedded two-phase cooling of high flux electronics via micro-enabled surface and fluid delivery system (FEEDS)," *presented at the Proceedings of the ASME 2015 International Technical Conference and Exhibition on Packaging and Integration of Electronic and Photonic Microsystems*, San Francisco, California, USA, 2015.
[95] A. Lohner, "Laser sintering ushers in new route to PM parts," *Metal Powder Report (MPR),* vol. 52, no. 2, pp. 24-30, 1997.
[96] ProtoLabs. (2018). *Design Guidelines: Direct Metal Laser Sintering*. Available: https://www.protolabs.com/services/3d-printing/direct-metal-laser-sintering/design-guidelines/ [Accessed September 20, 2018].
[97] A. Carter, Stratasys Ltd., private communication ed, 2014.
[98] 3D Systems. (2018). *Direct Metal Printing*. Available: https://www.3dsystems.com/on-demand-manufacturing/direct-metal-printing/materials [Accessed Septermber 20, 2018].
[99] M. Eesa and G. Marriott. *Photochemical Etching of Heat Exchanger Plates*.Available: http://www.heatexdesign.com/_resources/assets/attachment/full/0/3017205.pdf [Accessed March 31, 2018].
[100] Potomac-laser. (2018). *Laser Micromachining Metals*. Available: http://www.potomac-laser.com/services/core/laser-micromachining [Accessed September 20, 2018].
[101] N. Muhammad, B. D. Rogers, and L. Li, "Understanding the behaviour of pulsed laser dry and wet micromachining processes by multi-phase smoothed particle hydrodynamics (SPH) modelling," *Journal of Physics D: Applied Physics,* vol. 46, 2013.
[102] M. G. Nicholas, *Joining processes. In: Introduction to Brazing and Diffusion Bonding*. Kluwer Academic, 1998.
[103] K. Kitazono, K. Susumu, and K. Yuki, "Mechanical properties of titanium particles dispersed magnesium matrix composite produced through accumulative diffusion bonding process," *Materials transactions* vol. 52, no. 2, pp. 155-158, 2011.
[104] V. Aute, O. Abdelaziz, S. Azarm, and R. Radermacher, "Cross-validation Based Single Response Adaptive Design of Experiments," *presented at the 12th AIAA/ISSMO Multidisciplinary Analysis and Optimization Conference*, 2008.

[105] S. N. Lophaven, H. B. Nielsen, and J. Søndergaard, "DACE: A Matlab kriging toolbox, Citeseer," 2002.
[106] M. A. Arie, A. H. Shooshtari, S. V. Dessiatoun, E. Al-Hajri, and M. M. Ohadi, "Numerical modeling and thermal optimization of a single-phase flow manifold-microchannel plate heat exchanger," *International Journal of Heat and Mass Transfer,* vol. 81, pp. 478-489, 2015.
[107] R. K. Mandel, M. A. Arie, A. H. Shooshtari, and M. M. Ohadi, "A heat spreading model for double-sided, cross-flow, manifold-microchannel heat exchangers," *presented at the The 17th Intersociety Conference on Thermal and Thermomechanical Phenomena in Electronic Systems*, San Diego, CA, 2018.
[108] B. David, "Designing for the DMLS Process," ed: Protolabs, 2014.
[109] B. N. Taylor and C. E. Kuyatt, *Guidelines for evaluating and expressing the uncertainty of NIST measurement results*. Citeseer, 1994.
[110] Special Metals. (2018). *Inconel 718 spec sheet*. Available: http://www.specialmetals.com/documents/Inconel%20alloy%20718.pdf [Accessed September 20, 2018]
[111] Eaton. (2016). *Industrial Clamp Products*. Available: https://www.eaton.com/ecm/groups/public/@pub/@eaton/@aero/documents/content/ct_194111.pdf [Accessed September 20, 2018]
[112] Compressor World. (2018). *Powerex 5 HP Air Compressor Oilless Scroll Pump | SLAE05E*. Available: https://www.compressorworld.com/slae05e-5-horsepower-oilless-scroll-air-compressor-replacement-pump-manufactured-by-powerex.html [Accessed September 20, 2018]
[113] Engineering Page. *Typical Overall Heat Transfer Coefficients*. Available: http://www.engineeringpage.com/technology/thermal/transfer.html [Accessed April 2, 2018].
[114] W. M. Kays and A. L. London, *Compact heat exchangers*, third ed ed. Florida: Krieger, 1984.